



National Library
of Canada

Bibliothèque nationale
du Canada

Canadian Theses Service

Service des thèses canadiennes

Ottawa, Canada
K1A 0N4

NOTICE

The quality of this microform is heavily dependent upon the quality of the original thesis submitted for microfilming. Every effort has been made to ensure the highest quality of reproduction possible.

If pages are missing, contact the university which granted the degree.

Some pages may have indistinct print especially if the original pages were typed with a poor typewriter ribbon or if the university sent us an inferior photocopy.

Reproduction in full or in part of this microform is governed by the Canadian Copyright Act, R.S.C. 1970, c. C-30, and subsequent amendments.

AVIS

La qualité de cette microforme dépend grandement de la qualité de la thèse soumise au microfilmage. Nous avons tout fait pour assurer une qualité supérieure de reproduction.

S'il manque des pages, veuillez communiquer avec l'université qui a conféré le grade.

La qualité d'impression de certaines pages peut laisser à désirer, surtout si les pages originales ont été dactylographiées à l'aide d'un ruban usé ou si l'université nous a fait parvenir une photocopie de qualité inférieure.

La reproduction, même partielle, de cette microforme est soumise à la Loi canadienne sur le droit d'auteur, SRC 1970, c. C-30, et ses amendements subséquents.

UNIVERSITY OF ALBERTA

**AN EXPERIMENTAL EVALUATION OF AN ELECTRON ARC
ALGORITHM**

BY



BRAD MURRAY

A THESIS

SUBMITTED TO THE FACULTY OF GRADUATE STUDIES AND RESEARCH
IN PARTIAL FULFILLMENT OF THE REQUIREMENTS FOR THE DEGREE OF

MASTER OF SCIENCE

IN

MEDICAL PHYSICS

DEPARTMENT OF PHYSICS

EDMONTON, ALBERTA

FALL 1990



**National Library
of Canada**

**Bibliothèque nationale
du Canada**

Canadian Theses Service Service des thèses canadiennes

**Ottawa, Canada
K1A 0N4**

The author has granted an irrevocable non-exclusive licence allowing the National Library of Canada to reproduce, loan, distribute or sell copies of his/her thesis by any means and in any form or format, making this thesis available to interested persons.

The author retains ownership of the copyright in his/her thesis. Neither the thesis nor substantial extracts from it may be printed or otherwise reproduced without his/her permission.

L'auteur a accordé une licence irrévocable et non exclusive permettant à la Bibliothèque nationale du Canada de reproduire, prêter, distribuer ou vendre des copies de sa thèse de quelque manière et sous quelque forme que ce soit pour mettre des exemplaires de cette thèse à la disposition des personnes intéressées.

L'auteur conserve la propriété du droit d'auteur qui protège sa thèse. Ni la thèse ni des extraits substantiels de celle-ci ne doivent être imprimés ou autrement reproduits sans son autorisation.

ISBN 0-315-65118-0

UNIVERSITY OF ALBERTA

RELEASE FORM

NAME OF AUTHOR BRAD MURRAY

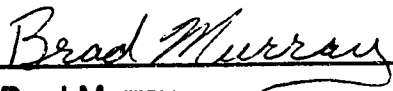
TITLE OF THESIS AN EXPERIMENTAL EVALUATION OF
AN ELECTRON ARC ALGORITHM

DEGREE MASTER OF SCIENCE

YEAR THIS DEGREE GRANTED 1990

Permission is hereby granted to THE UNIVERSITY OF ALBERTA LIBRARY to reproduce single copies of this thesis and to lend or sell such copies for private scholarly or scientific research purposes only.

The author reserves other publication rights, and neither the thesis nor extensive extracts from it may be printed or otherwise reproduced without the author's written permission.



Brad Murray

Box 1821
Kindersley, Saskatchewan
S0L 1S0

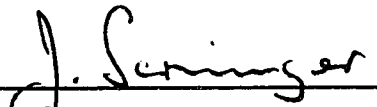
Date: June 1, 1990

UNIVERSITY OF ALBERTA
FACULTY OF GRADUATE STUDIES AND RESEARCH

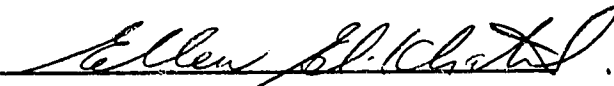
The undersigned certify that they have read, and recommend to The Faculty Of
Graduate Studies and Research, for acceptance, a thesis entitled

**AN EXPERIMENTAL EVALUATION OF AN
ELECTRON ARC ALGORITHM**

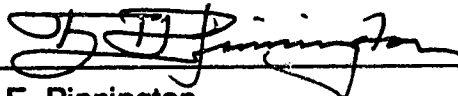
Submitted by BRAD MURRAY in partial fulfillment of the requirements for the
degree of Master of Science in Physics.



Dr. J. Scrimger



Dr. E. El-Khatib



Dr. E. Pinnington



Dr. J. Pederson

Date: June 1, 1990

ABSTRACT

Recently the Cross Cancer Institute purchased its first linear accelerator which has the capability of providing electron arc therapy. This type of treatment is starting to gain popularity, as more facilities are installing equipment with this capability. An algorithm for calculating the dose distributions from an electron arc irradiation, based on pencil beam theory, has also been introduced recently. This algorithm will likely be made available on commercial treatment planning computers, but a thorough evaluation of this algorithm has never been published. This thesis consists of a comparison of measured and calculated dose distributions from electron arc irradiations, which have been carried out for both homogeneous and heterogeneous phantoms. Nominal energies of 12 and 20 MeV have been used. The measurements were made with both film and TLD, and the calculations were done with the pencil beam algorithm originally developed at the MD Anderson Hospital. This algorithm is based on Fermi-Eyges electron transport theory, and employs a two dimensional inhomogeneity correction. A cylindrical polystyrene phantom was used, with inhomogeneities representing both ribs and lungs.

In all experimental situations, areas have been found in which there are differences between the measured and calculated dose distributions. The algorithm has been modified which improved correspondence between the measured and calculated data greatly. With this modification there are still differences between the experimental and calculated data, and possible explanations for these differences have been postulated whenever possible.

ACKNOWLEDGEMENTS

I would like to express my gratitude to the following people who have made this work easier and very enjoyable:

My wife Lori for her love and support through all of the tense situations during this program.

My parents for their encouragement and leadership throughout my life.

My supervisors, Dr. J Scrimger and Dr. E. El-Khatib, for their guidance and patience with all my work

Ernie Mah for his help in understanding and implementing the electron arc algorithm, as well as various other computing problems.

Colin Field and Claire McCartney for helping me out with all of my problems using ATP.

Finn Mortenson, Erich Schartner, and Gary Morrison for their careful construction of my phantoms.

Brent Long and Wayne Logus for their help with the technical aspects of this project.

John Isit for his help in constructing the collimators used in this project.

John Antolak for his many thought provoking discussions and his help in producing the difference maps that make the presentation of this data easier.

The University of Alberta Physics department for their financial support throughout this degree.

TABLE OF CONTENTS

CHAPTER	PAGE
1 Introduction	1
1.1 Introduction	1
1.2 Present State	2
1.3 Future Demands	4
2 Electron Beams	7
2.1 Electron Beam Production	7
2.2 Dosimetry of Electron Beams	11
3 Measurement Techniques	14
3.1 Phantom	14
3.1.1 Phantom Design	14
3.1.2 Construction	14
3.1.3 Properties of Materials	17
3.2 Dosimeters	21
3.2.1 Film Dosimetry	21
3.2.2 Thermoluminescent Dosimetry	26
3.2.3 Diodes	29
3.2.4 Ion Chambers	31
4 Computational Techniques	35
4.1 Pencil Beam Arc Algorithm	35

5 Results and Discussions	47
5.1 Comparison of Dosimeters	47
5.2 Homogeneous Phantom	49
5.2.1 Results	49
5.2.2 Discussion	55
5.3 High Density Inhomogeneities	67
5.3.1 Results	67
5.3.2 Discussion	79
5.4 Low Density Inhomogeneities	85
5.4.1 Results	85
5.4.2 Discussion	88
5.5 Summary of the Effects of the Inhomogeneities	92
6 Planning an Electron Arc Treatment	95
7 Conclusion	99
8 Bibliography	104
9 Appendix 1	107

LIST OF TABLES

TABLE 3-1	Properties of Materials	20
TABLE 7-1	Summary of Differences between Measured and Calculated Data	109

LIST OF FIGURES

FIGURE 2-1	Photograph of the Varian Clinac 2100C	7
FIGURE 2-2	Block Diagram of a Medical Linear Accelerator	8
FIGURE 2-3	Schematic Diagram of the Head of a Linac	10
FIGURE 3-1	Photograph of the Phantom	16
FIGURE 3-2	Schematic Diagram of the Phantom	17
FIGURE 3-3	Typical H & D Curve	23
FIGURE 3-4	Glow Curve for LiF	28
FIGURE 3-5	Voltage vs Current Curve for an Irradiated Diode	30
FIGURE 3-6	Schematic Diagram an Ion Chamber	33
FIGURE 4-1	Model Used in the Calculation Algorithm	38
FIGURE 4-2	Diagram of the Calculation Plane	39
FIGURE 5-1	Comparison of an Ion Chamber to a Diode	48
FIGURE 5-2	Comparison of Film, Diode and Calculated Depth Dose Curves	50
FIGURE 5-3	Dose and Difference Maps for a 12 Mev Beam on a Flat Phantom	53
FIGURE 5-4	Dose and Difference Maps for a 20 Mev Beam on a Flat Phantom	54
FIGURE 5-5	Dose and Difference Maps for a 12 Mev Beam on a Homogeneous Cylindrical Phantom	56

FIGURE 5-6	Dose and Difference Maps for a 20 Mev Beam on a Homogeneous Cylindrical Phantom	57
FIGURE 5-7	Depth Dose Curves for an Arc Irradiation Measured with TLD and Film and Calculated	59
FIGURE 5-8	Dose and Difference Maps for a 12 Mev Arc Calculated with a Pseudo-Arc Technique and with the Arc Algorithm	61
FIGURE 5-9	Dose and Difference Maps for a 12 Mev Beam on a Flat Phantom, with Modified Algorithm	63
FIGURE 5-10	Dose and Difference Maps for a 20 Mev Beam on a Flat Phantom, with Modified Algorithm	64
FIGURE 5-11	Dose and Difference Maps for a 12 Mev Arc, with Modified Algorithm	65
FIGURE 5-12	Dose and Difference Maps for a 20 Mev Arc, with Modified Algorithm	66
FIGURE 5-13	Dose and Difference Maps for a 12 Mev Arc, with an Aluminum Insert in the Phantom	68
FIGURE 5-14	Dose and Difference Maps for a 20 Mev Arc, with an Aluminum Insert in the Phantom	69
FIGURE 5-15	Dose and Difference Maps for a 12 Mev Arc, with a Hard Bone Analogue Insert in the Phantom	70
FIGURE 5-16	Dose and Difference Maps for a 20 Mev Arc, with a Hard Bone Analogue Insert in the Phantom	71
FIGURE 5-17	Dose and Difference Maps for a 12 Mev Arc, with a Rib Bone Analogue insert in the Phantom	73

FIGURE 5-18	Dose and Difference Maps for a 20 Mev Arc,with a rib Bone Analogue Insert in the Phantom	74
FIGURE 5-19	Dose and Difference Maps for a 12 Mev Arc, with Aluminum Rods in the Phantom	75-76
FIGURE 5-20	Dose and Difference Maps for a 20 Mev Arc,with Aluminum Rods in the Phantom	77-78
FIGURE 5-21	Dose and Difference Maps for a 12 Mev Arc, with an Aluminum Insert in the Phantom, With Stopping Power Correction	82
FIGURE 5-22	Dose and Difference Maps for a 20 Mev Arc,with an Aluminum Insert in the Phantom, With Stopping Power Correction	83
FIGURE 5-23	Dose and Difference Maps for a 12 Mev Arc, with a Cork Insert in the Phantom	86
FIGURE 5-24	Dose and Difference Maps for a 20 Mev Arc,with a Cork Insert in the Phantom	87
FIGURE 5-25	Dose and Difference Maps for a 12 Mev Arc, with an Air Gap in the Phantom	89
FIGURE 5-26	Dose and Difference Maps for a 20 Mev Arc,with an Air Gap in the Phantom	90
FIGURE 5-27	Curves Showing how the Depth Doses are Perturbed by Inhomogeneities	93

CHAPTER I INTRODUCTION

1.1 INTRODUCTION

Electrons have been used as a radiation source for treating cancerous tumors for many years. They are generally used to treat tumors that are situated close to the surface of the patient, or when there is radiation sensitive tissue beyond the tumor. Unlike X-rays, the electrons have a finite range in the patient and they deposit all of their energy between the patient surface and the end of their range. This means that any tissue beyond the range will not be subject to any radiation from the electrons, although there may be a small dose due to photon contamination of the beam. When treating a patient for cancer it is very important that the whole tumor receive a uniform dose, while sparing as much normal tissue as possible. This is quite easily accomplished with a stationary electron beam treatment if the patient surface is flat. If the surface is not flat the source to surface distance (SSD) will change across the patient. This will cause a non-uniform dose at a given depth in the patient because the radiation intensity is proportional to $1/r^2$ where r is the distance from the source to the surface. Therefore, if the tumor is large and the patient surface is sloped or curved the beam characteristics will have to be modified to get a uniform dose at any depth. In these situations multiple stationary beams can be used such that the edges of the fields are abutted. This, however, can lead to under or over dosing of the patient near these field edges. If the patient's surface is curved, a uniform dose can be delivered to a uniform depth below the patient surface by rotating the electron source while the electron beam is on. This constitutes electron arc therapy.

Electron arc therapy has been in use for approximately 30 years (Becker and Weitzel 1956), but has only recently started to become popular. The main reason that it was not immediately accepted is that there is a very complex relationship between many parameters of the treatment. In the past decade the computing power available has advanced and our knowledge of the interactions involved has increased to a point such that we are now better able to predict the dose distribution from an electron arc treatment. As more radiotherapy centers show interest in using this treatment mode the linear accelerator manufacturers are making this option available on more of their high energy accelerators. Therefore, many of the centers that have purchased linear accelerators in the past few years now have the ability to provide electron arc therapy.

1.2 PRESENT STATE

The radiation dose distribution in the target volume from an electron arc treatment depends on the field size, isocenter position, electron beam energy, number of monitor units per degree, patient curvature, and on the shape and position of the collimator. In particular the isodose distribution for electron arcs is very different from that for a stationary single field, because of the oblique incidence of the electrons and the velocity effect (Pla M.1988, Biggs P. 1984, Ruegsegger D. 1979). The velocity effect accounts for the fact that the linear velocity of a point close to the isocenter is smaller than a point further away from the isocenter. This means that the point near isocenter will be in the beam longer, and will receive a higher dose relative to the point farther from isocenter. This shifts the depth dose curve for an arc such that the depth of maximum dose (d_{max}) is deeper than for a stationary beam. The oblique incidence of the beam

in an arc treatment will make the average arc beam depth (the distance from the surface to any given point measured along a ray emanating from the source, and averaged over the whole arc) greater for a smaller radius of curvature. This means that d_{max} for the smaller radius of curvature will shift towards the surface. In general these two effects tend to oppose each other such that the depth dose curve for an arc electron treatment will have a deeper d_{max} , but be less penetrating than the stationary beam. There is a small amount of photon contamination (Bremsstrahlung) in the electron beam, which will penetrate deep enough to reach the isocenter. Since the beam is always directed at isocenter this photon dose at isocenter will add for the whole time the beam is on. The Bremsstrahlung component of the beam is, therefore, more important for arc therapy and needs special consideration (Pla M. 1989, Kase K. 1979, El-Khatib 1990).

Most of the research done on electron arc therapy has been focussed on two areas. The first deals with experimental evaluations of the effects of changing the various beam parameters in electron arc treatments (Leavitt D. 1989, Khan F. 1977, Boyer A. 1982, Ruegsegger D. 1979, Pla M.1988). The other major area of study has been in the development of a treatment planning algorithm which will accurately predict the dose distribution from an electron arc (Hogstrom K.1989, Leavitt D. 1985, Hogstrom K.1986, Hogstrom K. 1987). These algorithms basically use one of two approaches. The first one uses a measured beam profile and integrates it around the arc. The second uses a pencil beam approach that breaks the arc into a series of small "pencil beams", and sums the dose from all of these pencil beams. For stationary electron beam treatment planning an algorithm based on pencil beam theory is considered to be

state of the art (Hogstrom K. 1981, Mah E. 1989). This algorithm is available for electron beam dosimetry on commercial treatment planning systems. An electron arc algorithm has recently been developed which is based on this same theory and it will likely be widely available for the treatment planning of electron arcs (Hogstrom K. 1989). The complexity of electron arc treatment planning is further compounded by the presence of high and low density inhomogeneities in the target volume which perturb the dose distributions. Both high density ribs and low density lung must be considered when planning an electron arc treatment for the chest wall. Even in the case of a stationary electron beam, current clinical algorithms do not predict accurately the dose distributions within and beyond inhomogeneities (Shortt K. 1986, Cygler J. 1987, Mah E.1989). For this reason a complete investigation of the accuracy of this algorithm in and around inhomogeneities is needed.

1.3 FUTURE DEMANDS

Even though electron arc therapy has been around for many years it has not been widely used. However, as more treatment centres install linacs with this capability this treatment technique will become more common and in the future many new developments are likely to be implemented to this treatment mode. In all other radiotherapy techniques constant improvement to the treatment planning algorithms in order to achieve better accuracy is being attempted. As these are developed they may introduce methods for calculating electron arc dose distributions more accurately or quicker. Since electron arc therapy is seeing increased popularity, there will likely be many advances in the next decade. One area for development will be an implementation of an algorithm that uses a 3

dimensional inhomogeneity correction. Such advancements have recently been introduced for the stationary electron beam treatment planning algorithms (Mah E. 1989). The next generation of linear accelerators will probably have an ability to change all of the beam parameters during treatment, such as the energy of the beam, the field size, and the patient position (Leavitt 1989, Hogstrom 1986). In order to take advantage of these capabilities the computational speed of the treatment planning routines will need to be increased dramatically. In order to facilitate this increase in speed the computers used will need to be faster by orders of magnitude. In addition our algorithms could be made more "intelligent", such that they can automatically produce the best treatment plan possible (self-optimization), rather than the treatment planner trying four or five iterations to find the best plan. This, however, is a long way in the future at this time. Since the amount of time required to plan an electron arc treatment is already considered excessive, the algorithms must be sped up or the full function of the next generation accelerators will only be used for the most complex treatments.

This work will involve analyzing and testing a recently written electron arc algorithm (Hogstrom K. 1989). This testing is essential before the algorithm can be implemented clinically. There is very little measured data published to support this algorithm. Therefore, an attempt will be made to verify that the algorithm does reproduce the measured data. A stationary beam algorithm based on the same theory was developed in 1981 (Hogstrom K. 1981) and has since become widely used, and is considered to be state of the art. This algorithm has been shown to have problems predicting the dose near inhomogeneities (Mah E. 1989, Cygler J. 1987, Short K. 1986). For this reason many different configurations of homogeneous and inhomogeneous phantoms

will be used to analyze the algorithm. When the measured and calculated data do not correspond, reasons for these differences will be investigated and reported.

CHAPTER 2 ELECTRON BEAMS

2.1 ELECTRON BEAM PRODUCTION

Virtually all radiotherapy centers that treat with high energy electrons use a linear accelerator as the radiation source. These linacs are designed specifically for medical applications. A Varian Clinac 2100C linear accelerator, which is shown in Figure 2-1, was used for all the experiments described in this project. This accelerator is capable of producing electrons of nominal energies of 6,9,12,16, and 20 MeV, as well as 6 and 18 MV photons. The following will be a brief description of medical linear accelerators.

A basic linac consists of the following parts as shown in block diagram form in Figure 2-2. The accelerating structure is housed in the gantry, which is

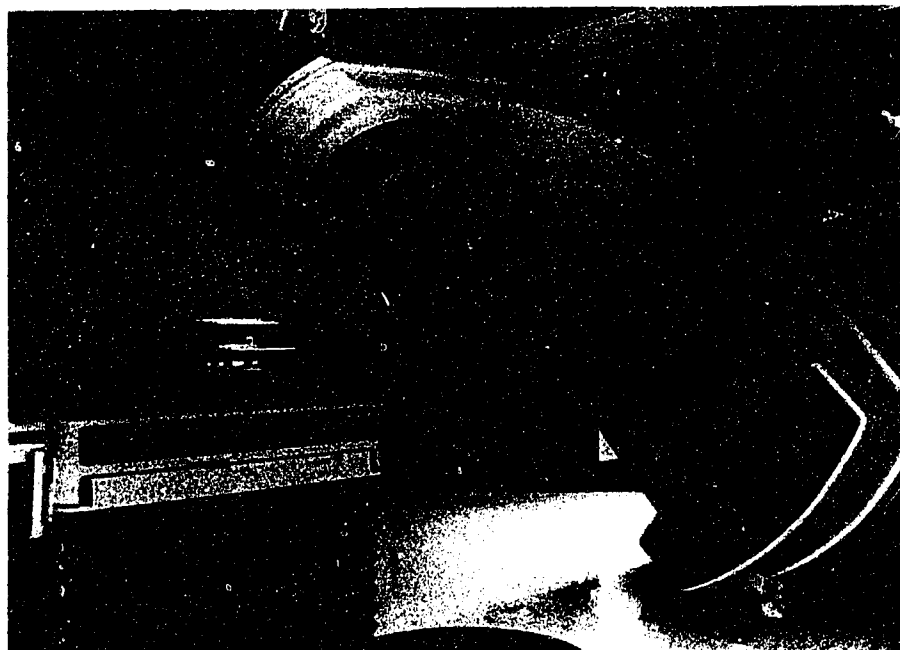


FIGURE 2-1 Photograph of the Varian Clinac 2100C

attached to a stand, such that the gantry can rotate a full 360°. This allows the radiation to be directed at the patient from any angle. The radiation emerges through the collimators. The central axis of the radiation beam is always directed through the gantry axis. The point in space where the beam axis intersects the gantry axis is called the isocenter. The treatment couch also rotates around the isocenter, and is used to move the patient into a position such that the tumor is aligned with the central axis of the radiation beam. Aligning the patient is made easier by the use of lasers, which project the position of the isocentric axis onto the patient surface. The linac has to be housed in a room that will prevent any excess radiation from penetrating through the walls or ceiling into areas that can be occupied by workers or visitors. This usually means that the rooms will have very thick concrete walls. The treatment console area will be outside the treatment room, and will house the electronic or computerized controls which

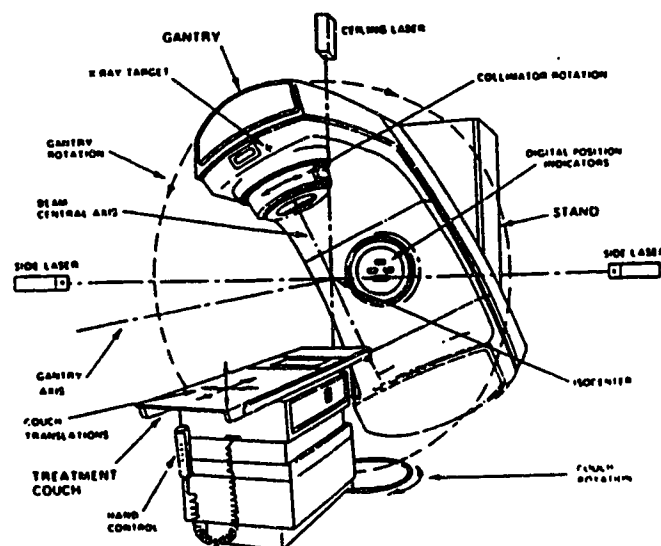


Figure 2-2 A block diagram of a medical linear accelerator

allow the operator to turn the linac on and off as well as setting the dose and various other machine parameters.

The actual electron accelerator is housed in the gantry. Radio frequency (RF) power is injected into the accelerator from the wave guide and allowed to reflect at both ends. The RF power creates very intense electric fields in the cavities of the accelerator. Since the RF is allowed to reflect from both ends it will set up a standing wave in the accelerator. The electrons are injected into the accelerator, and are accelerated by these electric fields. The linac is designed such that the electrons ride the standing wave down the accelerator being accelerated throughout their travel. By the time they reach the end of the accelerator they have reached their required energy. An excellent review of the accelerator design was done by Karzmark (Karzmark C. 1984).

The accelerating structure is in the gantry, which is horizontal. However, the electrons are required to be perpendicular to this direction for treatment purposes. Therefore, when the high energy electrons leave the accelerator they are bent through either 270 or 90 degrees (depending on the accelerator manufacturer) by means of a bending magnet, such that they are directed towards the isocenter. Once the beam has been bent it enters the treatment head. A schematic diagram of the components in the head is presented in Figure 2-3. For electron beam therapy a scattering foil is placed in the beam at its focal point beyond the magnet. This tends to scatter the electron beam, spreading it into a size that is useful for treating patients. Some manufacturers, however, will scan the electron beam using magnets, similar to the raster on a TV, to produce a wide treatment beam instead of using scattering foils. The

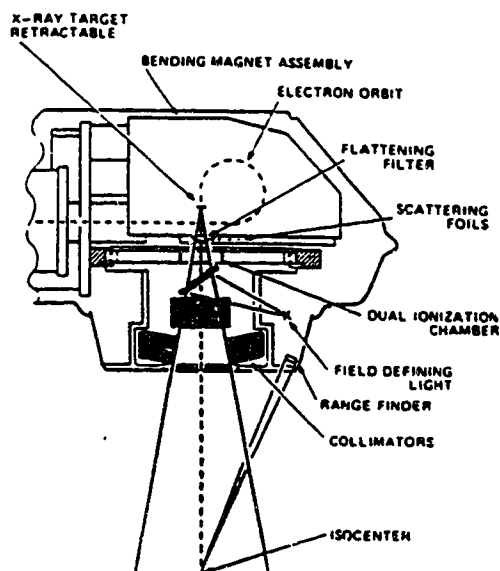


Figure 2-3 A schematic diagram of a treatment head of a medical linac

beam then goes through an ionization chamber which monitors the total dose, the dose rate, and the symmetry of the beam. Next the beam enters the collimating devices, which define the size of the beam entering the patient.

Most medical linacs that produce high energy electrons will also have the capability to produce high energy photons. This is accomplished by placing a target made of a high Z material such as tungsten into the electron beam. This, however, will require a much higher beam current than was required for electron beam therapy in order to produce a useable photon beam. The target is normally placed in the beam immediately after the bending magnet. This is shown in Figure 2-3 where the target is shown removed from the beam as it would be for an electron treatment. The Clinac 2100C offers 6 MV and 18 MV photons, where the unit MV designates that the photons are produced from an electron beam of that energy in MeV.

It is very practical to have an accelerator that has multiple energies of photons and electrons, since many treatments will use more than one energy or type of radiation. Therefore, a multimode accelerator will allow the patient to be given their complete treatment without being moved from one treatment room to another, which makes it more efficient and set up errors will be less likely to occur.

2.2 DOSIMETRY OF ELECTRON BEAMS

There are many methods of measuring the dose from an electron beam. The dosimeters that have been used for these experiments are discussed in detail in Chapter 3. There are some theories that, regardless of the type of dosimeter used, must be used to find the correct absorbed dose from the measured signal. These theories relate the quantity as measured by the dosimeter to the dose to the medium in the absence of the dosimeter. These are called cavity theories, and depending on the size of the cavity, different theories will need to be used. The main theory that will apply to the analysis of the results reported in this thesis is the Bragg Gray Cavity Theory (Bragg 1910, Gray 1936).

BRAGG GRAY CAVITY THEORY

Bragg Gray cavity theory is based on the fact that

$$D = \Phi \left(\frac{dT}{\rho dx} \right)_c \quad \text{eq 2-1}$$

where D is the absorbed radiation dose to the material.

Φ is the fluence (# of charged particles per unit area).

$\left(\frac{dT}{\rho dx}\right)_c$ is the mass collision stopping power of the medium evaluated at energy T.

If the electron beam passes through an interface between two media without changing the fluence of the beam, the ratio of the doses on either side of the interface can be written as

$$\frac{D_W}{D_G} = \frac{\left[\left(\frac{dT}{\rho dx}\right)_{c,T}\right]_W}{\left[\left(\frac{dT}{\rho dx}\right)_{c,T}\right]_G} \quad \text{eq 2-2}$$

where W and G represent the two materials.

The ratio of the mass collisional stopping powers of media W and G is commonly written as $\left[\frac{S}{\rho}\right]_G^W$

This leads to the equation

$$D_W = D_G \left[\frac{S}{\rho}\right]_G^W \quad \text{eq 2-3}$$

For the case when there is a thin cavity of material G surrounded by material W, and the properties of the two are sufficiently similar, then the fluence of electrons will not be significantly changed. In this case, we can use the above equation to describe the dose to the phantom in the absence of the dosimeter, where W is the phantom material and G is the dosimeter material.

In the experiments to be described later, the dose distributions are normalized. Therefore, it is necessary to develop a relationship between the normalized dose as measured by the dosimeter and the actual normalized dose to the material. For the case of a thin dosimeter where Bragg Gray cavity theory

applies, the normalized dose to the material is

$$\frac{D_w(x,y)}{D_w(\text{Norm})} = \frac{D_g(x,y) \left[\frac{S}{\rho} \right]_G^W T(x,y)}{D_g(\text{Norm}) \left[\frac{S}{\rho} \right]_G^W T(\text{Norm})} \quad \text{eq 2-4}$$

where $D_w(x,y)$ is the dose to the material at point (x,y)

$D_g(x,y)$ is the dose to the dosimeter at the point (x,y)

$D_w(\text{Norm})$ is the dose to the material at the normalization point

$D_g(\text{Norm})$ is the dose to the dosimeter at the normalization point

$\left[\frac{S}{\rho} \right]_G^W$ is the ratio of mass collisional stopping powers of materials W and G at the energy T of the point (x,y) or the normalization point.

Even though the mass collisional stopping power is very energy dependent the ratio of stopping powers is nearly energy independent over the energy range and for the materials that are considered in these experiments. Therefore, provided that the phantom is homogeneous the ratio of stopping powers will be unity and the normalized dose as measured by the dosimeter will be equal to the actual normalized dose. If, however, the phantom is not homogeneous the ratio of stopping powers will not be unity, and the entire expression will need to be evaluated. Therefore, in the areas that have inhomogeneities the normalized dose will be different from the normalized dose as measured by the dosimeter, because the normalized dose will be the dose measured inside the inhomogeneity divided by the dose measured in the homogeneous section of the phantom.

CHAPTER 3 MEASUREMENT TECHNIQUES

3.1 PHANTOM

3.1.1 PHANTOM DESIGN

In radiological experiments human subjects cannot be used to acquire the needed experimental data. In these experiments an inanimate object can be designed that will represent the subject. This object is commonly called a phantom. The phantom must be designed such that it has the same radiological properties as the tissue that will be encountered during an actual treatment. The size and shape of the phantom used in these experiments should be of similar dimensions to the human body in an area that would likely be treated with an electron arc treatment. The phantom was designed such that experiments could be performed on either a homogeneous area in the phantom or one with inhomogeneities in the target volume. These inhomogeneities must also be of some radiological importance to electron arc treatments. Specifically the phantom was designed to simulate electron arc treatments of the chest wall, and the inhomogeneities simulate ribs and lung. The design of the phantom must also permit the placement of dosimeters in the phantom such that a complete dose distribution could be measured for an arc irradiation. The dosimeters of choice to meet these criteria are film and TLD chips. Thus the design incorporated the ability to use either of these dosimeters anywhere in the phantom.

3.1.2 CONSTRUCTION

In order to get a simplistic geometry to study, but yet physiologically

similar to the human body the phantom shape was chosen to be a cylinder. A common area for electron arc treatments is in the chest wall, therefore, the radius of the cylindrical phantom was chosen to be 17.5 cm, which is a typical radius for an adult male chest. The length of the phantom was chosen to be 30 cm such that the phantom would provide full scatter for typical field sizes encountered with this type of treatment. In order to facilitate insertion of the dosimeters anywhere in the phantom, it was constructed as a series of circular sections 18 mm wide. These could then be clamped together to form a cylinder. A piece of film could then easily be sandwiched between two sections of interest to measure the dose distribution in that plane of the phantom. This also allowed two of these sections to have heterogeneities inserted into them. Then these two sections could be put in the phantom in any position depending on the experiments to be done. Two holes were drilled one on either side of center in each section, which allowed two rods to be passed through all the sections to keep them from rotating independently. These rods were threaded in order that they could be used to clamp the entire phantom together securely. A "book ends" style apparatus was constructed such that the phantom could be held in place and would not roll off the treatment table during irradiation. Figure 3-1 is a photograph of the assembled phantom which illustrates the position of the rods that pass through the phantom, and the overall design.

Inhomogeneities were inserted into the phantom to simulate rib and lung. The position and shape of these inhomogeneities is illustrated in Figure 3-2. For the rib equivalent insert a 6 mm deep slot was milled in two slabs, such that these two slabs could be placed together to form a 12 mm deep slot. The slot covered 70 degrees and was cut along an arc with radius from 15.5 - 16.5 cm,

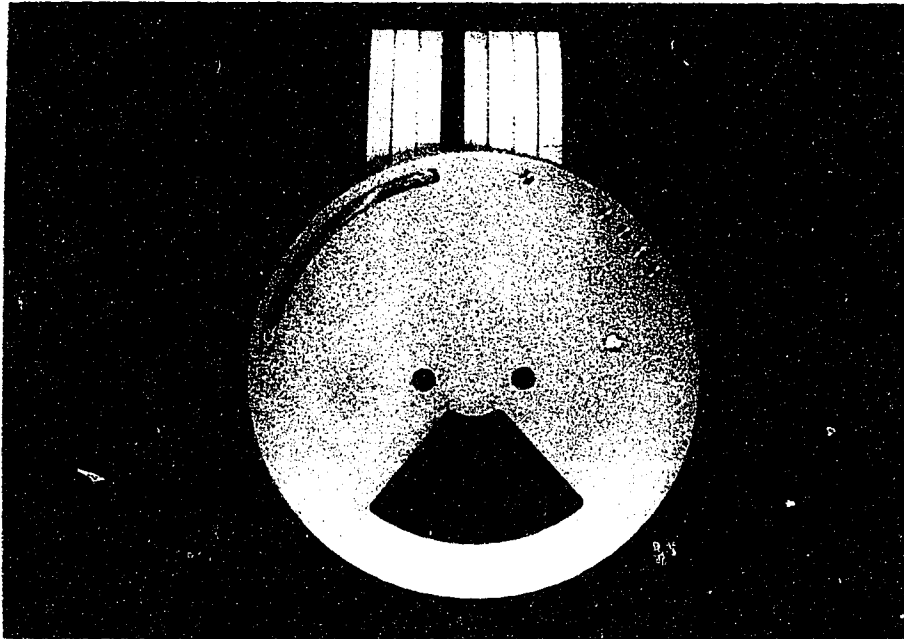


Figure 3-1 A photograph of the phantom used in these experiments with the inhomogeneous section removed.

thus making a 1 cm wide slot, 1 cm from the surface. These slots were then filled with one of the following materials: Aluminum (>99.0 % pure), hard bone analogue, or rib bone analogue (Scanplas). Another high density inclusion was made with Aluminum bars running parallel to the central axis of the phantom. These rods were 1 cm in diameter and 18 mm long. They are centered at a radius of 16.0 cm from the center of the phantom at the following angles: 30, 37, 44, 51 and 75 degrees. This gives a separation of about 1 cm between each of the first four rods, and one is set apart from the rest by nearly 7 cm. Their positions are also shown in Figure 3-2. In these same two slabs an 18 mm deep piece was cut out and filled with cork to simulate lung. This insert was separated from the rib insert by 60 degrees as shown in Figure 3-2. The dimensions of the cut out were such that the inhomogeneity would start at a depth approximately equal to the depth of the 80% isodose line for an arc on a

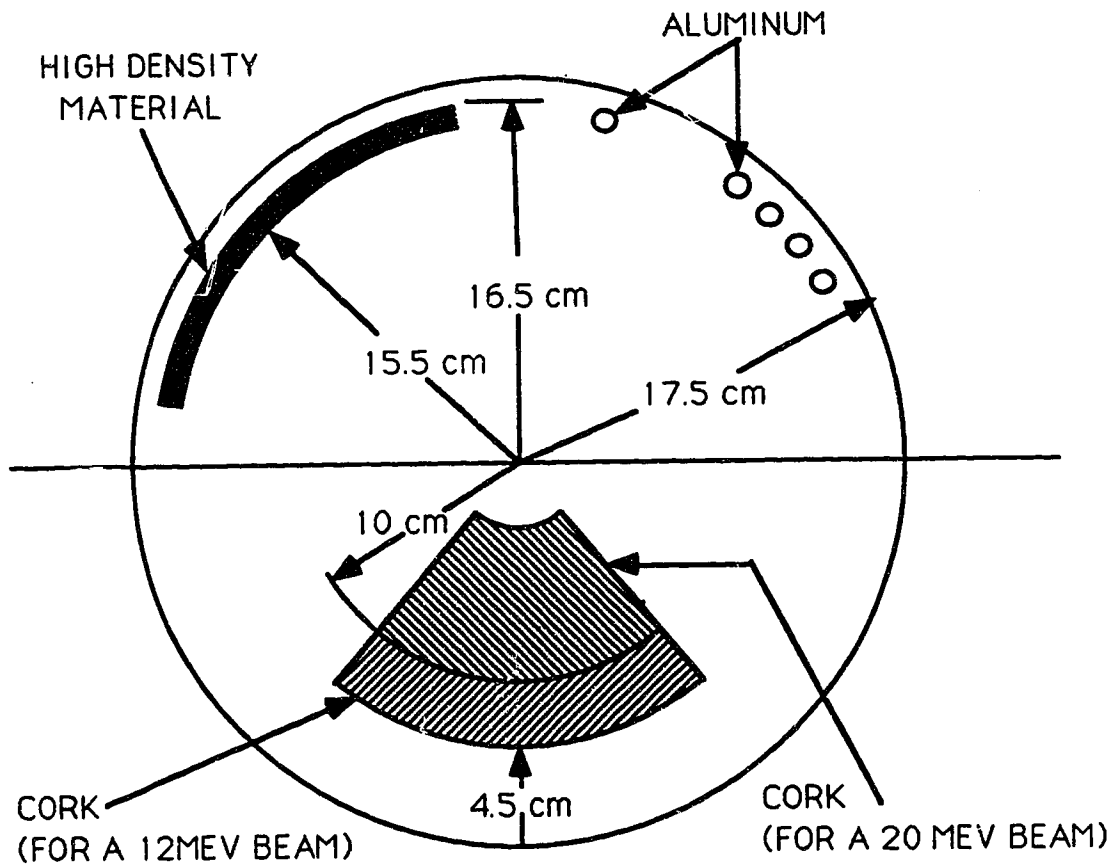


Figure 3-2 A schematic diagram showing the position of the inhomogeneities in the phantom.

homogeneous phantom. This was at a depth of 4.5 cm for 12 MeV, and 7.5 cm for 20 MeV, these being the two electron beam energies used in this study. This insert extended down to a radius of 3 cm in both cases and extended over 80 degrees.

3.1.3 PROPERTIES OF MATERIALS

It is vital that the materials used in radiotherapy experiments accurately

simulate the section of the human body that they are supposed to represent. In most cases we are trying to simulate normal tissue; however, we also need materials of both higher and lower density to model bones and lung.

For a material to be acceptable as a tissue substitute for photons and electrons, the radiation absorption and scattering coefficients for a given thickness or mass of the material should be the same as those for a similar thickness or mass of tissue.

Electrons interact with matter through three main types of interactions:

1) "Soft Collisions" - These collisions occur when the incident high energy electron interacts with an atom, where the distance from the nucleus is much larger than the nuclear radius. This is by far the most common type of interaction, but there is very little energy deposited in an individual reaction. Since they are so common, however, they account for about half of the total energy lost by the incident electron.

2) "Hard (knock on) Collisions" - These occur when the incident electron is approximately one nuclear radius away from the center of the nucleus. These collisions are far less frequent than the soft collisions. However, they cause the incident electron to lose a significant fraction of its energy in each interaction. Therefore, the hard collisions also account for about half of the total energy lost by the incident electron.

3) "Coulomb Force Interactions"- These occur when the electron is much less than one nuclear radius away from the center of the nucleus. These are very rare and make up only a small percentage of the total energy lost.

The electron will lose most of its energy through interactions with atomic electrons. This means that in order for two materials to be radiologically equivalent they must have the same electron density. For low atomic number materials this basically translates into finding two materials with the same mass density. If the mass stopping power and mass angular scattering power are the same as the tissue the material will be radiologically equivalent. Both the mass stopping power and the mass angular scattering power are energy dependent, and it is important that they match in the energy range intended (White 1978).

In these experiments the phantom was constructed from polystyrene as normal tissue substitute. This material meets the above requirements quite well in addition to having desirable mechanical characteristics for machineability. The characteristics of the materials used in the phantom are shown in Table 3 - 1. To simulate bone in the phantom three different materials were used: aluminum, hard bone analogue, and rib bone analogue. The aluminum was used as a "stress test", as this is a higher density than would ever be encountered in the human body. The two bone analogue materials were produced by a commercial manufacturer (Scanplas) and represent different types of bone that are likely to be encountered in the body. The final material used was cork, which simulated lung tissue. A perfect lung equivalent material is difficult to quantify because the lung density is very different for different people, and it varies throughout an individual lung (Van Dyk J. 1982). The density varies from that of air in the alveoli to unit density, and will change during the breathing cycle, depending on how much air is in the lung. Cork is widely accepted as a phantom substitute for lung.

One section of the phantom was specially constructed in order to allow easy accurate positioning of the TLD chips within it. TLD's will be discussed later in this chapter. The chips that were used were of dimensions 1/8" x 1/8" x .035". A piece of 1/8" polystyrene was cut to the same shape as the rest of the phantom pieces. In this section slots were milled 1/8" long and .070" wide such that two chips could be placed on end in each slot. The slots were cut at intervals of 5 mm in depth from the surface to 11 cm deep, and one was cut at 14.5 cm from the surface, and another at the center of the phantom, 17.5 cm deep. The chips are not exactly tissue equivalent (Harshaw Filtrol Performance Specifications), but two chips will not significantly perturb the beam. However, if all the chips were aligned, forty of them may perturb the dose enough to give inaccurate results. The chips were, therefore, offset so they would not be aligned. This meant that the arc must be long enough so that this whole area will be irradiated

TABLE 3 - 1		
MATERIAL	CT NUMBER (HOUNSFIELD UNITS)	DENSITY (g/cm³)
WHITE POLYSTYRENE	30	1.08
ALUMINUM	2250	2.7
RIB BONE	470	1.28
HARD BONE	1060	1.87
CORK	- 690	0.31

equally, so that there are no penumbral effects at the edge of the arc affecting the TLD's.

3.2 DOSIMETERS

3.2.1 FILM MEASUREMENTS

Film makes a very good dosimeter for electron arc therapy because of its excellent spatial resolution, along with the fact that it is an integrating dosimeter and is therefore capable of measuring the dose from a moving beam (Dutreix and Dutreix 1969).

Film is composed of a layer of emulsion on a cellulose acetate or polyester film. This emulsion is made of silver halide crystals suspended in a gelatin base. When film is exposed to ionizing radiation or light a chemical change takes place within the exposed crystals. The radiation causes some of the electrons in the silver halide crystals to gain energy and diffuse away. Through the process of "hole diffusion" the Bromine atoms will also diffuse away. This leads to the positive silver ions being clumped together. These silver ions constitute the latent image. A three stage chemical process is then able to transform this latent image into a useful image. The first stage is the developer, which will reduce the affected crystals into small grains of metallic silver. The second stage is to put the film into a fixer which dissolves and removes the unaffected silver bromide atoms leaving only the clear film base in this area. The metallic silver is not affected by the fixer, thus the areas exposed to radiation will appear black on a clear film. The final stage is to rinse the film in clean water to remove any chemical residue from the film. It is then dried and is ready to be

processed.

To analyze a film the degree of blackening of the film must be measured. A densitometer is used for this measurement. Basically the densitometer consists of a light source and a photo detector. The amount of light passing through the film and reaching the photo detector will be inversely proportional to the amount of blackening of the film. Since the film base is not completely clear, it will attenuate the light by a constant amount regardless of the absorbed radiation. There is also a fog level, which depends on both the development and processing conditions for the film. For this reason, a base + fog reading must be taken into account when making film measurements. The unit used to measure the amount of blackening of the film is the optical density, which is defined as

$$OD = \log I_0/I_t \quad \text{eq 3-1}$$

where I_0 = amount of light collected without a film

I_t = amount of light transmitted through the film.

A film is normally characterized by its H & D (Hurter and Driffield) curve, which plots the optical density versus dose. This curve is linear at low doses for Kodak XV- 2 film, which was used for these experiments; but at high doses the film begins to saturate and the H & D curve will plateau. Therefore, it is vital that all measurements be done in the linear area of the H & D curve or corrections will be necessary. Figure 3-3 is a typical H & D curve for Kodak XV-2 film, which was used in these experiments. It shows that the optical density is linear with dose for optical densities up to about 1.7 with the base + fog reading subtracted. This is within the range of optical densities used in these experiments, therefore,

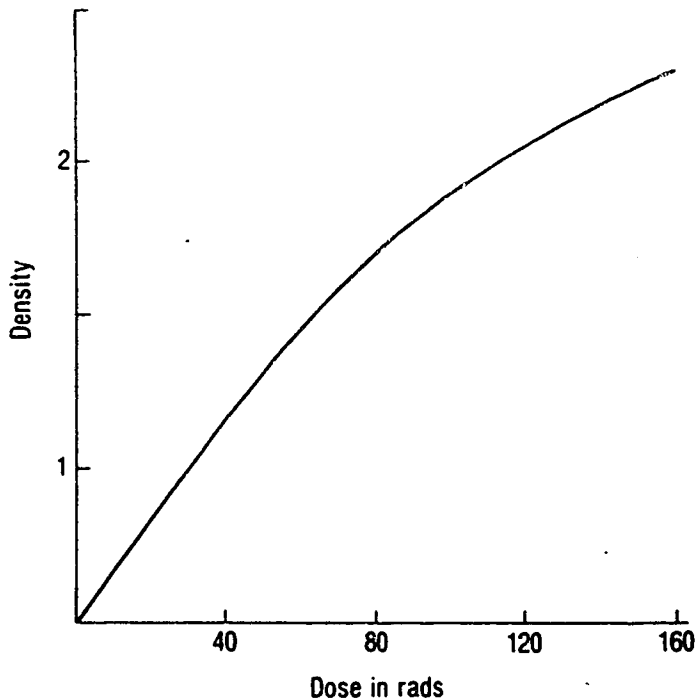


Figure 3 - 3 A typical H - D curve for Kodak XV-2 Film. It shows linearity of density vs. dose up to densities of approximately 1.7.

no correction is needed to get the relative dose from the relative optical density.

A simple densitometer is very useful for measuring the optical density at a single point. However, in order to measure a complete dose distribution with a densitometer it is almost essential to use an automated isodensitometer. An automated densitometry system is capable of accurately moving to a given position and measuring the optical density at that point. At the Cross Cancer Institute we have such a system called an RFA-7 manufactured by Scanditronix. This is a completely computer controlled apparatus and allows a great deal of flexibility in the way that the data can be analyzed. The next section will describe the RFA-7 film measurements mode.

In the film measurements mode there are many ways that data can be acquired using the RFA-7, including:

1) Single scan in one direction

2) Matrix scan - one or more scans in each direction parallel to the major axis

3) Isodose tracking

All three modes have been used in the analysis of the data, but the primary method of collecting data was to use the matrix scan mode. In this mode the computer is programmed with the Y co-ordinates of the first and last scan in the X direction, and the spacing between scans. The same is done for scans in the Y direction. The scan step, which is the distance between two adjacent points in the same scan, is also defined. With this information the RFA-7 will automatically move the densitometer to the proper position and measure the optical density of the film at this point. It will carry out this procedure until it has measured the optical density at each point in the matrix. As the data is measured, it is plotted on the screen in real time. After measuring the data it can be stored on disk and manipulated into the format that is needed. By making all of the scans in one direction with equal spacing, the information can easily be put into a rectangular dose matrix. This information is then ready to be compared to a calculated dose matrix for evaluation of the calculation algorithm.

In isodose tracking mode, the RFA-7 prompts the operator to enter the levels for it to track, as a percentage of the normalization optical density. From there it does a pre-scan in the X and Y directions to find starting points for each

of the levels that it will track. Then it will move to the position where it found the first level when it did the X-Y pre-scans. From here it simply moves the densitometer in small steps, searching for that same level. Once it has followed a complete isodose such that the path is closed, it will go on to the next isodose level. It will continue to do this until it has tracked all the isodose levels that were input. A very quick and efficient way of comparing the measured dose distribution to a calculated distribution is by simply overlaying the two hard copies of the isodose lines and comparing their position. For this reason the RFA-7 has an option to print the isodose lines to scale. This does not, however, provide as much information about the differences between the dose distributions as a full difference map, which utilizes a digital subtraction of the two dose matrices. Therefore, tracking of isodose lines was used only to generate preliminary information.

The RFA-7 specifies that it has a positional reproducibility of 0.1 mm. This does not mean that the co-ordinates of the measurement are this accurate, because the operator positions the photo diode at a point called the origin, at coordinates $X=0$, $Y=0$. If the operator does not position this exactly at the point that is truly (0,0) the co-ordinates will obviously be in error by more than 0.1 mm. The specifications also state that the densitometer is accurate to 0.001 optical density units, where $OD = \log I_0 / I_t$.

As a dosimeter, film has acquired a bad reputation. This is mainly due to the large energy dependence it shows for photon beams. The attenuation of a photon beam of low energy is almost completely due to the photo-electric effect, and at higher energies the Compton effect starts to dominate the attenuation

coefficient. The photoelectric effect has a Z dependence of the order of Z^3 and an energy dependence of $1/E^3$ (Hubbell 1969), while the Compton effect is proportional to the electron density (e^-/cm^3), but is independent of Z. Since film emulsion has a high amount of silver ($Z=45$), there will be a strong influence of atomic number for low energy photons, compared to the high energy photons. Since a medical photon beam generally has a continuous energy spectrum, film is not a good dosimeter for photon beams. However, there is very little photon contamination of the electron beams, and film is far better suited as an electron beam dosimeter, than as a photon beam dosimeter.

Differences in the parameters of the film processor can make drastic differences to the optical density of the film. Therefore, measuring the absolute dose using film as a dosimeter is very difficult. Strict control of the temperature of the chemicals, and the time that the film is exposed to each chemical must be ensured. However, if relative measurements are required these parameters are not as important since everything will be constant for that particular film, and an absolute dose is not being measured.

The spatial resolution that can be derived from the film is limited only by the densitometer that is used to analyze the film. Film also provides a permanent record of the dose distribution which can be re-analyzed at any point in time. For these reasons film makes an excellent dosimeter to measure the relative dose distributions from an electron arc treatment.

3.2.2 THERMOLUMINESCENT DOSIMETRY

When a crystal that exhibits thermoluminescence is irradiated a small

amount of that energy will be stored in the crystal lattice. If the crystal is then heated it will give off an amount of light that is proportional to the amount of energy absorbed. This is the principle used in Thermoluminescent Dosimetry.

After the TLD chips had been irradiated a Harshaw 2000 series TLD reader was used to find the dose absorbed by the TLD. The basic principle of operation is that the chip is heated and a photo multiplier tube is used to measure the light output from the chip. The photo multiplier tube converts the light output to electrical current, which can be amplified and measured by a counting device.

A plot of the thermoluminescence versus temperature is called the glow curve. A measure of the total energy absorbed by the TLD can come from either the peak height of the glow curve, or from the total area under the curve. Many of the TLD materials have traps at various energy levels, therefore, there will be numerous peaks in the glow curve, and the mean life time in the trap will be proportional to the energy level of the trap. In these experiments LiF was used as the TLD material. Figure 3-4 presents the glow curve for LiF which shows the many peaks and their mean life time at room temperature.

When measuring the dose using TLD the highest degree of accuracy is achieved by integrating the total light output (i.e. area under the glow curve) as this will always be constant for a given dose regardless of heating rate. The peak height of the glow curve, however, will depend on the heating rate, therefore, the peak height should only be used if the heating rate is very stable.

Since there is often a small peak that has a relatively short mean life in the

trap at room temperature (less than 24 hours), it is often desirable to raise the temperature to a point that will eliminate these before reading. This is called the "pre-read anneal", which then makes the time between irradiation and reading less vital.

After the TLD phosphor has been read, it can be annealed such that it can be used again. The annealing process involves raising the temperature of the phosphors to a given level for a period of time long enough to ensure that all of the traps have been emptied.

TLD, therefore, has some very useful applications in measuring the dose in electron arc therapy. Since they are integrating dosimeters they can be used in a moving beam to measure the dose. TL comes in many forms; mainly powder, chips, teflon matrix, rods, and bulk granulated. LiF TLD 100 chips were

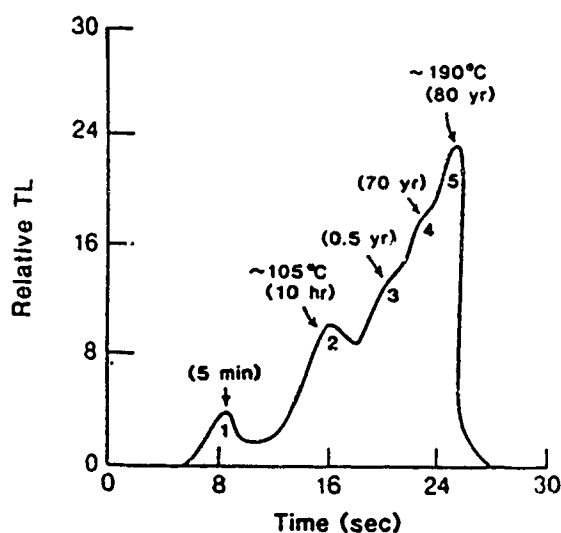


Figure 3 - 4 The glow curve for LiF TLD material

used extensively in these experiments. They had dimensions of 1/8" by 1/8" by .035" thick. This size made them rather large to try to measure accurately the entire dose matrix. They are, however, ideal as an absolute dosimeter to spot-check the results obtained with a dosimeter such as film, which has excellent spatial resolution but is not practical as an absolute dosimeter. In these experiments, the TLD chips were used to verify the depth dose measurements made with film.

3.2.3 DIODES

Diodes are solid state electronic devices that are affected by incident radiation. These effects are characteristic of the diode, and can thus be used to measure the dose. A diode can be constructed in a variety of ways, and connected in different ways, each providing a different method of measuring the dose. Generally, a silicon diode doped with a p-n junction is used in medical physics applications. The diode is normally operated without a bias voltage. In this configuration the reverse current in the diode is proportional to the dose deposited in the diode junction. Figure 3-5 shows the difference between the current through the unbiased diode with and without radiation incident on the junction. The theory of operation of diodes for radiation detection has been discussed by Rickner (Rickner 1983).

Diodes are not very useful in applications such as electron arc therapy because they are not integrating dosimeters, therefore, they can not measure the dose from the moving beam. However, they are very useful in measuring dose distributions for stationary beams in a water phantom. This is in fact what they were used for in this project. Dose distributions were measured for stationary

electron beams with the electron arc applicator installed. This information was necessary as an input parameter to the electron arc algorithm.

The RFA-7 which was used in the analysis of films also has a water phantom measurements mode. The water phantom is ideally suited for making measurements with either an ion chamber or a diode. The ion chamber will be described in the next section of this chapter. With the water phantom the same type of scans could be obtained as with the film mode. In addition, a third dimension can be used with the water phantom. For the isodose tracking, it will only track in one plane, but the operator can choose which plane to track in. When doing measurements in the water phantom there are some things that must be considered, which are unnecessary with the film measurements. First, the measurements are gathered in "real time", and the signal must be averaged

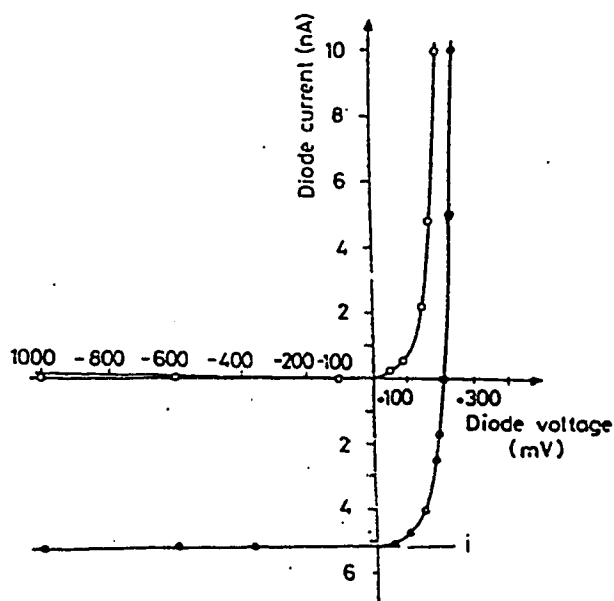


Figure 3 - 5 Typical voltage - current characteristics of a silicon diode, showing the response with radiation (filled circles) and without radiation (open circles).

over a time period long enough to eliminate statistical fluctuations in the beam. Second, the movement of the dosimeter through the water will perturb the surface, and either the speed of the movements must be slow enough to sufficiently reduce the perturbation of the surface or there must be a settling time between the movement and the measurement. With the RFA-7 both the speed that the dosimeter moves and the integration time for each measurement is set by the operator.

The RFA-7 also specifies a positional reproducibility of 0.1 mm for the water measurements. As with the film measurements mode, the diode or ion chamber is moved to a point in the phantom and labelled as the origin. If this is not set properly the coordinates will have more error involved than the 0.1 mm reproducibility. The accuracy of the water phantom measurements is a function of both the RFA-7 accuracy and the stability of the diodes or ion chambers used in the measurement. However, in both cases the overall accuracy is approximately 1%.

3.2.4 ION CHAMBERS

Ion chambers are generally considered to be the standard dosimeter for most radiotherapy departments. This is because they are very accurate and can measure the dose from any type of ionizing radiation, although the reading from the ion chamber may need to be corrected to obtain true absorbed dose from ionization.

When radiation passes through a material it will cause ionizations in the material. If these occur in an area with a strong electric field the electrons will be

separated from the ions and can be collected. This is the basis of operation of an ion chamber. It is important that the wall of the ion chamber be thick enough to produce electronic equilibrium inside the chamber. If the wall is made of air it will have to be quite thick, but the wall can be made of an air equivalent solid material which will reduce the wall thickness substantially. Figure 3-6 is a schematic diagram of a thimble ion chamber along with the cross sectional view of both the air wall and solid air wall chambers. The central electrode of the ion chamber is normally held at between -200 to -500 volts and the wall is grounded. The polarity can be switched and the ion chamber will operate in the same manner. The inside of the chamber wall must be coated with a thin conductive layer in order that the whole wall will be grounded. The application of this large potential will create a strong electric field between the wall and the central electrode. This allows all the electrons from the radiation induced ionizations to be collected. Collecting this charge will cause a current to flow, which can be measured by an electrometer. The dose to the gas can be related to the charge collected through the equation

$$D_{\text{gas}} = \frac{Q}{m} \frac{W}{e} \quad \text{eq 3-2}$$

Where D_{gas} is the dose to the gas in the chamber.

Q is the charge collected by the electrometer.

m is the mass of gas (air) in the chamber.

W/e is the energy needed to create one ion pair.

The amount of ionization produced in the cavity will depend on the amount

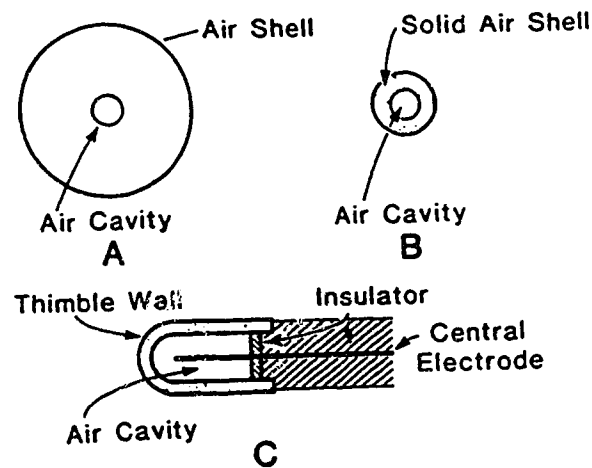


Figure 3 - 6 A schematic diagram of an ion chamber, showing (A) an air shell and air cavity, (B) a solid air shell and air cavity, and (C) a thimble chamber.

of gas in the cavity. The common ion chambers are usually not sealed units, and it is necessary to correct for temperature and pressure to obtain the proper reading. Some units such as the ion chambers in some linacs and water proof ion chambers are sealed, therefore, they will not need to be corrected, as the amount of air in the chamber will be constant. The amount of ionization produced in the chamber as measured by the electrometer can be converted to absorbed dose using an appropriate protocol (eg TG - 21) (Task Group 21), which takes into account all of the variables within the ion chamber and electrometer. Absorbed dose can also be found for any wall material surrounding the cavity by using the Bragg - Gray cavity theory, discussed in Chapter 2. Only the thimble ion chamber has been discussed here, but it should be noted that ion chambers come in many different sizes and shapes, depending on their application (Attix F. 1986)

Ion chambers are generally required to be calibrated against a standard

dosimeter every couple of years to ensure that all the parameters have remained constant. This is usually carried out at a National Standards Laboratory. These calibrations require that both the ion chamber and the electrometer to be calibrated together, since the accuracy of any measurement depends on the accuracy of both instruments.

CHAPTER 4 COMPUTATIONAL TECHNIQUES

4.1 PENCIL BEAM ALGORITHM

The calculation algorithm used to predict the isodose distributions for the electron arc treatments was developed by Hogstrom et al (Hogstrom 1989). This algorithm is based on pencil beam theory, which is derived from Eyges solution to Fermi's electron transport equation (Eyges 1948). This approach has been used quite successfully in an algorithm used to calculate the dose distributions from a stationary electron beam (Hogstrom 1981). The broad electron beam is broken down into a series of infinitesimal electron beams (pencil beams). The dose to a given point from each of the pencil beams can be calculated, then the sum of the doses from each pencil can be found to give the total dose at any point. The stationary electron beam algorithm has been shown to predict the dose distributions quite well in homogeneous phantoms. However, in and around inhomogeneities there can be substantial errors (Mah E. 1989). In the electron arc algorithm the pencil beams start at the electron source. From this point they are transported through the various media down to the patient. As the electron beam passes through these different media, they are scattered by an amount predicted by the angular scattering power of the media. These scattering media cause the pencil beam to spread out such that when it reaches the patient it has some inherent spread in the width of the pencil beam. As the pencil beam passes through the patient it is spread out even more depending on the type of material that the beam traverses. The algorithm uses the variable sigma to represent the angular distribution of the gaussian shaped pencil beam. The pencil beam will get wider as it gets scattered. Thus the value of sigma (the

width of the pencil beam) will depend on the distance from the source to the point in question, and the media that the pencil beam has traversed in arriving at that point. The algorithm uses the parameter sigma in various ways depending on the type of calculation. In the following description of the algorithm the definition of sigma will depend on where the pencil beam under consideration starts, and the material through which it is being transported. The superscript to the left of σ defines the position from which the pencil beam is propagated. The subscript to the left indicates where σ is being evaluated. The first subscript to the right shows which parameter is of interest, and the second subscript to the right determines what has caused the pencil beam to spread. This is illustrated below.

$$\begin{array}{l}
 \text{pencil} \\
 \text{beam} \\
 \text{origin}
 \end{array}
 \left(\begin{array}{l}
 \text{s, virtual source} \\
 \text{c, secondary collimator} \\
 \text{si, ith strip beam origin}
 \end{array} \right)$$

$$\sigma$$

$$\begin{array}{l}
 \text{plane of} \\
 \text{evaluation}
 \end{array}
 \left(\begin{array}{l}
 \text{c, secondary collimator} \\
 \text{si, ith strip beam origin} \\
 \text{S, water surface} \\
 \text{Z, depth position}
 \end{array} \right)$$

$$\left(\begin{array}{l}
 \text{x} \\
 \text{y} \\
 \text{Ex} \\
 \text{Ey}
 \end{array} \right)$$

$$\left(\begin{array}{l}
 \text{d, drift} \\
 \text{a, air} \\
 \text{p, patient} \\
 \text{w, water} \\
 \text{t, total}
 \end{array} \right)$$

$$\begin{array}{l}
 \text{parameter} \\
 \text{of interest}
 \end{array}
 \cdot
 \begin{array}{l}
 \text{physical} \\
 \text{contribution} \\
 \text{to parameter}
 \end{array}$$

In the description of the algorithm the mathematical definition of each of the sigma's will not be given in order to keep the explanation as brief as possible.

However, the physical meaning of each sigma will be given as it is encountered. For a more complete explanation of this code, and for the mathematical expressions for the sigma's, the reader should refer to the original paper describing the algorithm (Hogstrom 1989).

The dose at any point can be broken down into a component due to the photon dose and a component due to the electron dose.

$$D_{\text{total}} = D_{\text{photons}} + D_{\text{electrons}} \quad \text{eq 4-1}$$

The photon dose from a single beam can readily be found from a measured depth dose curve, since the dose beyond the electron range will be due to photons only. The photon dose is thus bremsstrahlung dose at a point beyond the practical range and corrected for beam divergence and attenuation. The total X-ray dose component from an arc can then be found as the sum of the fixed beam dose distributions for a discrete set of angles that make up the arc. Once the electron component of the dose distribution has been found it will be added to this photon distribution to obtain the total dose distribution.

The electron dose distribution is obtained through a very complex calculation. The following is an overview of the major steps involved in the calculation. Figure 4-1 shows how the patient surface is broken into strip beams, as defined by the patient collimation, and the secondary collimator. The patient anatomy and the surface collimator in planes parallel to the calculation plane are assumed to be identical to that in the plane of calculation (the X, Z plane), which allows the dose in the Y plane to be summed to form a series of strip beams. A diagram showing the plane of calculation is shown in Figure 4-2. Within any strip beam the distribution functions are assumed to be independent of X. This is reasonable since the width of the strip beam will always be small. The strip beam is characterized by its planar fluence Φ , with units of electrons/cm². The angular dependence is assumed to be gaussian in shape, as this allows it to be easily convolved with the gaussian solution to Fermi-Eyges pencil beam theory.

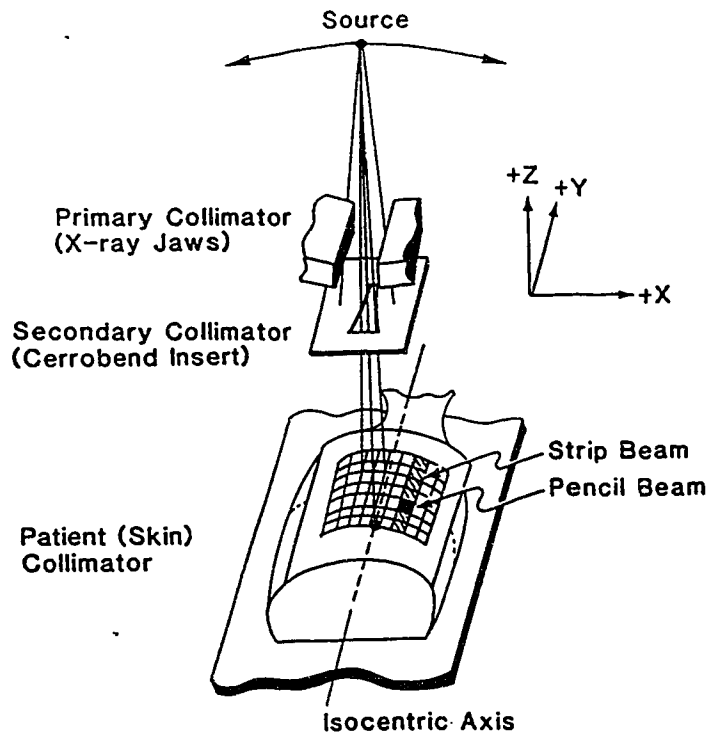


Figure 4-1 A schematic diagram showing the way in which the algorithm divides the patient into strip beams for the calculations.

The Gaussian shape is characterized by two parameters, the mean direction $\langle \Theta_X \rangle_i$, and the rms spread about the mean direction $(\sigma_{\Theta_X})_i$, which are shown in Figure 4-2. With these assumptions the planar fluence from the i_{th} strip beam can be written as.

$$\Phi_i(x_i, Y, z_i) = \int_{y_i \left(\frac{SSD-Z}{SAD} \right)}^{y_i \left(\frac{SSD+Z}{SAD} \right)} dY' \int_{\frac{\Delta x_i \left(\frac{SSD-Z}{SSD} \right)}{2}}^{\frac{\Delta x_i \left(\frac{SSD+Z}{SSD} \right)}{2}} dx \frac{1}{\sqrt{2\pi} \frac{\sigma_{x,i}}{2}} \exp\left(\frac{-(x-x_i)^2}{2 \frac{\sigma_{x,i}^2}{2}} \right) \frac{1}{\sqrt{2\pi} \frac{\sigma_{y,i}}{2}} \exp\left(\frac{-(Y'-Y)^2}{2 \frac{\sigma_{y,i}^2}{2}} \right) \Phi_i(R_i, \Theta_i, Y) \quad \text{eq 4-2}$$

Where Δx_i is the width of the i_{th} pencil beam projected on the plane perpendicular to the mean direction $\langle \Theta_X \rangle_i$.

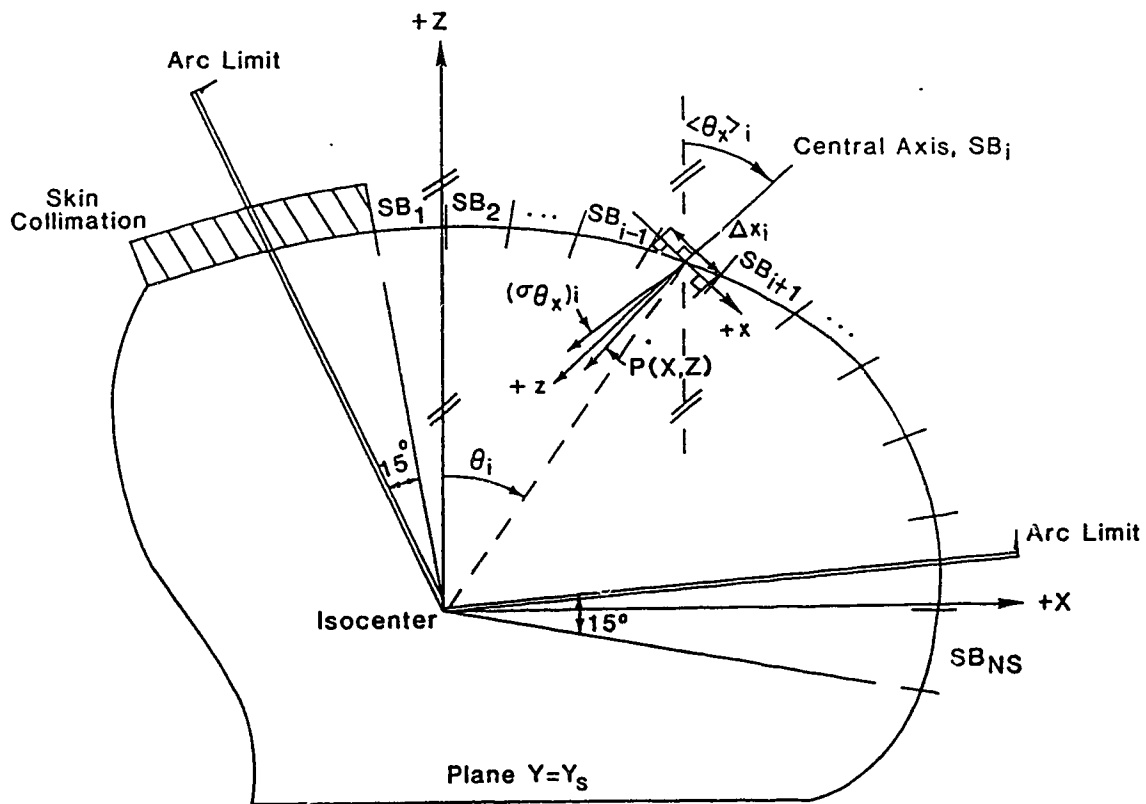


Figure 4-2 A diagram of the plane of calculation showing the calculation parameters of the i_{th} strip beam

Y_S and Y_I are the superior and inferior limits of the collimator in the Y direction.

$\sigma_{x,t}$ is the rms value of the lateral spatial distribution projected onto the XZ plane for a pencil beam originating in the i_{th} strip, S_i , and being transported to depth z_i .

$\sigma_{y,t}$ is the rms value of the lateral spatial distribution projected onto the YZ plane for a pencil beam originating in the i_{th} strip, S_i , and being transported to depth z_i .

$\Phi_i (R_i, \Theta_i, Y')$ is the planar fluence of the i_{th} pencil beam at the surface of the patient.

R_i is the radial distance from the isocentre to the surface.

SSD is the source to surface distance.

SAD is the source to isocentric axis distance.

The two σ values are different since the σ in the XZ plane will include the angular dependence due to multiple coulomb scattering and that due to geometrical considerations from the arcing motion, while the σ in the YZ plane only includes contributions from multiple coulomb scattering.

This takes the sum of the contributions to the point (x_i, Y', z_i) from all the points across the pencil beam in the X direction. The fluence will be a constant over this very small distance, therefore, the integral in X is easily solvable. The integral in Y sums the contributions from all the pencil beams at x_i , thus forming a strip beam. This integral is also solvable if the fluence is assumed to be a slowly varying function of Y, therefore, it is taken out of the integral. Therefore, the solution to equation 4-2 is

$$\Phi_i(x_i, Y, z_i) = \frac{1}{2} \left[\operatorname{erf} \left(\frac{\frac{\Delta x_i}{2} \left(\frac{SSD+Z_i}{SSD} \right) + x_i}{\sqrt{2} \frac{\sigma_{x,z}}{2}} \right) + \operatorname{erf} \left(\frac{\frac{\Delta x_i}{2} \left(\frac{SSD+Z_i}{SSD} \right) - x_i}{\sqrt{2} \frac{\sigma_{x,z}}{2}} \right) \right] \Phi_i(R_i, \Theta_i, Y) \quad \text{eq 4-3}$$

$$\frac{1}{2} \left[\operatorname{erf} \left(\frac{Y_{S_i} \left(\frac{SSD+Z_i}{SAD} \right) - Y}{\sqrt{2} \frac{\sigma_{y,z}}{2}} \right) + \operatorname{erf} \left(\frac{Y_{I_i} \left(\frac{SSD+Z_i}{SAD} \right) - Y}{\sqrt{2} \frac{\sigma_{y,z}}{2}} \right) \right]$$

This is the planar fluence of the i_{th} strip beam, which is defined as the number of electrons per unit area crossing a plane that is:

- 1) Parallel to the isocentric axis
- 2) Perpendicular to the mean direction of the i_{th} strip beam
- 3) Contains the origin of the i_{th} strip beam.

The dose to water is defined as the product of the fluence and the mass collisional stopping power. Therefore, to get the dose to water the planar fluence must be converted to fluence, and multiplied by the stopping power. The factor $F(z_{eff})$ is defined to be this conversion factor from planar fluence to dose at depth z_{eff} . Where the depth z is converted to an equivalent depth in a water phantom and is called the effective depth z_{eff} .

$$D_{e}^{i}(x_i, Y, z_i) = \Phi_i(x_i, Y, z_i) F(z_{eff}) \quad \text{eq 4-4}$$

where D_{e}^{i} is the dose contribution from the electron component at point P from the i_{th} strip beam

The factor $F(z)$ can be solved for analytically by comparing the calculated central axis depth dose (CADD) to the measured (CADD) for a stationary beam.

This gives $F(z)$ to be

$$F(z) = \Phi_0^{-1} \left(\frac{SSDR + Z}{SCD} \right)^2 \left[\operatorname{erf} \left(\frac{WXRZ}{2\sqrt{2} \sigma_{x,z}} \right) \operatorname{erf} \left(\frac{WYRZ}{2\sqrt{2} \sigma_{y,z}} \right) \right]^{-1} D_{ref}(0,0,z) \quad \text{eq 4-5}$$

where $WXRZ$ is the X dimension of the reference field size at depth z , where the reference field size refers to the size of the field for the data input into the algorithm.

$WYRZ$ is the Y dimension of the reference Field Size at depth z .

Φ_0 is the central axis value of the planar fluence defined at the level of the secondary collimator.

D_{ref} is the measured CADD as a function of depth Z.

SSDR is the distance from the source to the surface under the reference measurements conditions.

SCD is the distance from the source to the secondary collimator.

σ_{xt} is the rms value of the projected lateral spatial distribution of a pencil beam originating within the secondary collimator and being transported to depth Z in the water phantom.

The total planar fluence of the i_{th} strip beam can be found by summing the contributions to the i_{th} beam from each gantry position in the arc. The planar fluence contribution from the j_{th} gantry position to the i_{th} strip Φ_{ij} beam can be calculated using the Fermi-Eyges theory of electron transport again.

$$\Phi_{ij}(x_{ij}, Y, SSD_{ij}) = \left(\frac{SCD}{SSD_{ij}}\right)^2 \int_{-W_X(SSD_{ij}/ZSAD)}^{W_X(SSD_{ij}/ZSAD)} dx' \int_{-W_Y(SSD_{ij}/ZSAD)}^{W_Y(SSD_{ij}/ZSAD)} dY' \quad \text{eq 4-6}$$

$$\times \Phi_0^j(y') \frac{1}{2\pi \sigma_x^2 \sigma_y^2} \exp\left(-\frac{(x_{ij} - x')^2 + (Y - Y')^2}{2 \sigma_x^2 \sigma_y^2}\right)$$

where SSD_{ij} is the central axis source to surface distance of the i_{th} strip beam

x_{ij} is the off axis distance of the i_{th} strip beam relative to the j_{th} gantry position

$\Phi_0^j(y')$ is the planar fluence at the level of the secondary collimator at the

off axis position y' for the j_{th} gantry position. (this is a slowly varying function compared to the exponential and is therefore removed from the integral)

$\sigma_{x,t}$ is the rms value of the projected spatial distribution of a pencil beam originating in the secondary collimator and being transported through air to a plane containing the origin of the i_{th} strip beam and perpendicular to the j_{th} gantry position.

Solving this gives the planar fluence passing through a plane perpendicular to the central axis of the j_{th} gantry position at the origin of the i_{th} strip beam. In order to get the planar fluence through a plane perpendicular to the i_{th} strip beam, Φ_{ij} must be multiplied by $\cos(\langle\Theta_x\rangle_i - \Theta_j)$.

$$\Phi_{ij}(\Theta_i, R_i, Y) = \Phi_{ij}(x_{ij}, Y, SSD_{ij}) \cos(\langle\Theta_x\rangle_i - \Theta_j) \quad \text{eq 4-7}$$

To get the total planar fluence of the i_{th} strip beam Φ_{ij} must be summed over all the gantry angles. If the beam has a constant intensity at all points in the arc, the total planar fluence at $x=0, y=Y$ in the rotating coordinate system will be

$$\Phi_o(Y) = N \Phi_o^j(Y) \quad \text{eq 4-8}$$

where the arc has been broken down into N equally spaced gantry positions. Combining Equations 4-6, 4-7, and 4-8 yields the total planar fluence for the i_{th} strip beam, which becomes

$$\Phi(\Theta_i, R_i, Y) = \sum_{j=1}^N \frac{1}{N} \Phi_o(Y) \left(\frac{SSD}{SSD_{ij}} \right)^2 \frac{1}{2} \left[\operatorname{erf} \left(\frac{1Wx \left(\frac{SSD_{ij}}{SAD} \right) + x_{ij}}{\sqrt{2} c_{s1} \sigma_{x,t}} \right) + \operatorname{erf} \left(\frac{1Wx \left(\frac{SSD_{ij}}{SAD} \right) - x_{ij}}{\sqrt{2} c_{s1} \sigma_{x,t}} \right) \right] \cos((\Theta_{\eta_i} - \Theta_j)) \frac{1}{2} \left[\operatorname{erf} \left(\frac{1Wy \left(\frac{SSD_{ij}}{SAD} \right) + Y}{\sqrt{2} c_{s1} \sigma_{x,t}} \right) + \operatorname{erf} \left(\frac{1Wy \left(\frac{SSD_{ij}}{SAD} \right) - Y}{\sqrt{2} c_{s1} \sigma_{x,t}} \right) \right] \quad \text{eq 4-9}$$

This total strip beam fluence can then be converted into the strip beam dose by combining equation 4-9 with 4-4, along with 4-3 and 4-5. This gives the dose distribution from the i_{th} strip beam to be

$$D_e^i(x_i, Y, z_i) = W_i \frac{\Phi_o(Y)}{\Phi_o} \left(\frac{SSDR + Z_{eff}}{SSDR} \right)^2 \left[\operatorname{erf} \left(\frac{wXRZ}{2\sqrt{2} c_{s2} \sigma_{x,t}} \right) \operatorname{erf} \left(\frac{wYRZ}{2\sqrt{2} c_{s2} \sigma_{x,t}} \right) \right]^{-1} D_{rad}(0,0,Z_{eff}) \frac{1}{2} \left[\operatorname{erf} \left(\frac{\Delta x_i \left(\frac{SSD+Z_i}{SSD} \right) + x_i}{\sqrt{2} c_{s1} \sigma_{x,t}} \right) + \operatorname{erf} \left(\frac{\Delta x_i \left(\frac{SSD+Z_i}{SSD} \right) - x_i}{\sqrt{2} c_{s1} \sigma_{x,t}} \right) \right] \frac{1}{2} \left[\operatorname{erf} \left(\frac{y_{s_i} \left(\frac{SSD+Z_i}{SAD} \right) - Y}{\sqrt{2} c_{s2} \sigma_{y,t}} \right) + \operatorname{erf} \left(\frac{y_{t_i} \left(\frac{SSD+Z_i}{SAD} \right) - Y}{\sqrt{2} c_{s2} \sigma_{y,t}} \right) \right] \quad \text{eq 4-10}$$

Where the weighting factor W_i is defined to be

$$W_i = \frac{1}{N} \sum_{j=1}^N \left(\frac{SSDR}{SSD_{ij}} \right)^2 \cos((\Theta_{\eta_i} - \Theta_j)) \frac{1}{2} \left[\operatorname{erf} \left(\frac{1Wx \left(\frac{SSD_{ij}}{SAD} \right) + x_{ij}}{\sqrt{2} c_{s1} \sigma_{x,t}} \right) + \operatorname{erf} \left(\frac{1Wx \left(\frac{SSD_{ij}}{SAD} \right) - x_{ij}}{\sqrt{2} c_{s1} \sigma_{x,t}} \right) \right] \frac{1}{2} \left[\operatorname{erf} \left(\frac{1Wy \left(\frac{SSD_{ij}}{SAD} \right) + Y}{\sqrt{2} c_{s1} \sigma_{x,t}} \right) + \operatorname{erf} \left(\frac{1Wy \left(\frac{SSD_{ij}}{SAD} \right) - Y}{\sqrt{2} c_{s1} \sigma_{x,t}} \right) \right] \quad \text{eq 4-11}$$

Finally the electron component of the dose distribution can now be solved for at any point in the XZ plane at position Y, by summing D_e^i over all possible strip beams. The complete dose distribution is then found by summing the electron and photon dose components at each point of interest, as given in equation 4-1.

The algorithm thus uses a measured depth dose curve and a profile at d_{\max} to execute the electron dose calculation section of the algorithm. It also uses a profile for the bremsstrahlung tail in the calculation of the photon component of the dose. The algorithm thus takes very little time to implement since it does not require large amounts of data to be measured.

Many assumptions have been made either in Fermi-Eyges theory or in order to make the algorithm fast enough to be used clinically. The following is a summary of the major assumptions :

1) All inhomogeneities found along the central axis of the pencil beam are assumed to be infinite in extent in the dimension perpendicular to the arc (2D assumption).

2) The medium is layered in a slab geometry such that the electron energy and scattering power change only as a function of depth.

3) Only electrons scattered by small angles are included in the electron fluence distributions

4) The fluence distribution includes only primary electrons, ignoring secondary delta rays and back scattered electrons as well as bremsstrahlung photons produced in the patient.

5) The theory yields planar fluence, for which the conversion to dose is only approximate.

6) The dose within the heterogeneous medium is not directly calculated. The dose to water inside the heterogeneity is calculated, and the heterogeneity is

accounted for in the calculation of a depth scaled by a linear stopping power ratio derived from CT data.

7) The electrons are assumed to lose their energy linearly with depth (Continuous Slowing Down Approximation), and energy-loss straggling is ignored.

8) The lateral scattering of electrons increases monotonically, thus propagating them beyond their finite range.

The algorithm makes up for some of these assumptions by forcing the calculated values to match measured values such as the depth dose curve, which is an input parameter to the algorithm. In order to account for the inhomogeneities the algorithm actually forces the calculated dose at depth z to match the dose at the effective depth z_{eff} in the water phantom. By using measured data the algorithm compensates for assumptions 4, 5, 7, and 8. By making the approximation that there are no large angle scattering events the pencil beam can be assumed to have a gaussian shape, which makes the Eyges solution to Fermi's electron transport equation easily solvable.

CHAPTER 5 RESULTS AND DISCUSSION

5.1 COMPARISON OF DOSIMETERS

For any measurements accuracy is always an important factor. Therefore, the accuracy of all of the dosimeters used in these experiments were verified by a comparison to a "standard" dosimeter. It is generally agreed that the standard dosimeter should be an ion chamber with associated electrometer whose calibration is traceable to a National Standards laboratory. Therefore, before any of the dosimeters were used the measurements obtained with that dosimeter were compared to measurements done with an ion chamber. The first such test was to show that the depth dose measured with a diode was the same as that obtained with the ion chamber. A diode is a more practical dosimeter for an electron beam since it measures dose directly, where as the ion chamber measures the amount of ionization, which must be corrected by an energy, and hence depth dependent factor in order to get the absorbed dose. Figure 5-1 shows the percentage depth dose measured with an ion chamber and with the diode. The ion chamber readings have been corrected according to the energy of the electrons at depth to give the proper depth dose curve. This involves using a look up table to convert the amount of ionization at a given energy to the absorbed dose. A sample of this type of calculation is shown in Appendix 1. This shows that the diode does in fact give a true measure of the absorbed dose in water. Therefore, the data gathered with the diode was assumed to be valid. The electron arc algorithm requires as an input the depth dose curve and a series of profiles measured in water under a reference field size. This information was measured with a diode and entered into the algorithm thus allowing the latter to be used for these experiments. The diode is very useful for

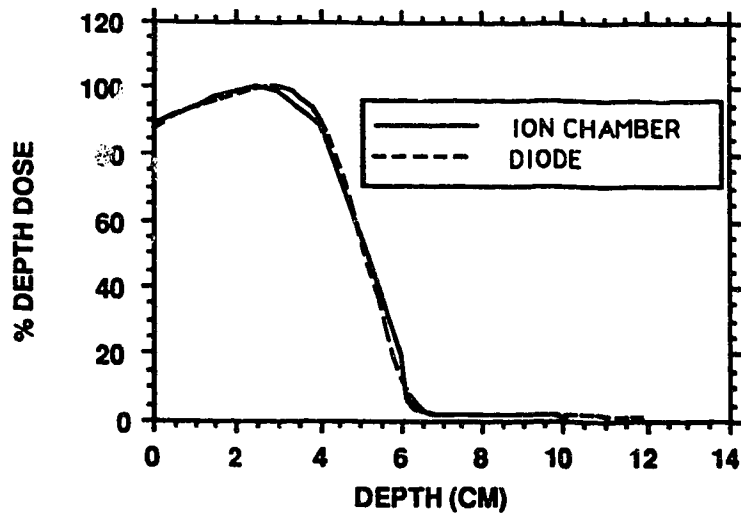


Figure 5-1 (a) Percentage depth dose measured in water with an ion chamber and with a diode for a 12 MeV electron beam.

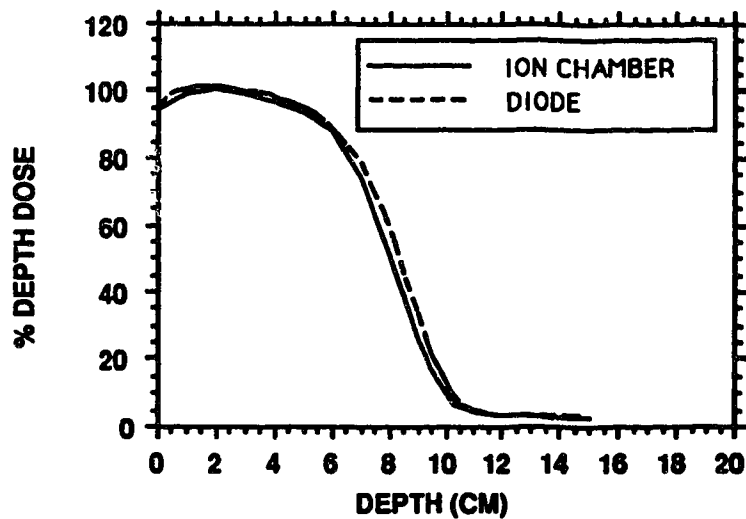


Figure 5-1 (b) Percentage depth dose measured in water with an ion chamber and with a diode for a 20 MeV electron beam.

measuring electron beam dose distributions in water, but, for the arc irradiations a solid polystyrene phantom is used. The diode, therefore, is not a practical dosimeter for these experiments. Film is the most practical dosimeter for this type of experimental setup, as it integrates the total dose and has excellent spatial resolution. The accuracy of the film response is verified by comparing the PDD measured with film in polystyrene to that measured in water with the diode. The PDD's match very well as is shown in Figure 5-2. The depth dose, therefore, provides a validation of the film as a reliable dosimeter in the context of these studies. Since the electron beam energy will decrease with depth, it is important that the response is linear at all energies. This curve is a better indicator of the film response than a simple H - D curve which only shows the dose response at one energy. There is, however, a small region near the surface where the film response is different from the diode. This difference has been observed by others, and many different factors have been postulated as the reasons for the difference. However, at this point this remains unresolved. The film response can therefore be assumed to be accurate everywhere except within this narrow region near the surface. However, even in this region the response is quite close to the diode measurements.

5.2 HOMOGENEOUS PHANTOM

5.2.1 RESULTS

To evaluate the electron arc algorithm the dose distributions were calculated and compared for simple setups, and then more complex phantoms which would stress the algorithm were used. These more complex configurations would point out worst case differences between the measured and

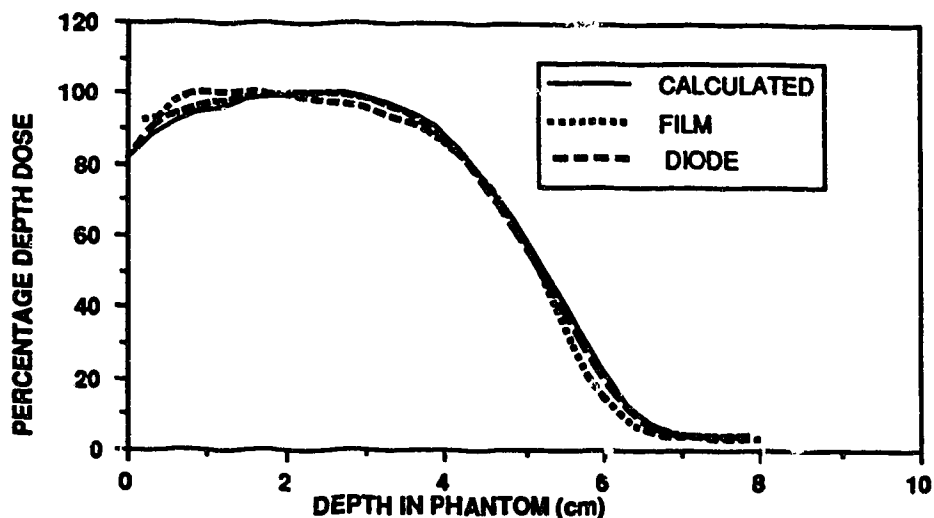


Figure 5-2 (a) Percentage depth dose measured with film and a diode, and calculated with the electron arc algorithm for a 12 MeV stationary electron beam.

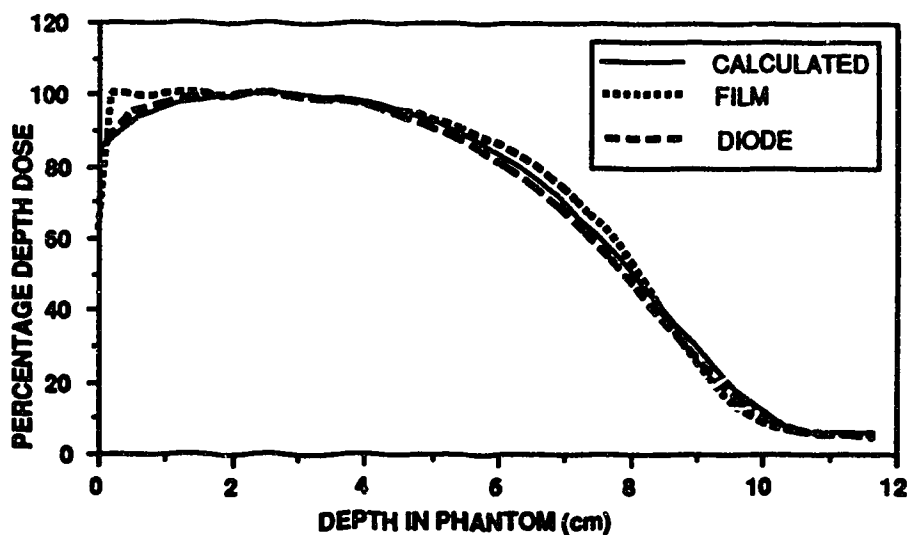


Figure 5-2 (b) Percentage depth dose measured with film and a diode, and calculated with the electron arc algorithm for a 20 MeV stationary electron beam.

calculated dose distributions. The data presented up to this point has all been in the form of depth dose curves. This is sufficient to prove that the dosimeter is responding properly. Nevertheless, when comparing calculated results to measured data it is vital that the dose be compared everywhere in the plane of calculation. This can be accomplished in various ways. The most common is to overlay two sets of isodose curves on one diagram. This method works reasonably well. However, in regions where the dose is relatively constant small differences in dose can cause the distance between isodose lines to be large. Conversely in a region where the dose changes rapidly, a large difference in dose will appear as a very slight displacement of the isodose line. Therefore, this method can cause some misinterpretation of the results. In order to avoid this, difference maps will be presented along with the isodose curves for the measured and calculated dose distributions. The first dose and difference maps shown are for the simplest case, which is for a stationary beam on a flat phantom. Figures 5-3 and 5-4 are for the 12 and 20 MeV beams respectively. Although this is a stationary beam set up the arc algorithm was used for the calculation, with an arc of zero degrees. In a clinical situation this algorithm would not be used to calculate the dose for a stationary beam set up, but it may provide some interesting starting results. The difference maps will be used to emphasize the areas where the two dose matrices are different, one will show areas where the measured dose is greater than the calculated, and the other will show where the calculated dose is greater than the measured. These final two maps come from a simple digital subtraction of the two dose matrices. Since the distributions around the arc, or on the flat phantom, are symmetric the isodose and difference maps are cut in half with the measured distributions in the upper

left (a), and the calculated distributions in the upper right (b) of the figures. The lower map shows areas where the measured dose is greater than the calculated dose on the left (c), and on the right (d) the areas where the calculated dose is greater than the measured dose. This format will be followed for all of the dose and difference maps presented in this study. The phantom used was a cubical shaped piece of polystyrene, with a piece of film sandwiched in the center of the phantom. The film was aligned along the radial plane in the middle of the beam. The phantom was positioned such that the source to surface distance (SSD) was 82.5 cm, to be consistent with future experiments with the cylindrical phantom. In this case the calculated distribution should reproduce the measured depth dose curve which was entered into the algorithm, because the algorithm forces the output to match the input depth dose. Therefore, the main question that will be answered by this experiment is how well the calculation predicts the penumbral region of the beam. Figures 5-3 and 5-4 show that the predicted dose matches the measured dose along the central axis within about 2 mm even in the very high dose gradient region beyond d_{max} . However, this is not the case in the penumbra. The measured dose is as much as 20 % higher than the calculated dose in this region. These differences in dose do occur in a very high dose gradient area, and they correspond to a maximum difference between the position of the isodose lines of about 3 - 4 mm at d_{max} for both energies. This difference of several millimeters would not be considered to be very significant for a stationary beam algorithm, but such slight differences may cause a substantial error in an arc calculation, because the dose from the penumbra of the beam makes up a significant fraction of the total dose to any given point in an arc irradiation. The information presented in these last two figures is not clinically

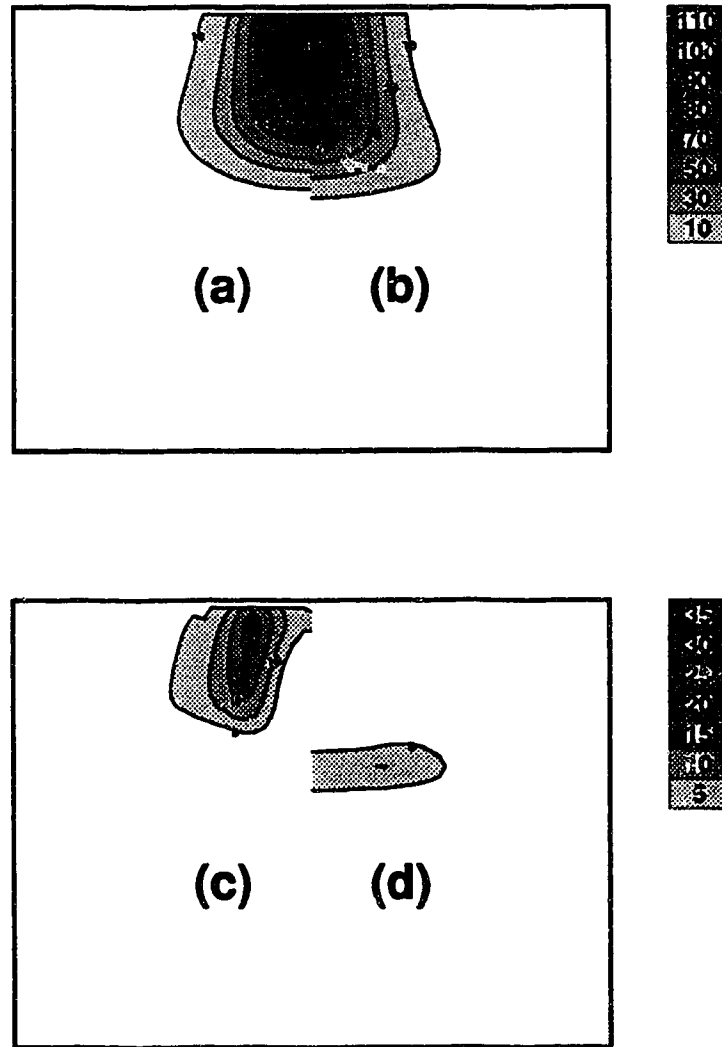


Figure 5-3 Isodose and Difference maps for an arc of 0 degrees with a 12 MeV beam incident on a flat phantom.

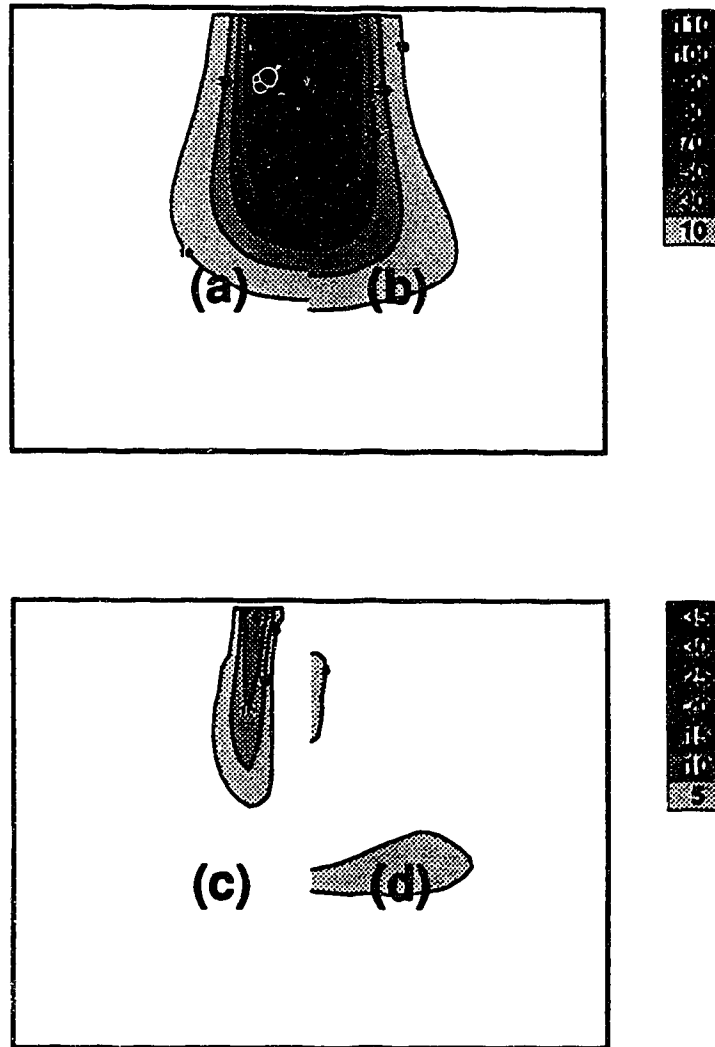


Figure 5-4 Isodose and Difference maps for an arc of 0 degrees with a 20 MeV beam incident on a flat phantom.

relevant, since all single stationary beam treatment plans would be done using an algorithm written specifically for the stationary electron beam treatment planning, and the accelerator would be set up using a different method of collimating the beam. This information may, however, provide insight into some of the areas that are causing the arc algorithm to break down.

The next obvious progression from simple phantoms to more elaborate geometries was to test the algorithm for a simple arc on a homogeneous phantom. In this case the phantom described in Chapter 3 was used. The phantom was put together such that the inhomogeneous sections were outside of the radiation beam, and thus would not affect the dose distributions. The set up was such that the isocenter of the linac was at the center of the phantom. This ensured that the SSD would be the same throughout the arc (82.5 cm). In all cases where the cylindrical phantom was used there is a region on either side of center where the film had to be cut out to allow the phantom to be assembled. The data in this region should, therefore, be ignored. Again the isodose and difference maps are presented. Figures 5-5 and 5-6 present this data for the 12 and 20 MeV arcs, from which it can be seen that there are some differences between the predicted and measured results. The major areas of difference occur in the build-up region, and are as high as 15 % in some areas. In the penumbra there is also a region in which the calculated dose is as much as 10 % higher than the measured dose.

5.2.2 DISCUSSION

The goal of this work on the homogeneous phantom was to determine if the arc algorithm can accurately predict the dose from an electron arc irradiation. We have shown with one dosimeter (film) that this is not strictly the case.

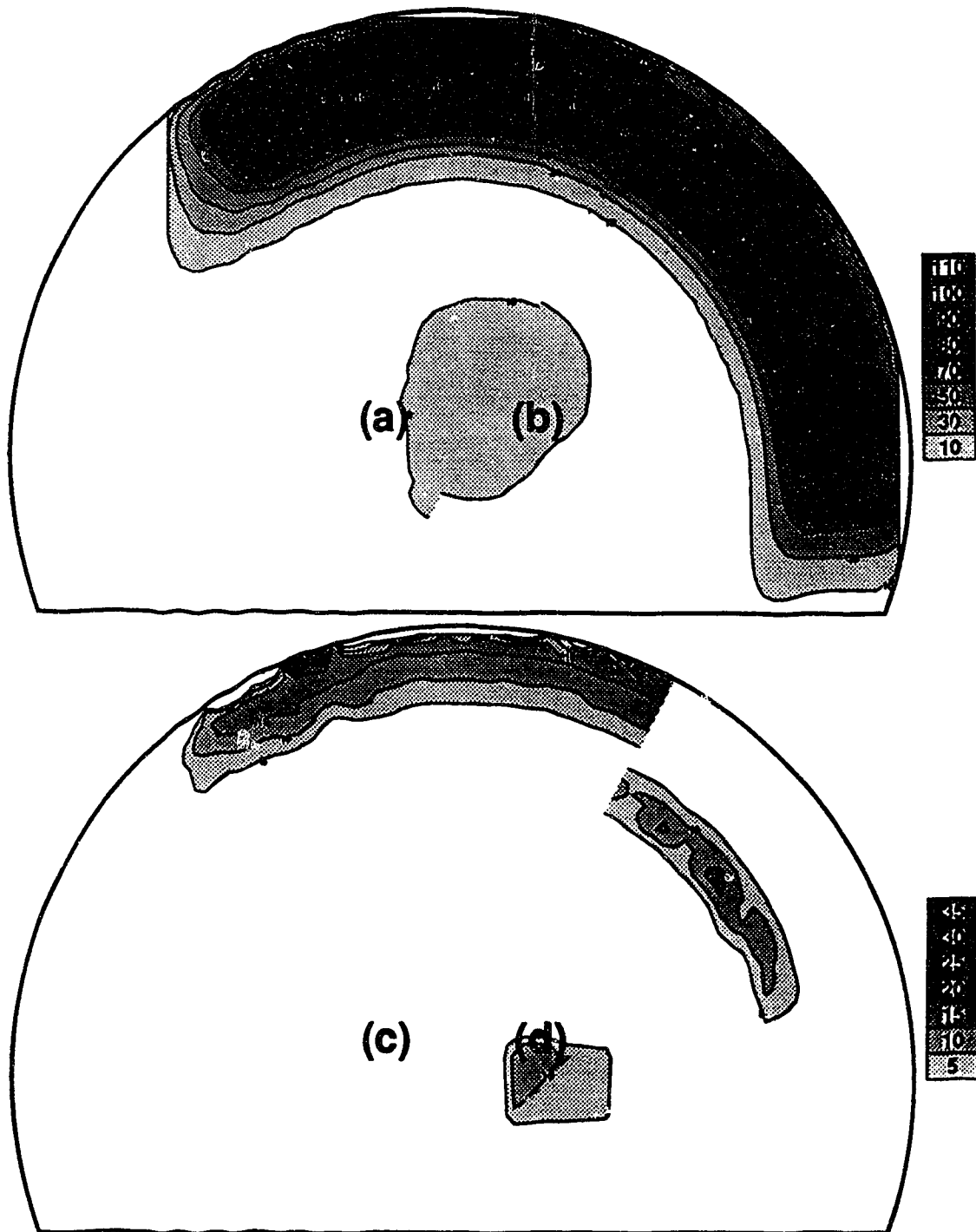


Figure 5-5 Isodose and Difference maps for an arc of 145 degrees with a 12 MeV beam incident on a homogeneous cylindrical polystyrene phantom.

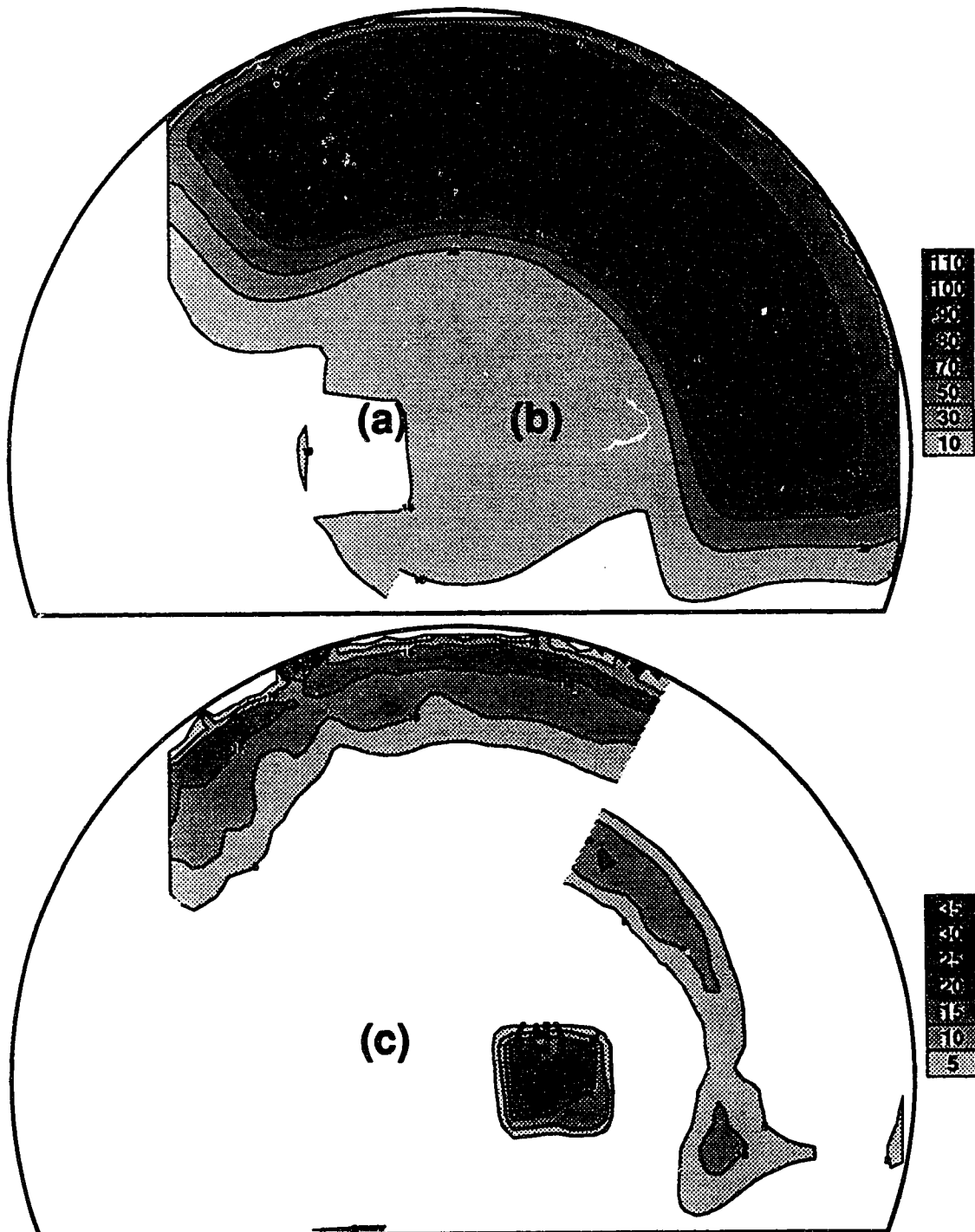


Figure 5-6 Isodose and Difference maps for an arc of 145 degrees with a 20 MeV beam incident on a homogeneous cylindrical polystyrene phantom.

Therefore, in order to verify that the film was responding correctly in the arc irradiation a depth dose curve was measured with LiF thermoluminescent dosimeters (TLD). Figure 5-7 presents the depth dose curve measured with the TLD's for both energies, as well as the depth dose curves derived from the measured and calculated distributions shown in Figures 5-5 and 5-6. This experiment again verifies the validity of the film as a dosimeter. This also shows a discrepancy between the film and TLD near the surface, especially for 20 MeV, but the response matches that measured with TLD quite well after the first two centimeters. An accuracy of $\pm 2\%$ was assumed for the film measurements as reported by Dutreix (Dutreix and Dutreix 1969), and a $\pm 3\%$ accuracy as is commonly associated with TLD measurements. The error of the normalized value is actually double the error in a single measurement, therefore, the total errors are $\pm 4\%$ and $\pm 6\%$ respectively. Within error the film and TLD measurements are in complete agreement for the 12 MeV and deviate only between 0-2 cm for the 20 MeV beam. The calculated values are significantly lower than both measured values in the build up region, and they show a deeper d_{max} for both energies. All of these curves are normalized to the depth of maximum dose for the TLD measurements. Had they been normalized to their own maximum dose which may occur at a different depth, the calculated PDD would be much lower than the measured values in the build up region, but they would appear to match better beyond d_{max} .

Therefore, the TLD measurements confirm that the data shown in Figures 5-5 and 5-6 is correct, and that the differences between the data measured with film and the calculated data do actually exist. This shows that the algorithm is not modelling the arc irradiation correctly in the build up region. These errors are

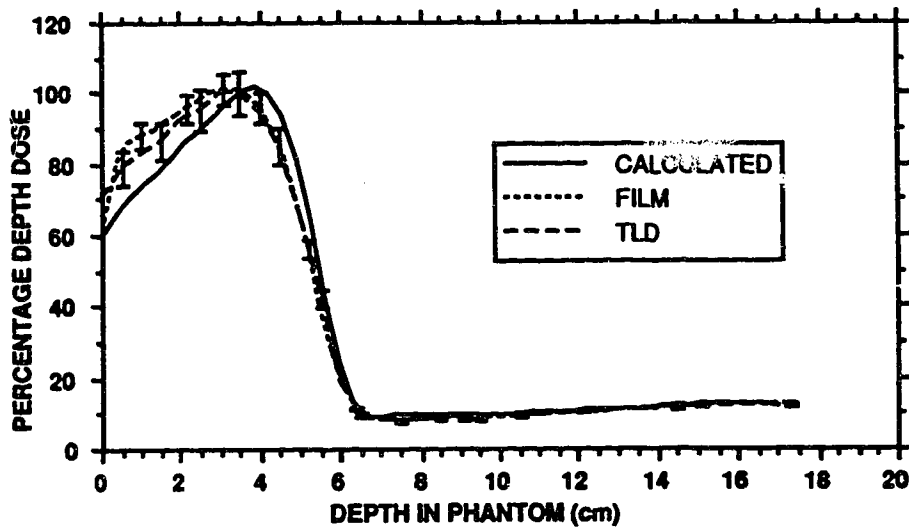


Figure 5-7(a) Percentage depth doses measured with film and TLD and calculated using the electron arc algorithm for a 145 degree irradiation on a homogeneous phantom with a 12 MeV electron beam.

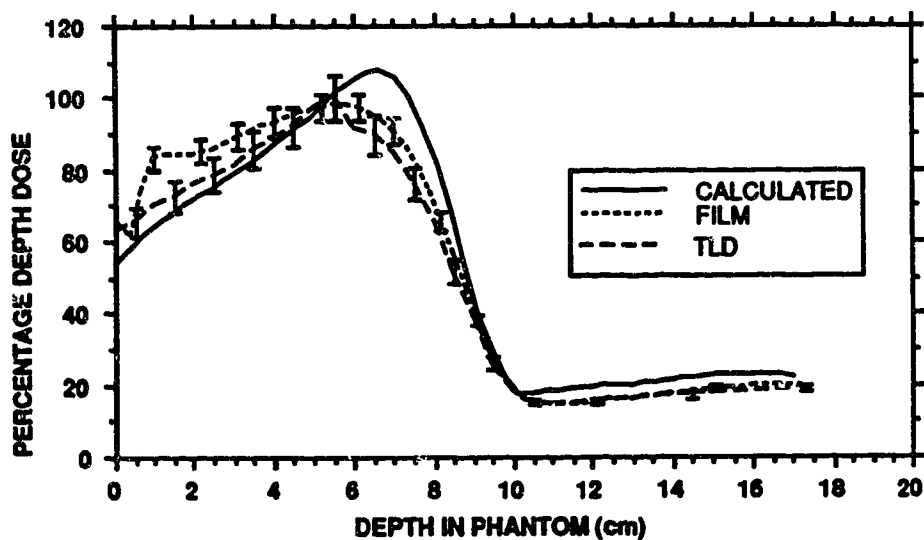


Figure 5-7(b) Percentage depth doses measured with film and TLD and calculated using the electron arc algorithm for a 145 degree irradiation on a homogeneous phantom with a 20 MeV electron beam.

possibly due to the differences that were found in the penumbra for the stationary beam irradiation. In an arc irradiation the penumbra of the stationary beam makes up a large portion of the dose, therefore, differences of a few millimeters in the penumbra of the stationary distribution could be the cause of the differences that are apparent in the arc distribution. To test this hypothesis the arc dose distribution was calculated by taking the calculated stationary beam dose matrix and rotating it in one degree intervals and summing the dose matrix from each interval. If the arc algorithm is working properly we would expect that the dose matrix from both methods would be the same. This is in fact the case as can be seen from the difference maps presented in Figure 5-8, as these two dose matrices show only minor differences. This indicates that the differences found between the dose matrix calculated with the arc algorithm and the measured dose matrix are due to the same factor that is causing the differences seen in the stationary beam set up. In order for this algorithm to be generally used it will need to be modified to get a better agreement between the experimental and calculated data for the simple arc on the homogeneous phantom. It would be very questionable to try to use this algorithm as it is on a patient where inhomogeneities would be present, if it is unable to predict the dose accurately for a homogeneous arc. The data presented to this point shows that the arc algorithm would produce the correct dose distribution if it could yield the correct stationary distribution. For this reason the computer code was questioned since the theory has been proven to work quite well in the stationary beam algorithm. When the code was analyzed it was found to have incorrectly modeled the input field size in order to ensure that the total dose is conserved between the calculated and input dose profile at the depth of d_{max} . This error

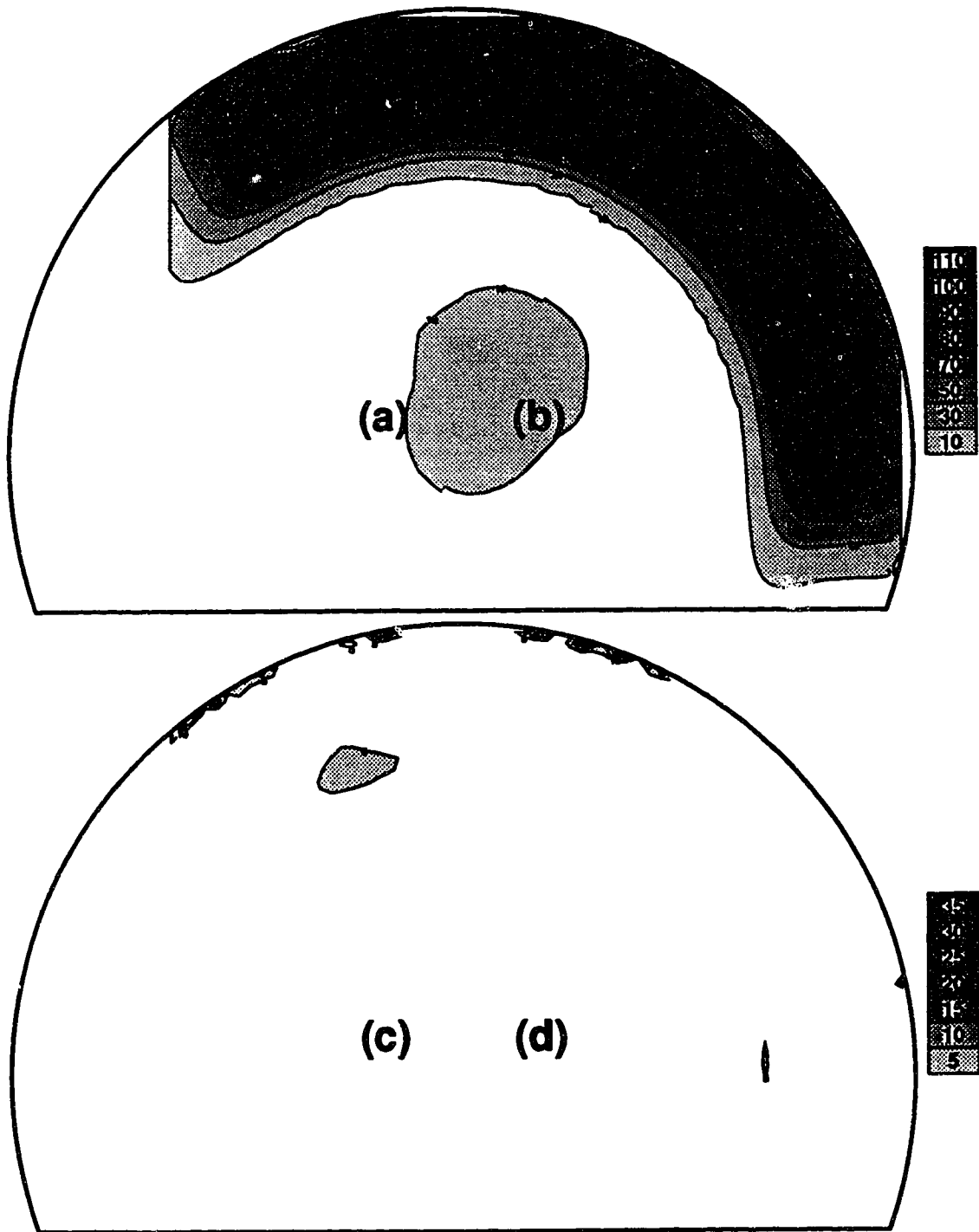


Figure 5-8 Isodose and Difference maps for an arc of 145 degrees with a 12 MeV beam calculated with a pseudo-arc technique and with the electron arc algorithm.

caused the beam profile to be shifted approximately 4 mm inside the input profile, when it should have actually shifted it to be slightly wider than the measured profile to compensate for theoretical limitations. When the code was changed to correct this mistake it produced a much better correspondence between the calculated and measured dose distributions for the stationary beam on a flat phantom. These modified distributions are shown in Figures 5-9 and 5-10. The calculated beam is now slightly wider than the measured beam profile near the surface, but in general they match very well. Again there is a slight difference in the central axis dose, but this represents a difference of only a few mm. The shape of the ten percent line is now slightly different for the measured and calculated dose distributions, but this probably will not make a big difference to the arc distributions except at the very edge of the penumbra. In Figures 5-11 and 5-12 the arc distributions are presented for the homogeneous phantom using the modified algorithm. It shows that now the differences in the build up region are substantially lower than they were before. There are a few very small areas showing a 10 % difference, but in most cases the difference is 5% in the first couple of centimeters of the build up region. Again beyond d_{max} the calculated dose is greater than the measured dose, however the difference maps now show only small regions of 5 % difference. This compares to a difference of up to 15 % in this region before the correction was made.

The data presented above shows that the modification to the algorithm has made a substantial improvement to the size of the differences found for an arc irradiation on a homogeneous phantom. For this reason the modified algorithm was used to calculate the dose distributions for the rest of the phantoms that will be presented in the next sections of this chapter.

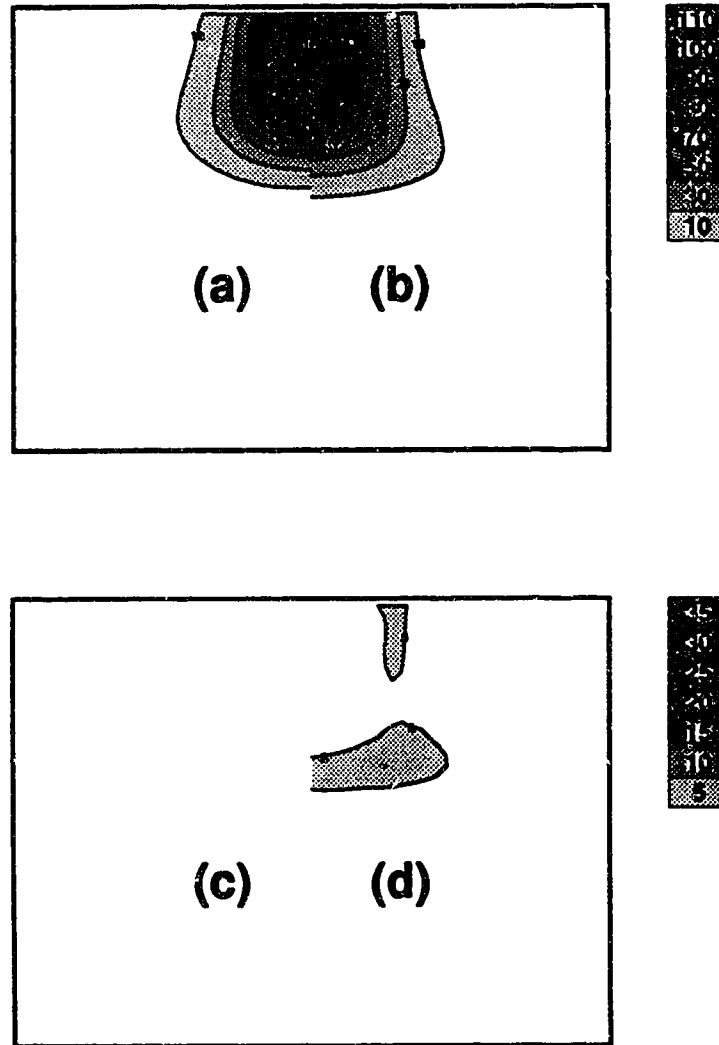


Figure 5-9 Isodose and Difference maps for an arc of 0 degrees with a 12 MeV beam incident on a flat phantom (calculated with modified arc algorithm).

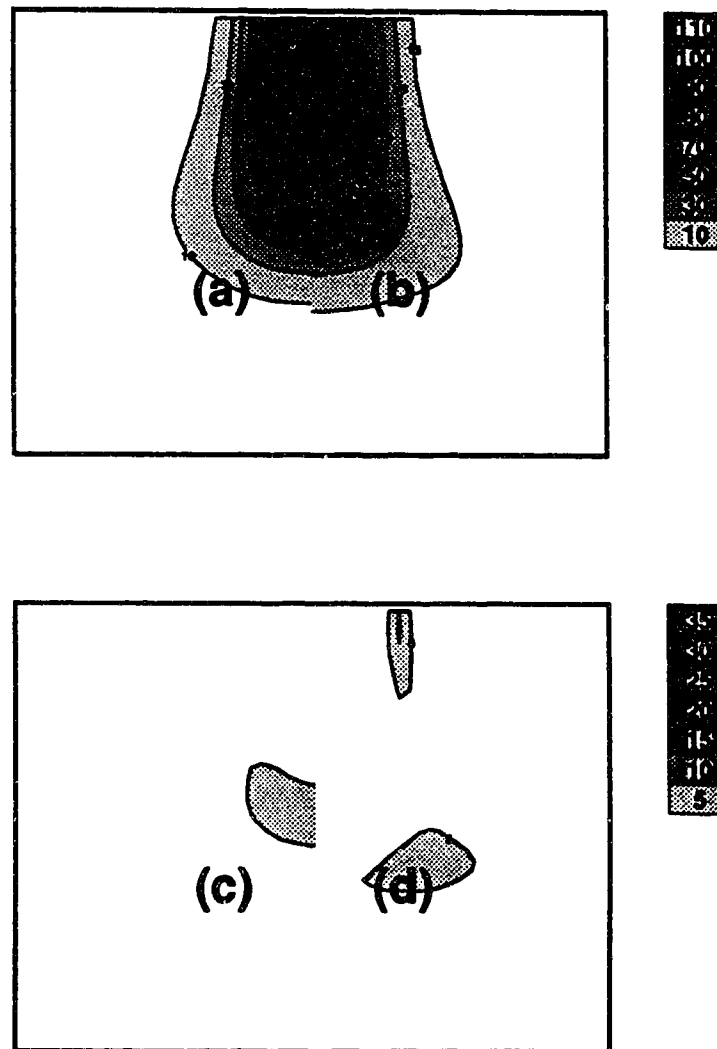


Figure 5-10 Isodose and Difference maps for an arc of 0 degrees with a 20 MeV beam incident on a flat phantom (calculated with modified arc algorithm).

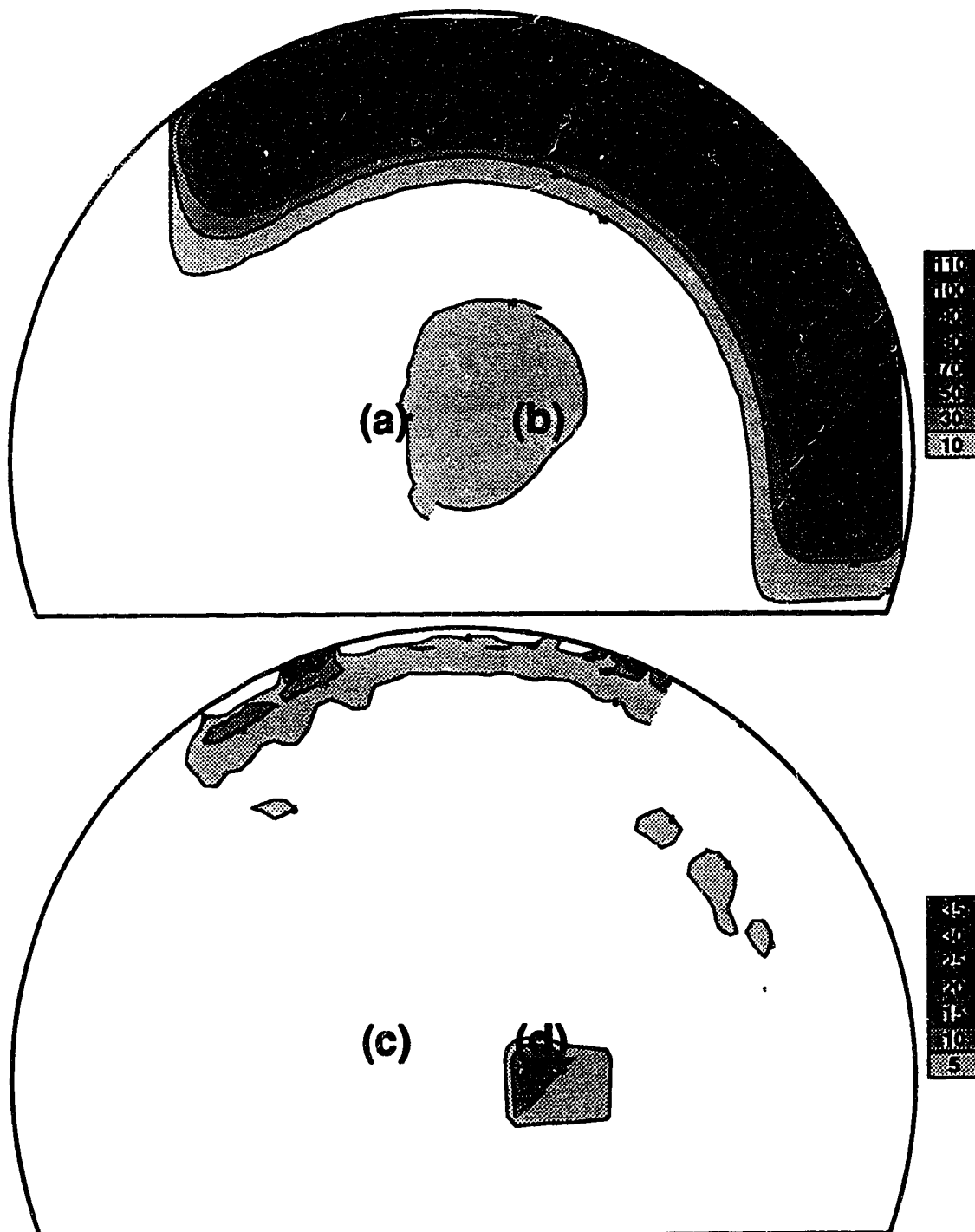


Figure 5-11 Isodose and Difference maps for an arc of 145 degrees with a 12 MeV beam calculated with modified arc algorithm.

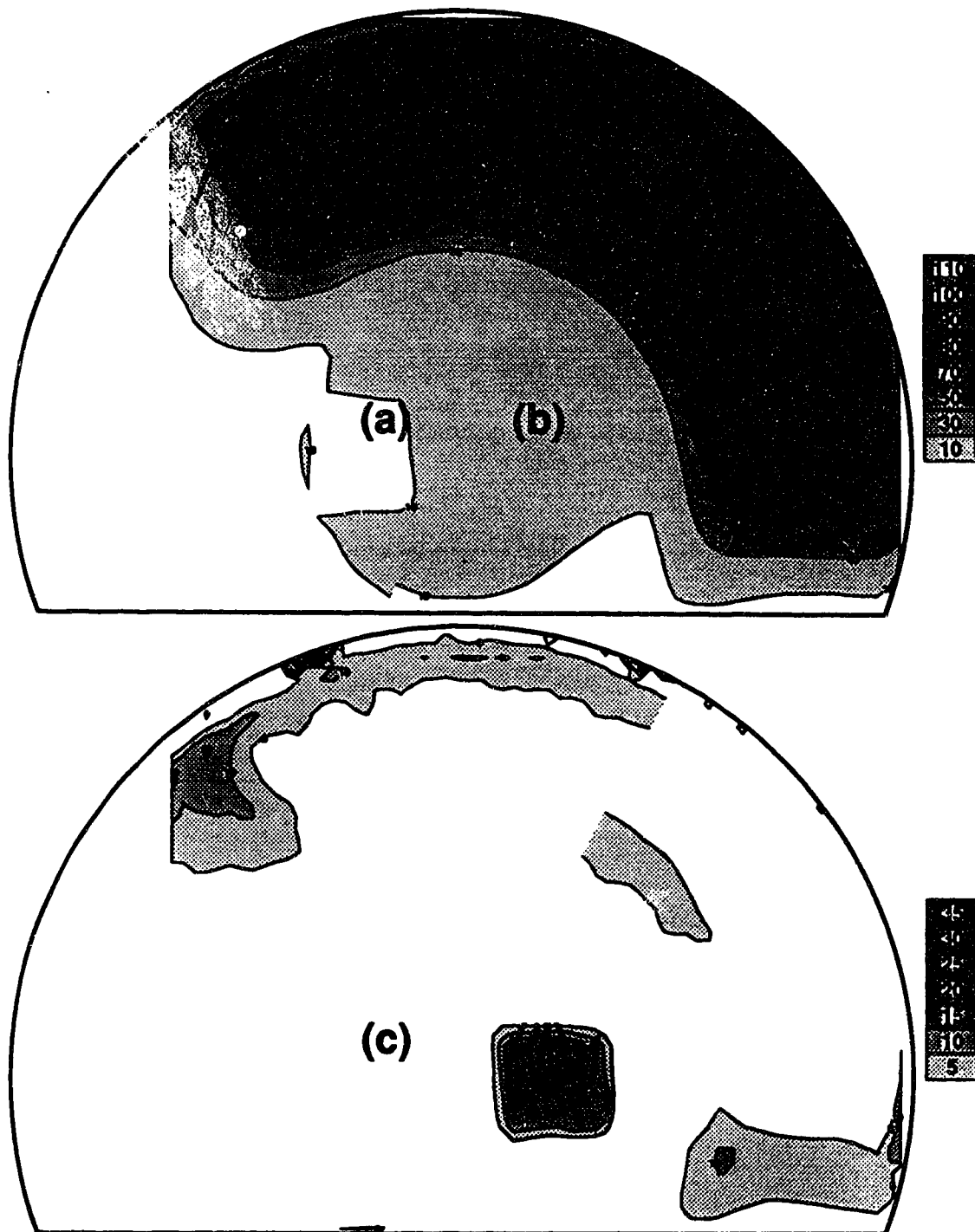


Figure 5-12 Isodose and Difference maps for an arc of 145 degrees with a 20 MeV beam calculated with modified arc algorithm.

5.3 HIGH DENSITY INHOMOGENEITIES

5.3.1 RESULTS

Introducing high density inclusions into the phantom produces expected dose perturbations, which are not accurately modelled by the algorithm. Figures 5-13 and 5-14 show the calculated and measured dose distributions for 12 and 20 MeV arcs incident on a phantom with an aluminum bar which follows the contour of the phantom similar to a rib bone in the body. The position of the inhomogeneity is outlined in the dose and difference maps and the exact position was shown in Figure 3-2. Initially the measured dose is greater than the calculated dose in the build up region. This is similar to the observations for the homogeneous phantom. However, a substantially higher dose is measured within the inhomogeneity than that which is calculated. In this region the difference is as high as 25 % in the aluminum. Such a high discrepancy cannot be attributed to the differences seen in the build up region of the homogeneous case. Later in this chapter the reason for this large difference will be elaborated upon. It is also noteworthy that the dose at the sides of the aluminum can be 15 % higher in the measured distribution than in the calculated. This would indicate that the algorithm is predicting less scatter from the aluminum. Beyond the inhomogeneity the predicted dose is up to 5 % higher than the measured dose. This then falls off, but at greater depths the measured dose again becomes greater than the calculated dose. This region shows differences which reach 25 % for both the 12 and 20 MeV beams.

Figures 5-15 and 5-16 present the data for the same set up using a hard bone analogue instead of the aluminum as an inhomogeneity. The difference and dose maps show a very similar pattern to that which was observed for the

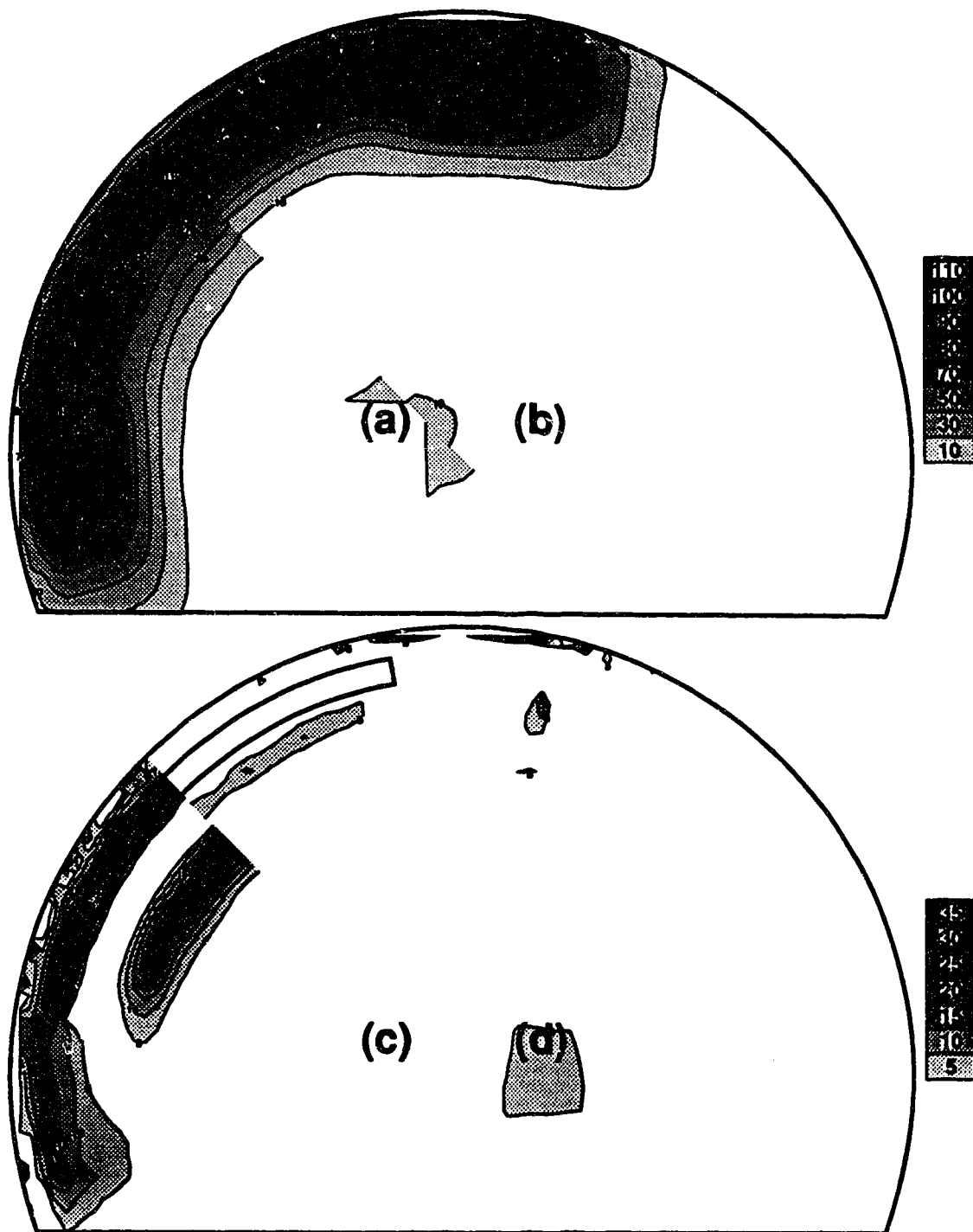


Figure 5-13 Isodose and Difference maps for an arc of 145 degrees with a 12 MeV beam incident on a phantom with an aluminum insert that follows the contour of the phantom. The position of the insert is outlined in the maps.

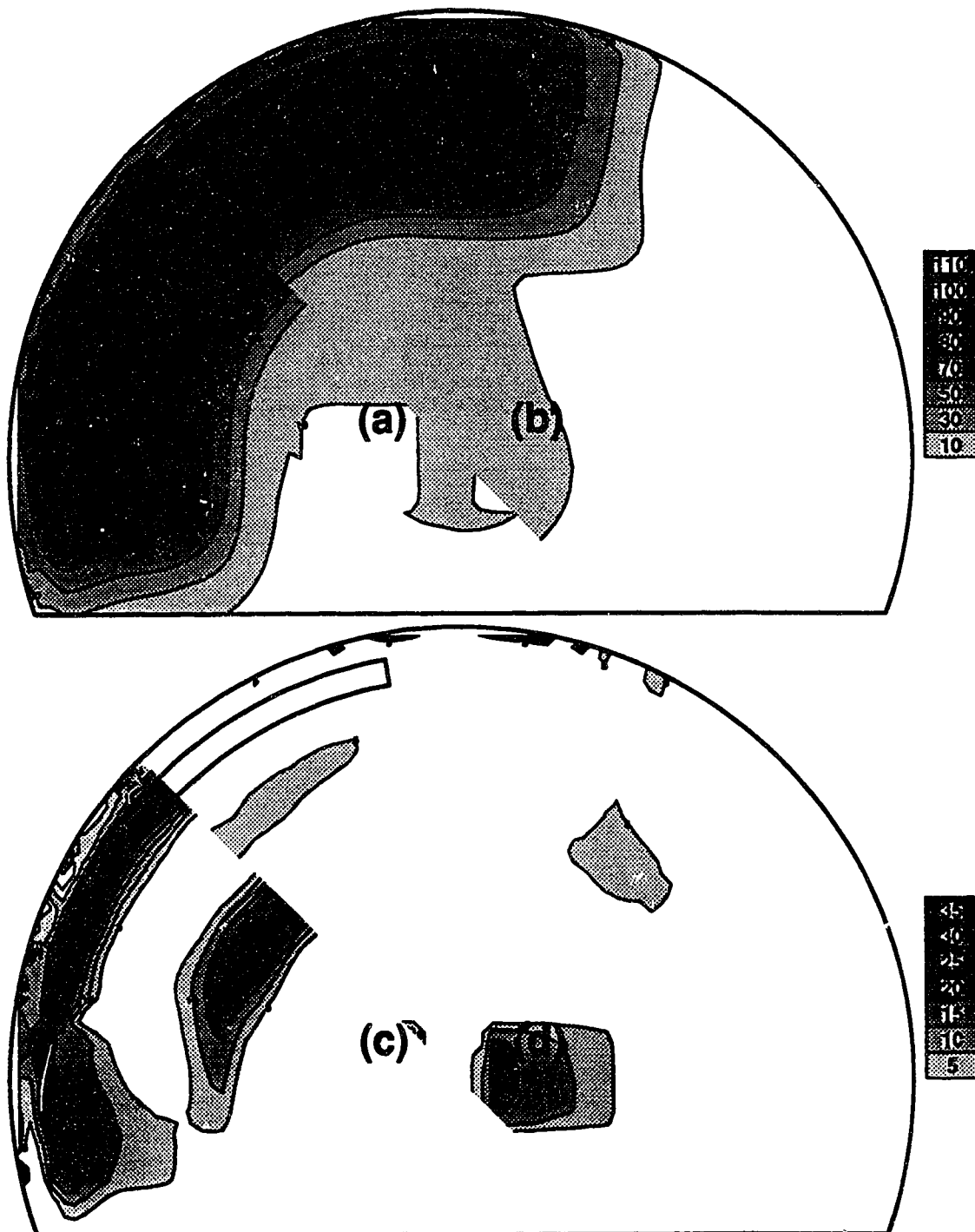


Figure 5-14 Isodose and Difference maps for an arc of 145 degrees with a 20 MeV beam incident on a phantom with an aluminum insert that follows the contour of the phantom. The position of the insert is outlined in the maps.

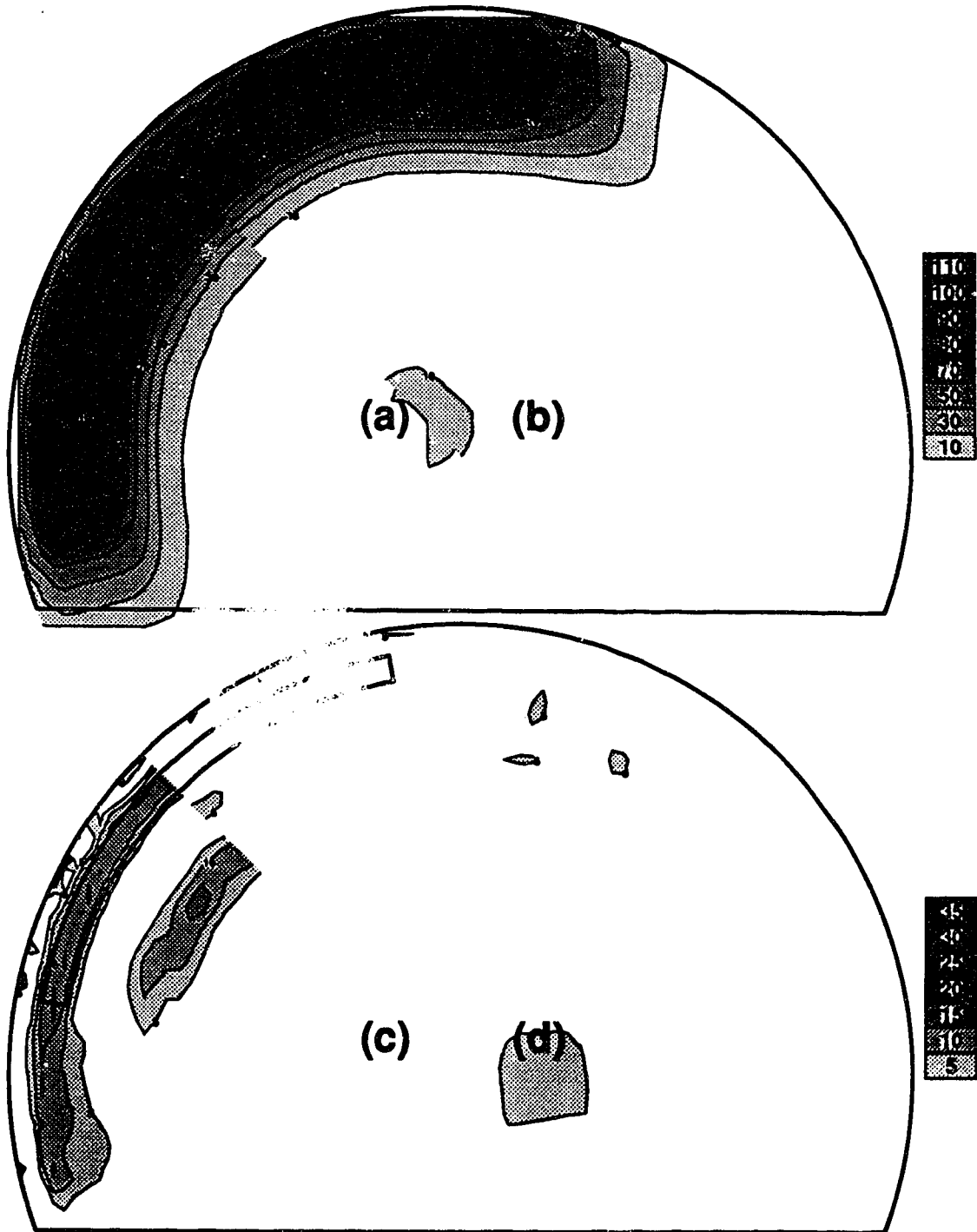


Figure 5-15 Isodose and Difference maps for an arc of 130 degrees with a 12 MeV beam incident on a phantom with a hard bone analogue insert that follows the contour of the phantom. The position of the insert is outlined in the maps.

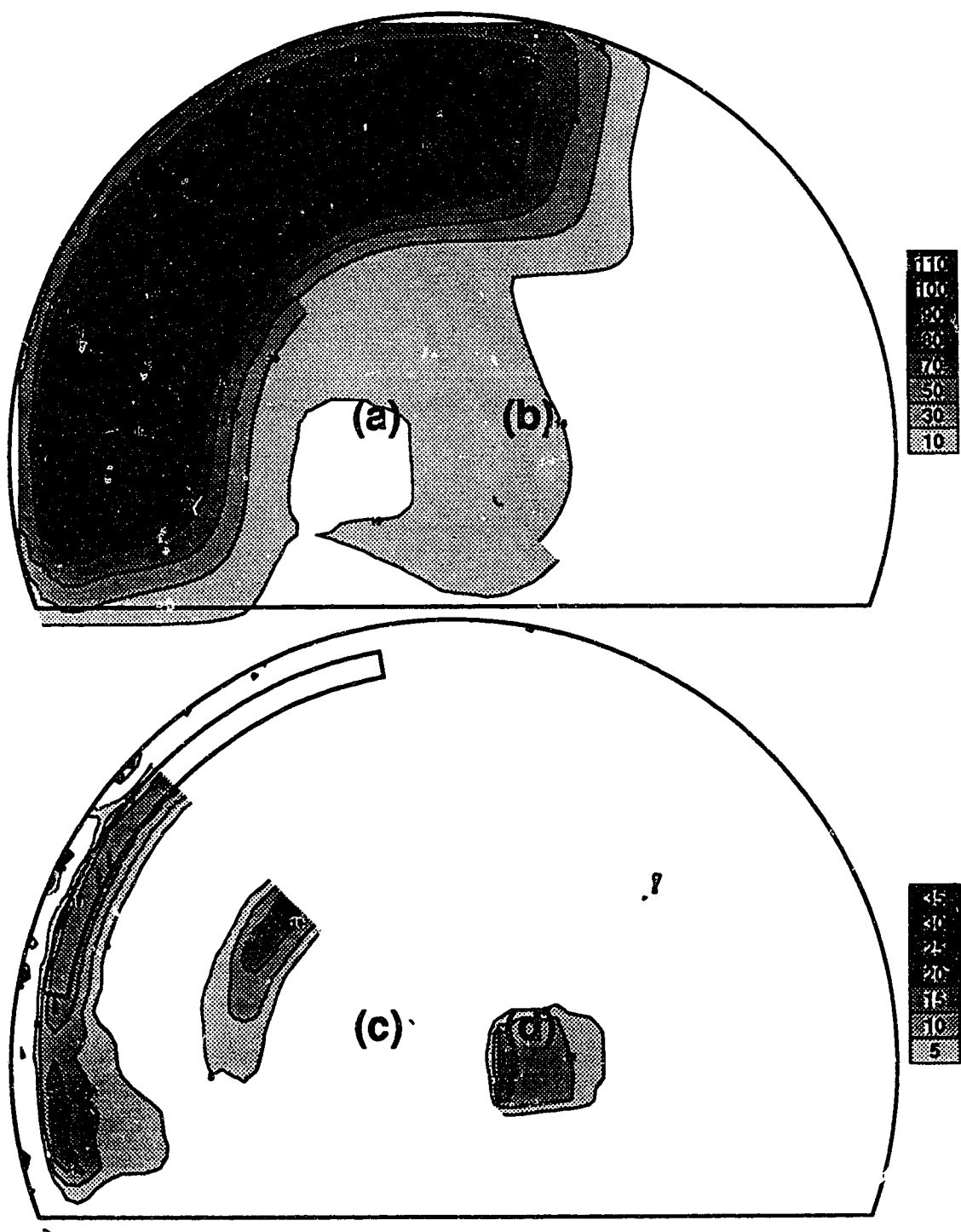


Figure 5-16 Isodose and Difference maps for an arc of 130 degrees with a 20 MeV beam incident on a phantom with a hard bone analogue insert that follows the contour of the phantom. The position of the insert is outlined in the maps.

aluminum inhomogeneity, however the differences are in general of a lower magnitude. Differences are again seen in the inhomogeneity, but they are generally about 10 %. Directly behind the inhomogeneity the calculated dose is 5 % higher for the aluminum insert, however there is only a very small region showing a 5 % difference in this area with the lower density hard bone analogue. At a larger distance from the inhomogeneity the measured dose becomes higher than the calculated dose as was observed for the aluminum. In this case the differences are only up to 15 % for both energies in this region compared to 25 % seen with the aluminum. Figures 5-17 and 5-18 show the difference maps for an arc of 130 degrees with a rib bone analogue as the high density inclusion. It can be seen that the difference maps have the same general shape as the difference maps for the aluminum and hard bone inclusions, but the differences are of a slightly lower magnitude than those observed for the hard bone analogue.

Another configuration of high density inhomogeneities was investigated in this study. In this case aluminum rods were inserted into the phantom in the direction perpendicular to the plane of rotation, as was shown in Figure 3-2. In the region with the one rod offset from all the rest the differences caused by a single small inhomogeneity can be seen. The phantom also consists of a region with four rods together with a small gap between each rod which shows how one inhomogeneity will affect another when they are separated by a small distance. This type of set up has been investigated by other authors for stationary electron beam irradiation (Cyglar J. 1989, Mah E. 1989). For this reason it was felt that this set up may produce some interesting results. Figures 5-19 and 5-20 present the dose and difference maps for this phantom configuration. In this case there is no axis of symmetry in the phantom, so the dose maps could not be overlaid

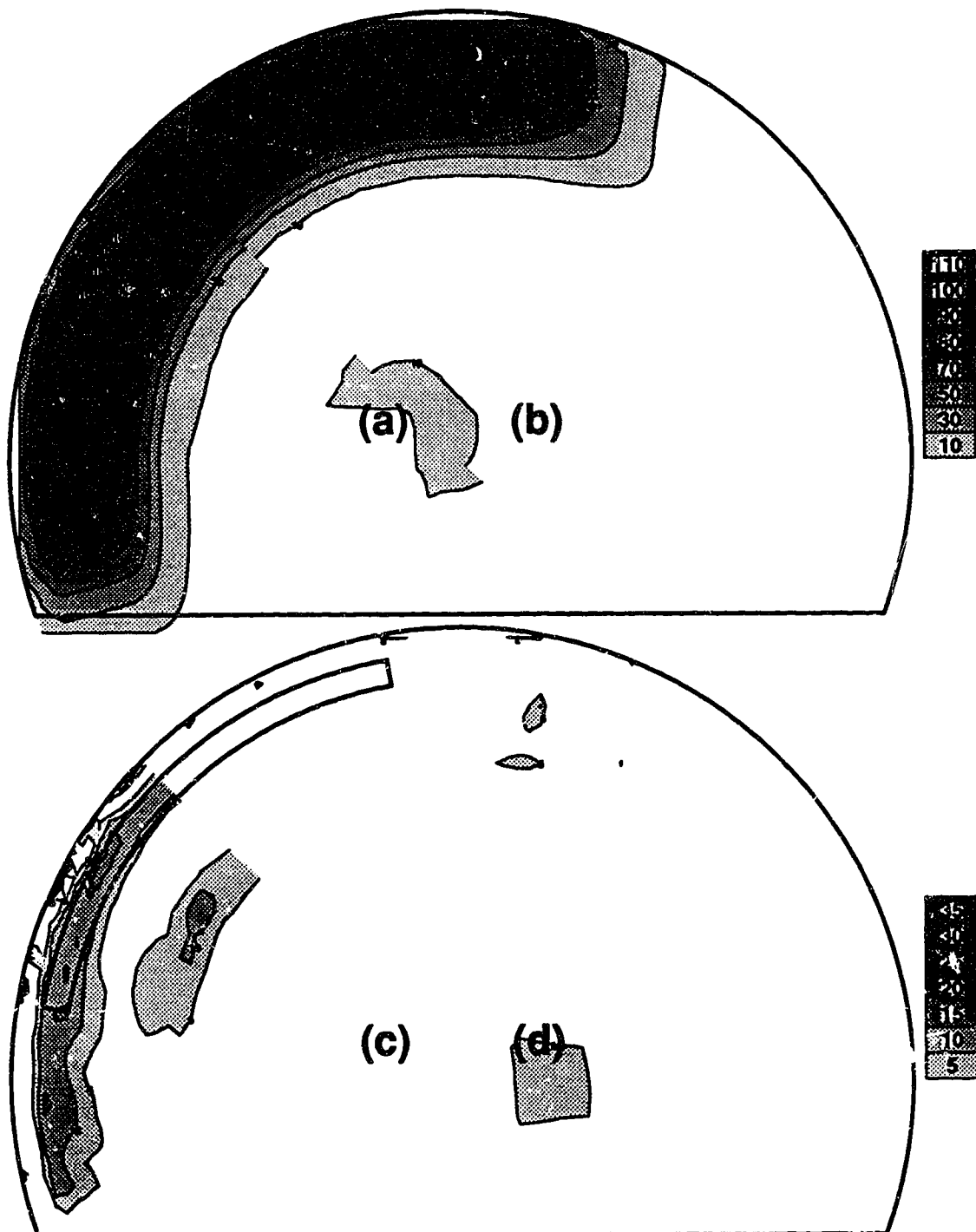


Figure 5-17 Isodose and Difference maps for an arc of 130 degrees with a 12 MeV beam incident on a phantom with a rib bone analogue insert that follows the contour of the phantom. The position of the insert is outlined in the maps.

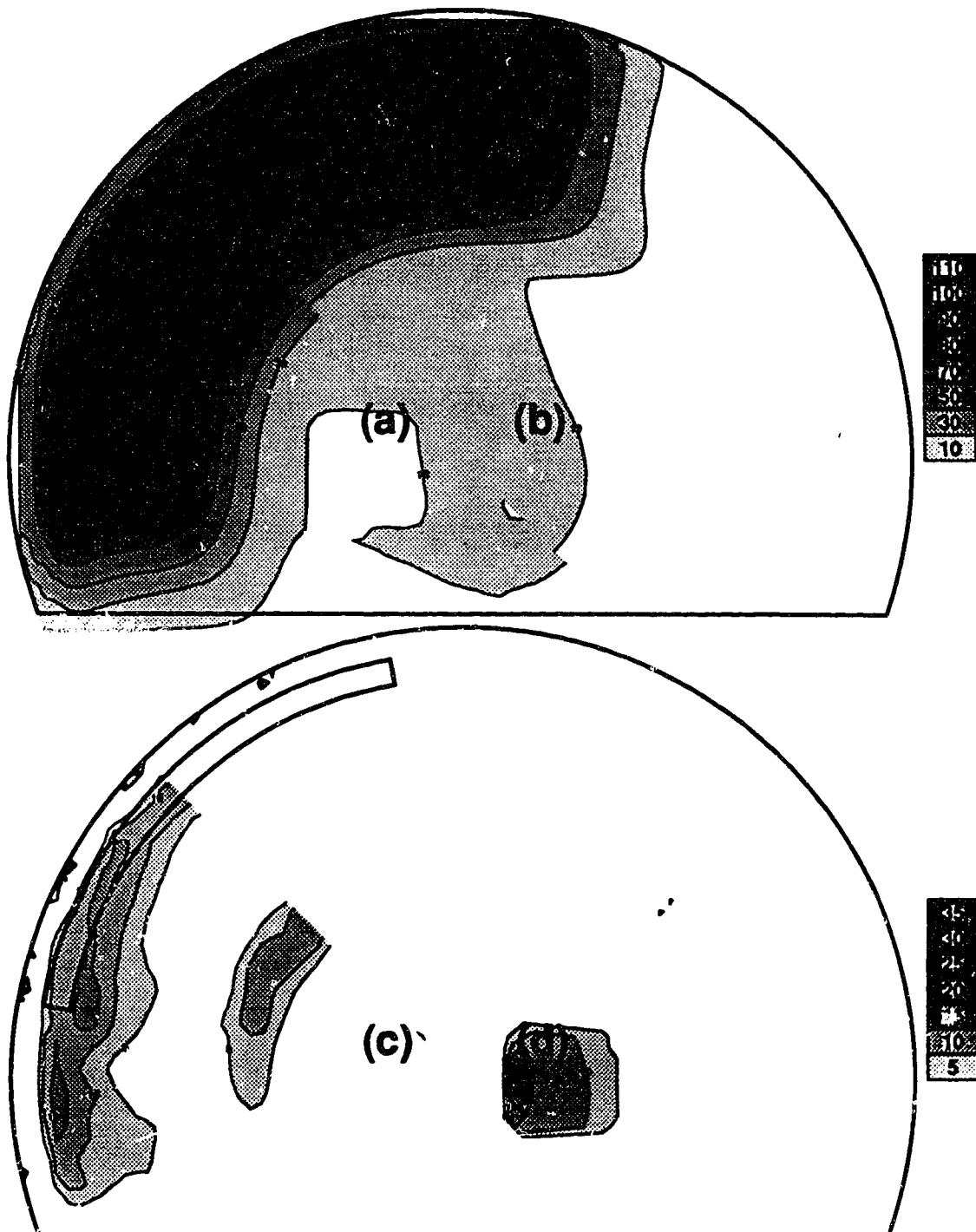


Figure 5-18 Isodose and Difference maps for an arc of 130 degrees with a 20 MeV beam incident on a phantom with a rib bone analogue insert that follows the contour of the phantom. The position of the insert is outlined in the maps.

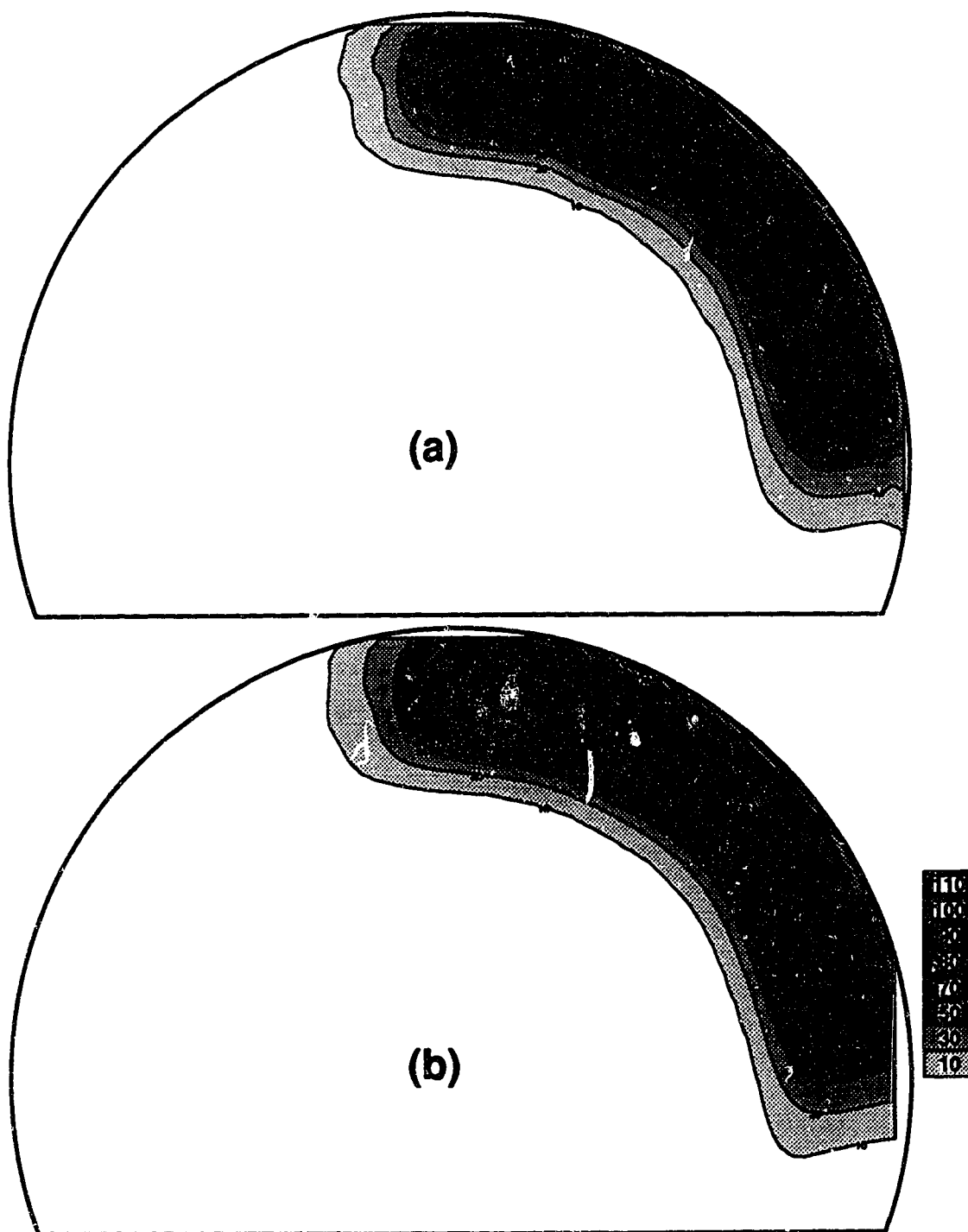


Figure 5-19 Isodose maps for an arc of 130 degrees with a 12 MeV beam incident on a phantom with a series of aluminum rods which follow the contour of the phantom. The position of the rods are outlined in the maps.

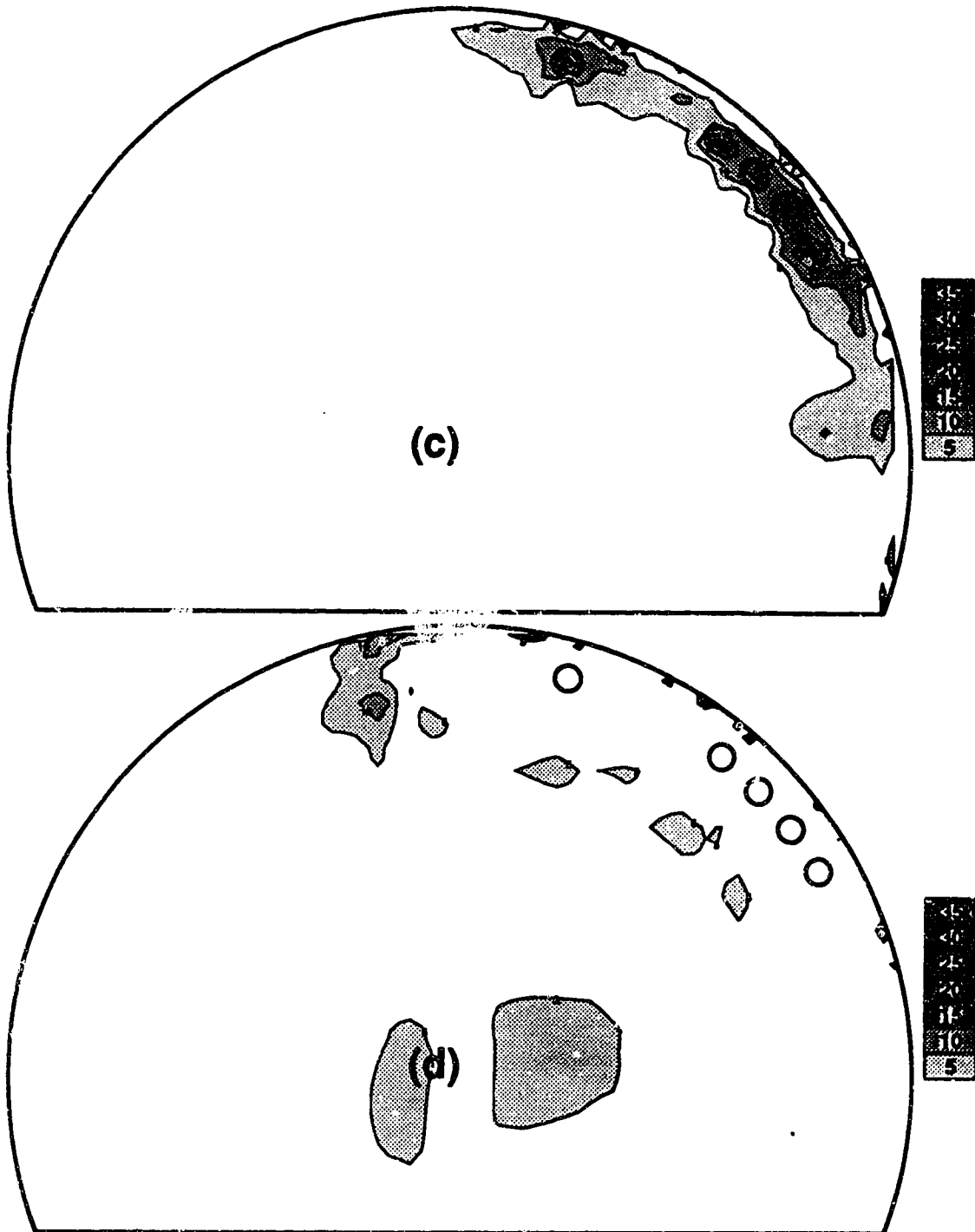


Figure 5-19 Difference maps for an arc of 130 degrees with a 12 MeV beam incident on a phantom with a series of aluminum rods which follow the contour of the phantom. The position of the rods are outlined in the maps.

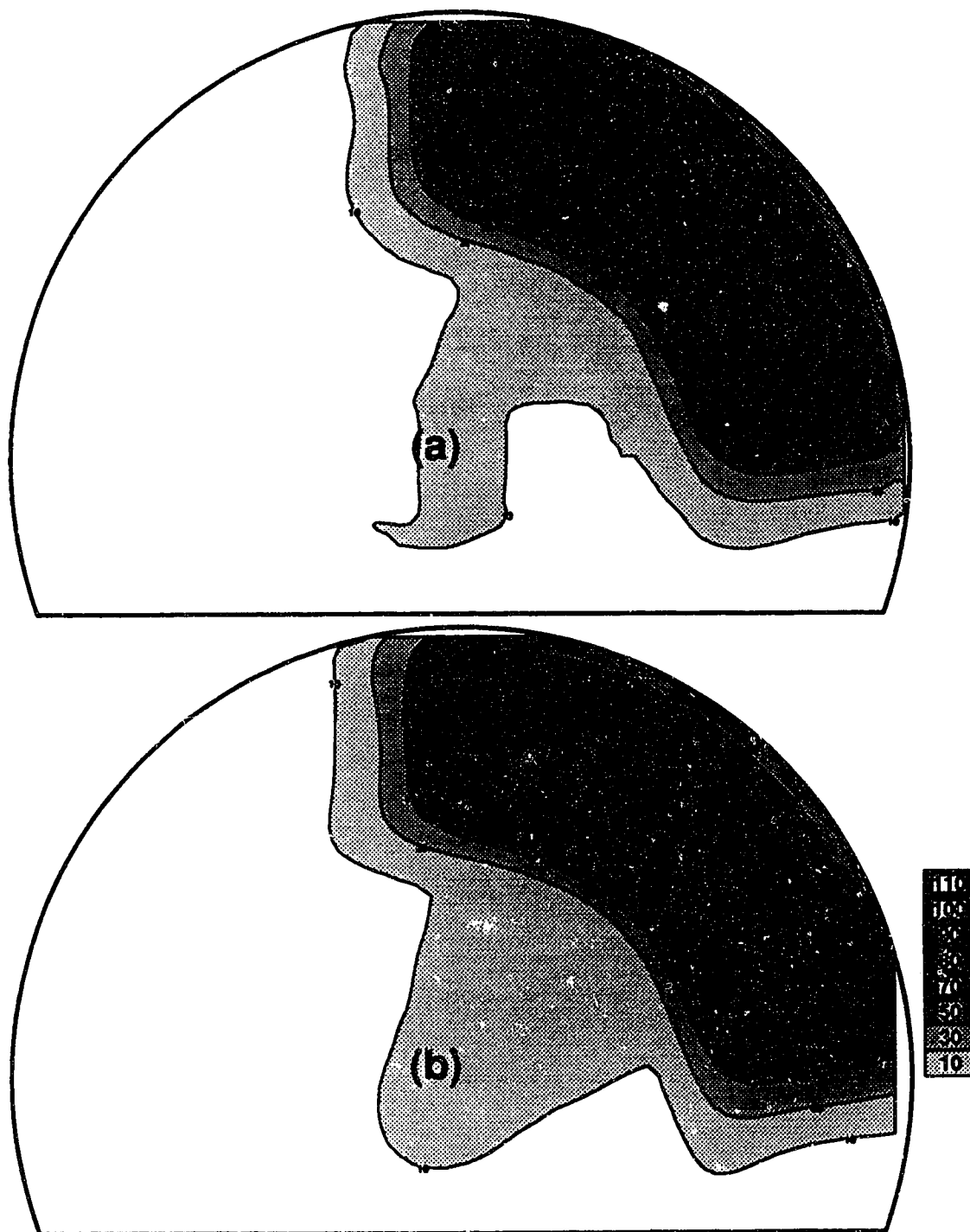


Figure 5-20 Isodose maps for an arc of 130 degrees with a 20 MeV beam incident on a phantom with a series of aluminum rods which follow the contour of the phantom. The position of the rods are outlined in the maps.

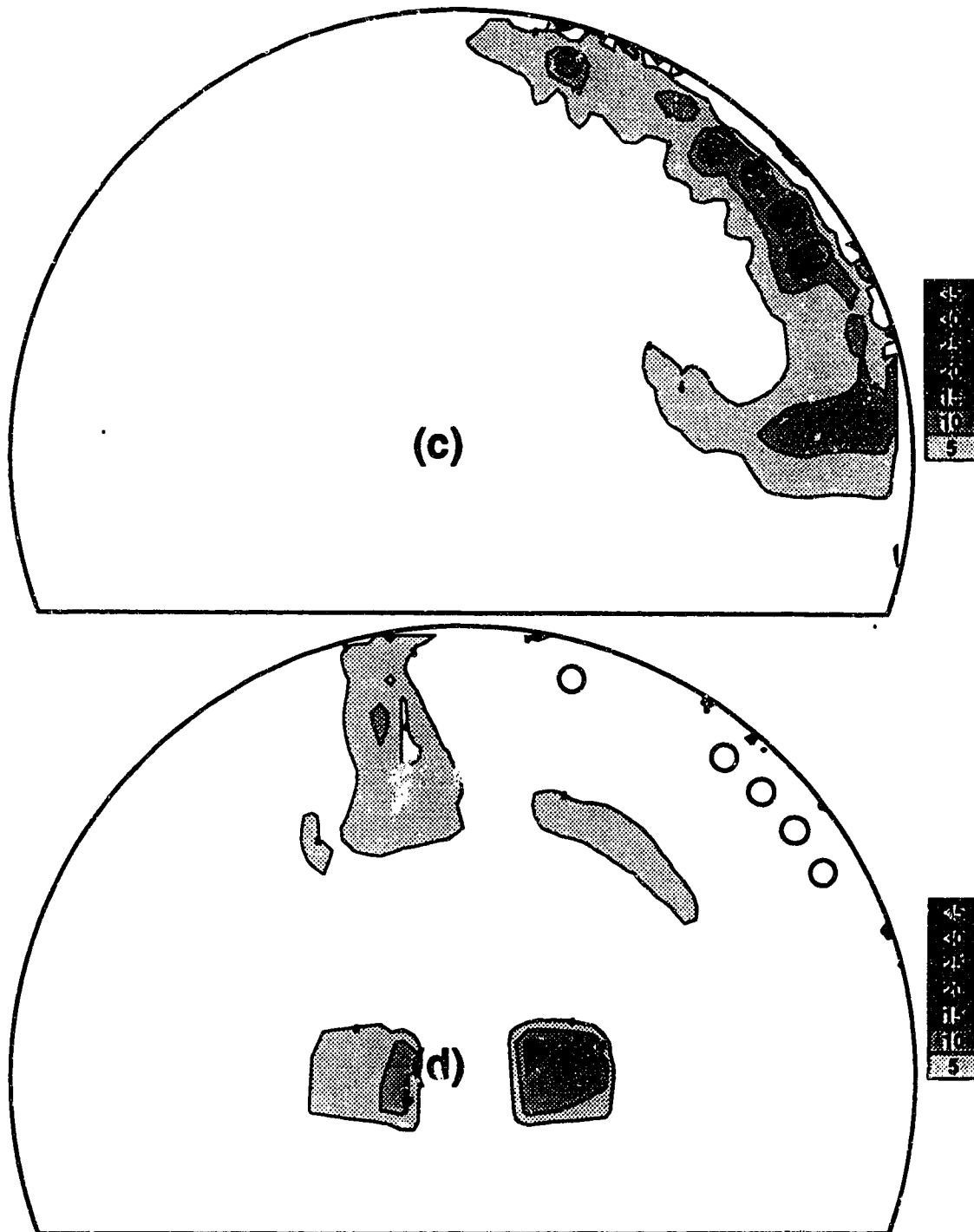


Figure 5-20 Difference maps for an arc of 130 degrees with a 20 MeV beam incident on a phantom with a series of aluminum rods which follow the contour of the phantom. The position of the rods are outlined in the maps.

as they have been in the previous figures. The notation, however, has remained the same with figure (a) showing the measured dose matrix, (b) is the calculated dose matrix; regions where the measured dose is greater than the calculated dose are shown in (c), and (d) shows where the calculated dose is greater than the measured dose. This data presents some very interesting results. The dose maps reveal that with the single inhomogeneity there is a very narrow region directly behind the rod that receives a substantially lower dose than the surrounding region. However, when there are a series of rods all in close proximity these narrow region tends to get spread out and the cold spot directly behind the inhomogeneity is not as cold as in the case of the single rod. From this we can see the progression from the small single inhomogeneity to the series of inhomogeneities to the solid bar that has been discussed previously. Similar to the aluminum bar configuration there are large differences in measured and calculated dose inside the inhomogeneity. There is a difference of 5 % in the build up region as was seen for the homogeneous phantom. There are also small areas directly behind the inhomogeneities where the calculated dose is 5 % higher than the measured dose. The one major difference between what is seen in this case as compared to the aluminum bar which follows the phantom contour is that there is no area beyond the inhomogeneities where the measured dose is much higher than the calculated dose.

5.3.2 DISCUSSION

In all of the cases described above the area inside the inhomogeneity has had a much higher measured dose than the calculated value. The reason for this discrepancy lies in both the calculation algorithm and the interpretation of the film. The measured relative optical density of the film inside the inhomogeneity

must be corrected by the ratio of the mean mass collision stopping powers for polystyrene and aluminum in order to get the true dose. As was pointed out in Chapter 2 the normalized dose in the homogeneous phantom will be equal to the ratio of optical densities as measured on the film. However, when the normalization is carried out by dividing the dose to the aluminum by the dose to polystyrene the ratio of stopping powers must be evaluated. This correction can be made by estimating the energy of the electron beam at the depth of the inhomogeneity and correcting by the ratio of mean mass collision stopping powers for this energy.

$$\frac{D_{Al}}{D_{Poly}} = \frac{OD_{Al}}{OD_{Poly}} (Sp)_{Poly}^{Al} \quad \text{eq 5-1}$$

Where D_{Al} = absorbed dose within the aluminum

D_{poly} = reference dose within polystyrene

OD_{Al} = optical density of the film inside the aluminum

OD_{poly} = optical density of the film in the polystyrene

For a nominal energy of 12 MeV, the actual incident energy E_0 is 11.47 MeV. At a depth of 2.0 cm the electron beam energy is 7.63 MeV. At this energy the ratio of stopping powers for aluminum and polystyrene is 0.85 (ICRU 37), and for the 20 MeV beam this ratio is approximately the same (ie the ratio is relatively energy independent). This value will get closer to unity for the bone analogue materials. This indicates that the dose to the aluminum is about 85%

of that measured as the relative optical density. This correction can be applied to all the points in the dose matrix that lie within the inhomogeneity. The dose distributions and the difference maps with the stopping power correction applied to the measured data for the case of the aluminum bar that follows the contour of the phantom are shown in Figures 5-21 and 5-22. As is expected the difference maps simply show that the difference between the calculated and measured distributions is about 10 % inside the inhomogeneity rather than the 25 % that was apparent in Figures 5-13 and 5-14. The dose to the inhomogeneity, as predicted by the algorithm, is also suspect because it actually calculates the dose to a small volume of water inside the inhomogeneity. This will also lead to differences between the predicted dose and the actual dose. The table of stopping and scattering powers as a function of CT numbers also had to be changed in the algorithm in order to extend the values up to the CT number of aluminum. The authors of the algorithm only extended this table to CT numbers of approximately 1000 Hounsfield units, which is within the clinical range, but the CT number of aluminum is about 2250 Hounsfield units. Where the CT number is defined to be

$$H = 1000 (\mu_{mat} / \mu_{water} - 1) \quad \text{eq 5-2}$$

where μ_{mat} and μ_{water} are the linear attenuation coefficients for the material and for water.

The differences found at a large depth beyond the inhomogeneity for the case of the bar following the phantom contour may be caused by assumptions made in the algorithm. The bar is only 12 mm wide in the direction perpendicular to the plane of rotation, but the algorithm assumed it to be infinite in this direction (2D inhomogeneity correction). This assumption could produce the differences

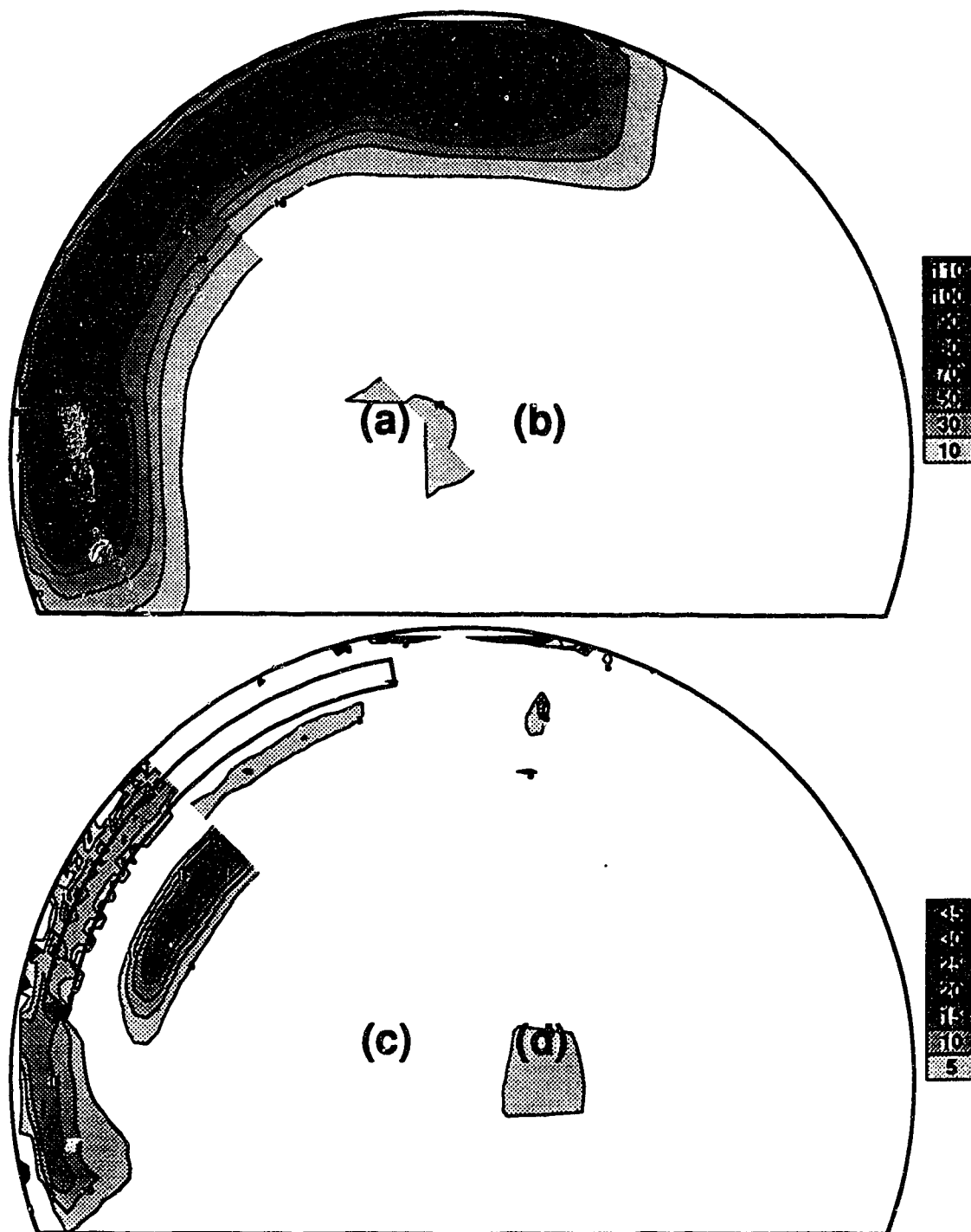


Figure 5-21 Isodose and Difference maps for an arc of 130 degrees with a 12 MeV beam incident on a phantom with an aluminum insert that follows the contour of the phantom. The position of the insert is outlined in the maps. The measured dose matrix has been corrected by the ratio of stopping powers inside the inhomogeneity.

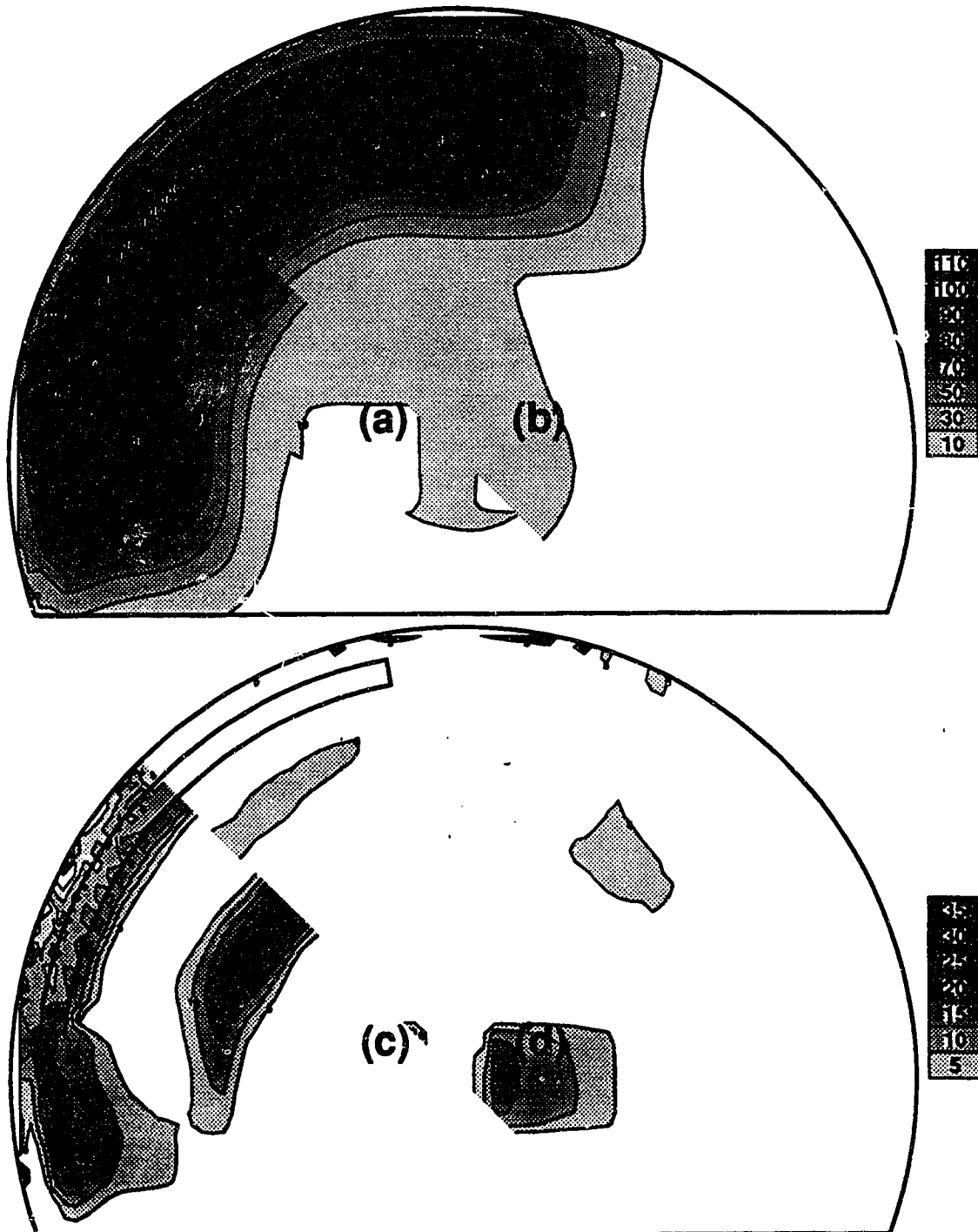


Figure 5-22 Isodose and Difference maps for an arc of 130 degrees with a 20 MeV beam incident on a phantom with an aluminum insert that follows the contour of the phantom. The position of the insert is outlined in the maps. The measured dose matrix has been corrected by the ratio of stopping powers inside the inhomogeneity.

that are being seen between the measured and calculated dose distributions beyond the inhomogeneity. The algorithm's assumption that the inhomogeneity is infinite will cause the calculated dose to be higher directly beyond the inhomogeneity because the scattering power for aluminum is higher than that for polystyrene. Therefore, the algorithm will predict more scatter from the adjacent planes of the phantom than that which is actually present in the experiment. This could cause the differences seen between the measured and predicted dose maps directly behind the bar that follows the contour of the phantom. Then at a larger depth the opposite type of effect will occur because of this assumption. In the experiment there will be a large number of electrons that have passed through polystyrene, but are scattered into the measurement plane. The calculation will only have electrons which have passed through the 1 cm of aluminum reaching this depth, and they will therefore, be of a lower energy than those in the experiment. This will mean that the measured dose will be higher than the calculated dose at a depth beyond a two dimensional inhomogeneity, which is what we have observed. The data also shows that the magnitude of this difference decreases as the density of the inhomogeneity approaches unity. This is what would be expected if the differences were caused by the two dimensional inhomogeneity correction. This would happen because as the inhomogeneity approaches unity the difference between electrons passing through the inhomogeneity or the polystyrene would become minimal. If the 2-D inhomogeneity correction is the cause of these differences they should not appear in the case of the aluminum rods that are perpendicular to the plane of rotation, since they fulfil the 2-D requirement of being effectively infinite in extent. This is in fact the case, as is borne out in Figures 5-19 and 5-20. The differences

found in the phantoms with high density inhomogeneities can, therefore, be attributed to the 2-D limitation of the algorithm. The small differences in the build up region were also present in the homogeneous phantom.

5.4 LOW DENSITY INHOMOGENEITIES

5.4.1 RESULTS

Low density inclusions in the phantom, can also reveal substantial differences between the measured and calculated dose distributions. Figures 5-23 and 5-24 show the isodose distributions and difference maps for an arc of 140 degrees incident on the phantom with a cork insert, which was illustrated in Figure 3-2. Figure 5-23 is for a 12 MeV electron beam, and Figure 5-24 is for a 20 MeV beam. For both energies similar results are observed. From the shape of the isodose curves it is apparent that the inhomogeneity is causing very different things to happen in the measured and calculated dose matrices. This is most obvious in Figure 5-23 (a) and (b) (12 MeV arc) by looking at the shape of the 10% isodose line as it approaches the inhomogeneity. The isodose line is perturbed at a greater distance from the inhomogeneity in the calculated distribution than it is in the measured distribution. The difference maps show differences both within and outside the inhomogeneity. In the central area of the arc there is a 15 % difference between the measured and calculated doses near the surface. Within the inhomogeneity there are differences of 10% with the calculated dose being greater than the measured dose. The algorithm predicts a significant amount of scatter out of the cork that is not seen in the measured distributions, thus the area near the edge of the cork shows the calculated dose to be higher than the measured dose. For a 20 MeV beam this difference is as

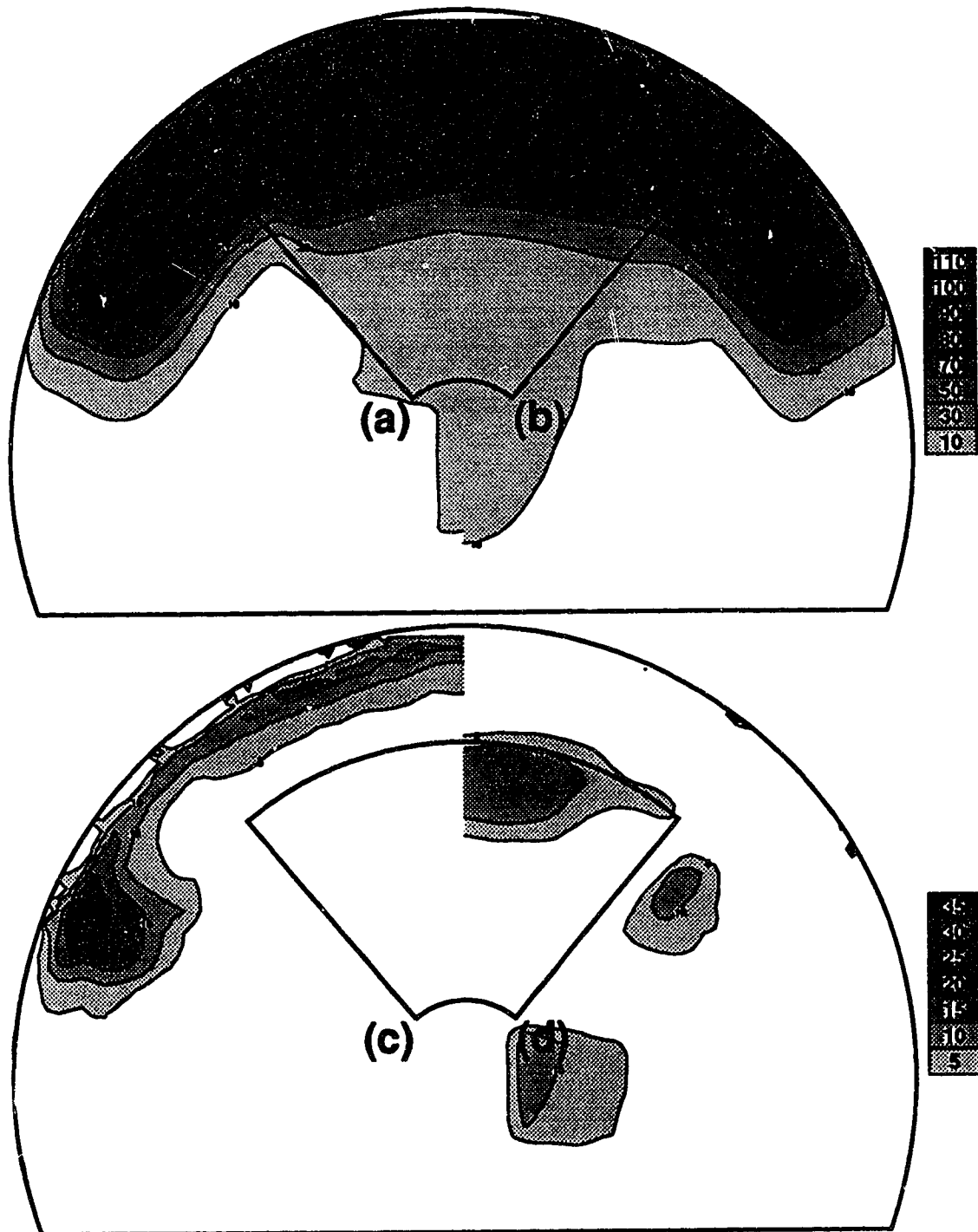


Figure 5-23 Isodose and Difference maps for an arc of 140 degrees with a 12 MeV beam incident on a phantom with a cork insert that follows the contour of the phantom. The position of the insert is outlined in the maps.

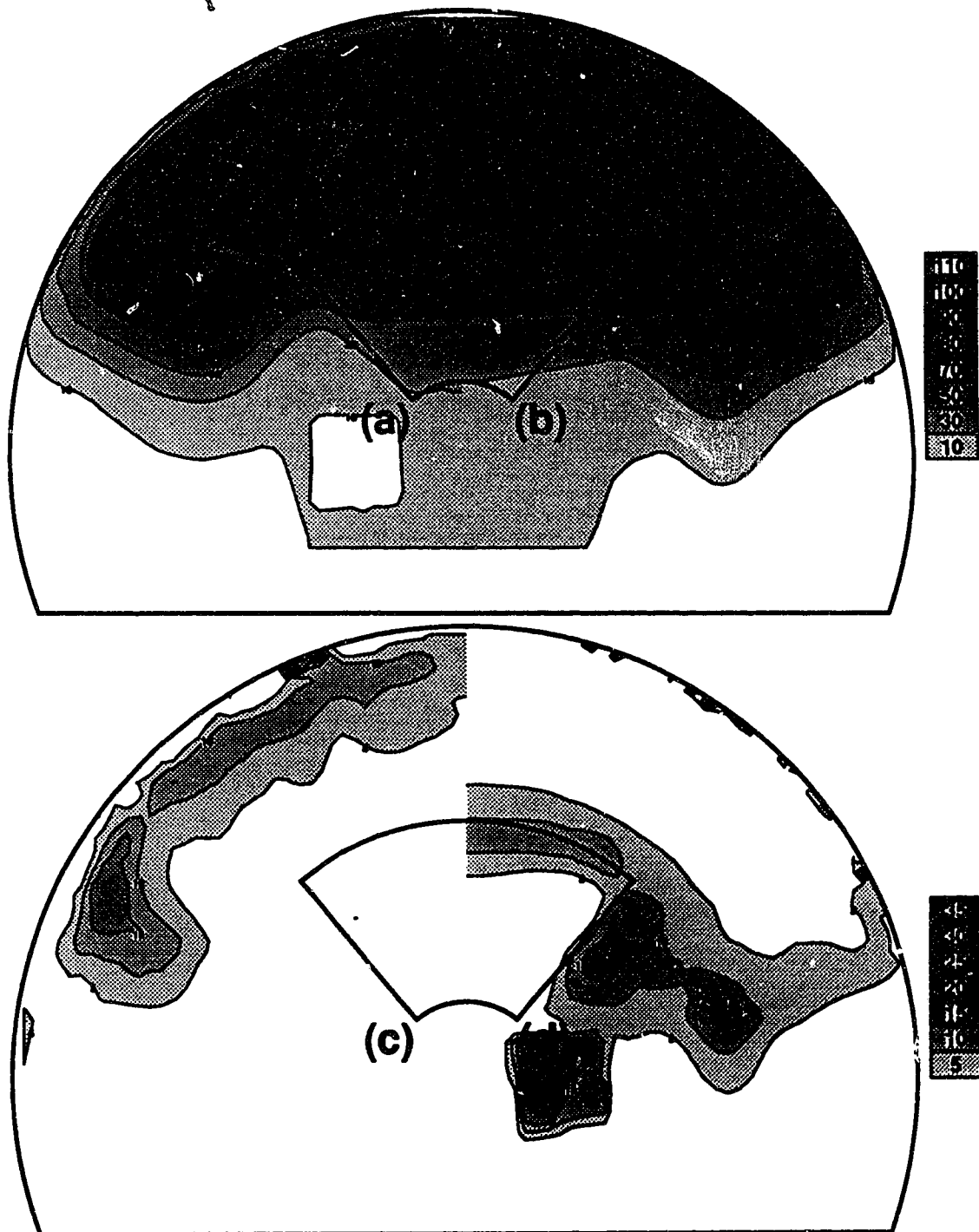


Figure 5-24 Isodose and Difference maps for an arc of 140 degrees with a 20 MeV beam incident on a phantom with a cork insert that follows the contour of the phantom. The position of the insert is outlined in the maps.

high as 15 % and for the 12 MeV beam it is 10 %.

Another phantom configuration was made such that the area in which the high density inclusions representing the rib bone was left as an air gap. This situation may be clinically relevant since it is possible to have small air gaps inside the patient. This situation will also stress the algorithm because the gap is three dimensional, and the algorithm assumes it to be two dimensional. In this case the inhomogeneity is only 12 mm in this direction, and therefore, should test the limits of the algorithm. Figures 5-25 and 5-26 show the dose and difference maps for the 12 and 20 MeV beams respectively. Again an arc of 130 degrees was used. As would be expected the depth of d_{\max} is shifted deeper when the low density inhomogeneity is present. However, the algorithm predicts d_{\max} to be substantially deeper than the depth of d_{\max} in the measured data. This occurs for both the 12 and 20 MeV beams. This causes the fall off region to be substantially deeper for the calculated dose distribution, causing a very large difference between the measured and calculated dose distributions at depth. These differences reach 25% for the 12 and the 20 MeV arcs. As was the case for the cork insert, and the homogeneous phantom there are also differences between the measured and calculated dose distributions in the build up region.

5.4.2 DISCUSSION

The phantom with the cork insert which simulates the lung illustrates some interesting results. In this case the inhomogeneity is of sufficient width to provide full scatter. Therefore, the 2-D inhomogeneity assumption should be a valid assumption, and we would not expect to see any effects due to it. As was described in the results section, the experimental and computed isodose lines have a very different shape as they enter or approach the inhomogeneity,

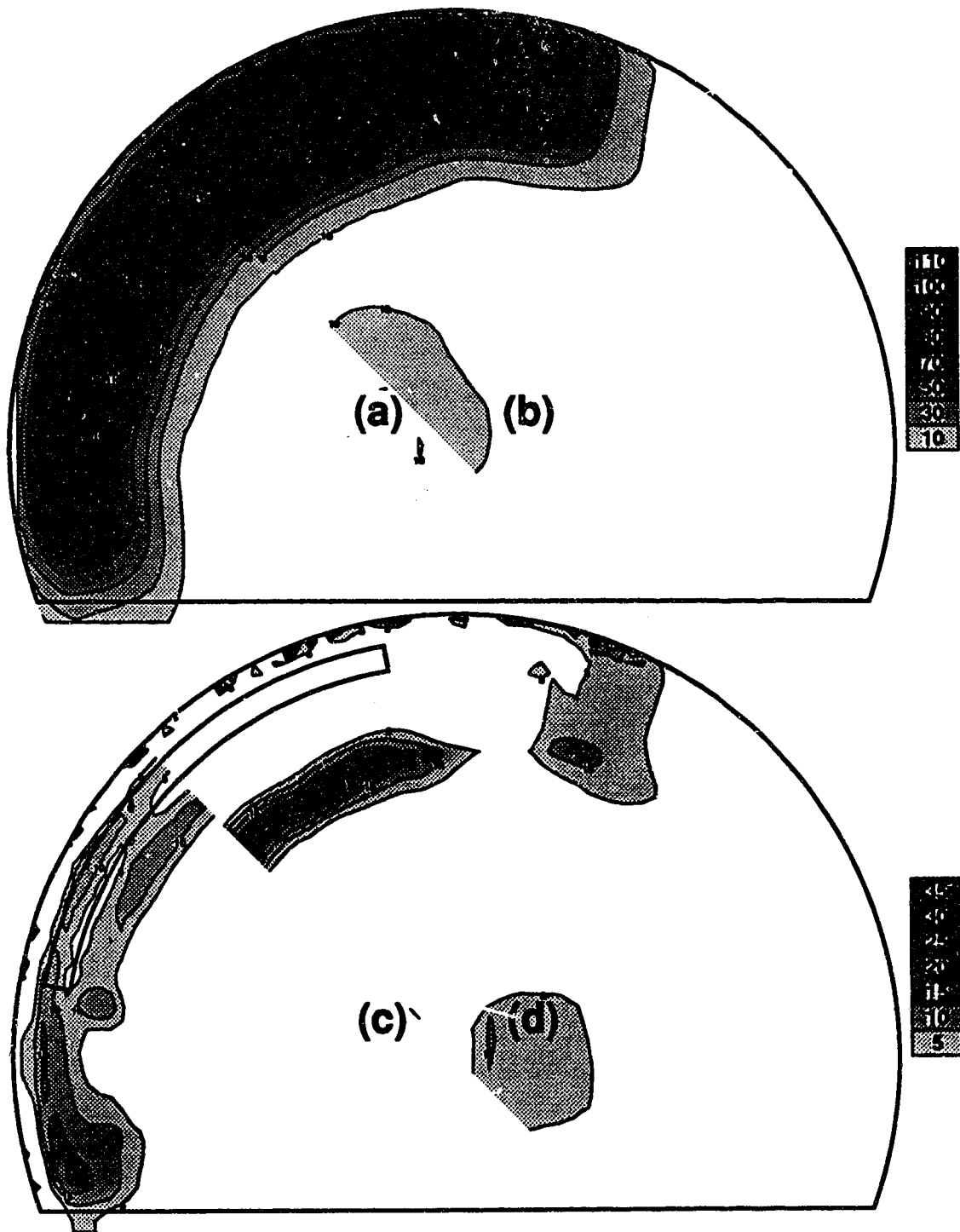


Figure 5-25 Isodose and Difference maps for an arc of 130 degrees with a 12 MeV beam incident on a phantom with an air gap that follows the contour of the phantom. The position of the air gap is outlined in the maps.

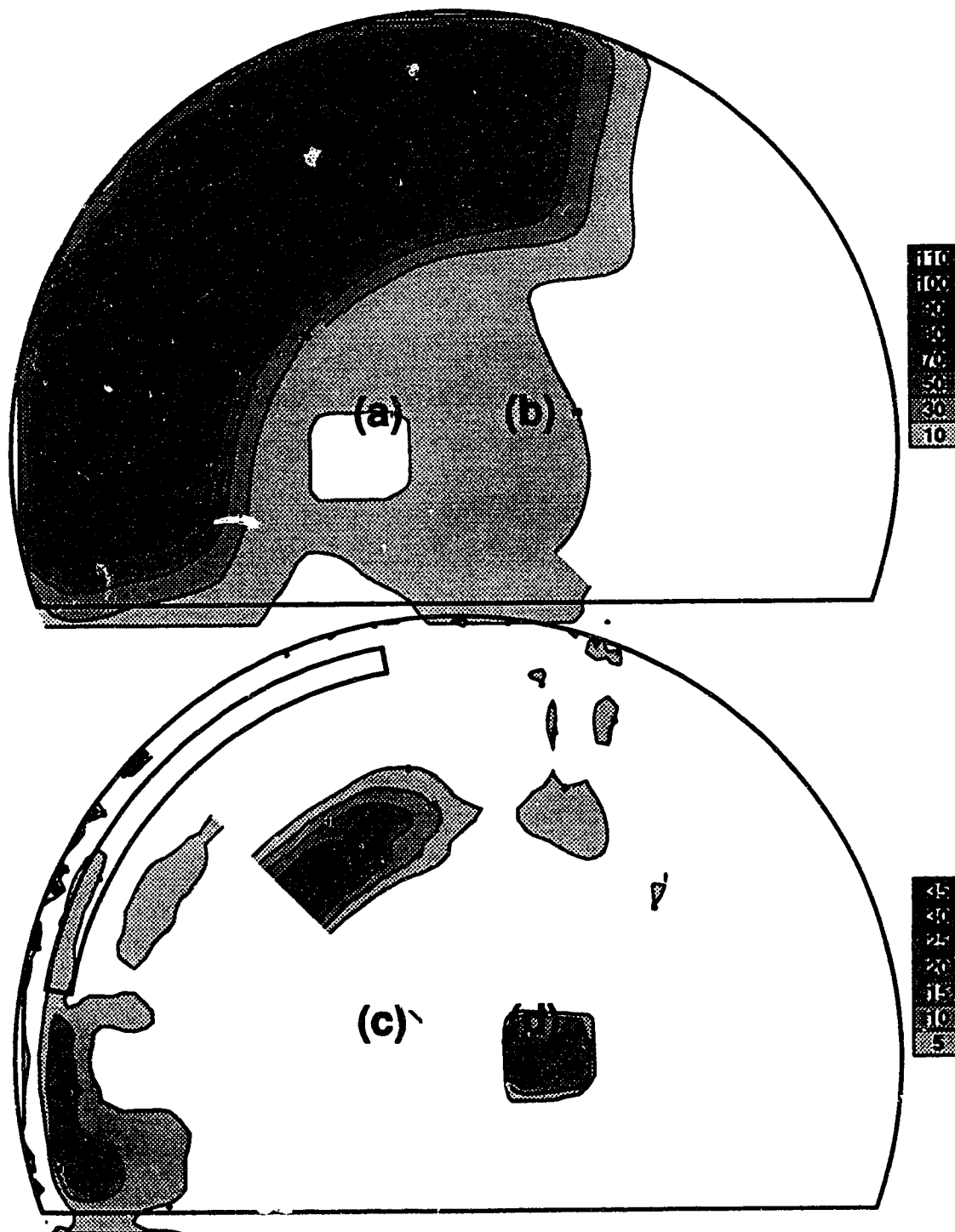


Figure 5-26 Isodose and Difference maps for an arc of 130 degrees with a 20 MeV beam incident on a phantom with an air gap that follows the contour of the phantom. The position of the air gap is outlined in the maps.

suggesting that the algorithm is predicting more scatter out from the edge of the cork than that which is measured. This would cause the isodose lines to be perturbed at a distance further from the inhomogeneity than they should be, and this is in fact what is observed. This would explain the very large difference that is seen near the edge of the cork insert, where the calculated dose can be up to 15 % higher than the measured dose. In describing the differences for the arc irradiations on the homogeneous phantom we found only small regions of 5 % difference. However, when these difference maps are compared with those for the phantom with the cork insert it is obvious that the differences are occurring at the same depth. With the cork phantom however, these differences are amplified as they enter the low density inhomogeneity. Therefore, it appears that the errors inside the cork are due mainly to the slight differences that were apparent in the homogeneous case.

In the case of the of the air gap the 2-D inhomogeneity assumption will obviously be violated, as it was for the high density inclusions with the same set up. If the differences are caused by this assumption they would be expected to be opposite to those that were found for the high density inclusions. Since the electrons coming through the lateral planes would be propagated through an extra centimeter of air in which they would lose very little energy. When these electrons are scattered into the plane of calculation they would have more energy to deposit than the electron that actually passed through polystyrene in the off axis plane rather than air. This would cause the calculated dose to be higher than the measured dose distant from the inhomogeneity. This is in fact what is observed. The measured dose directly behind the inhomogeneity would be expected to be higher than the calculated dose because the scattering power of

air is less than that of polystyrene. Thus more electrons are scattered in from adjacent planes than are predicted by the algorithm, thus causing the measured dose to be higher than the calculated dose in this region.

The differences found in the case of the phantom with the cork insert can, therefore, be attributed to the small differences found in the homogeneous arc irradiation. The differences in the dose distributions for the arc on the phantom with the air gap seen to be due to the assumption in the algorithm that the inhomogeneity is infinite in extent.

5.5 SUMMARY OF THE EFFECTS OF THE INHOMOGENEITIES

Figure 5-27 illustrates how the inhomogeneities perturb the homogeneous PDDs for both 12 and 20 MeV beams. They show that the depth doses are changed substantially by the inhomogeneities. The dose is higher inside the high density inhomogeneity, which lies between one and two centimeters in depth, than it is for the homogeneous case. As the density of the inhomogeneity approaches unity the PDD is perturbed to a lesser degree, as is expected. Beyond the inhomogeneity the dose drops rapidly but then it has a slight increase. The increase is more apparent for the 20 MeV beam than for the 12 MeV. This type of depth dose has been observed for stationary beams behind a high density inhomogeneity. It is possible that the increase in dose at a depth beyond the inhomogeneity is due to the increased scatter contribution from the high density inhomogeneity. The low density inhomogeneity also perturbs the PDD. The cork extends from a depth of 4.5 to a depth of 14 cm for the 12 MeV and from 7.5 -14 cm for the 20 MeV beam. The PDD follows the PDD in the homogeneous phantom until it reaches the inhomogeneity. The inhomogeneity causes the fall off region beyond d_{max} to broaden compared to the

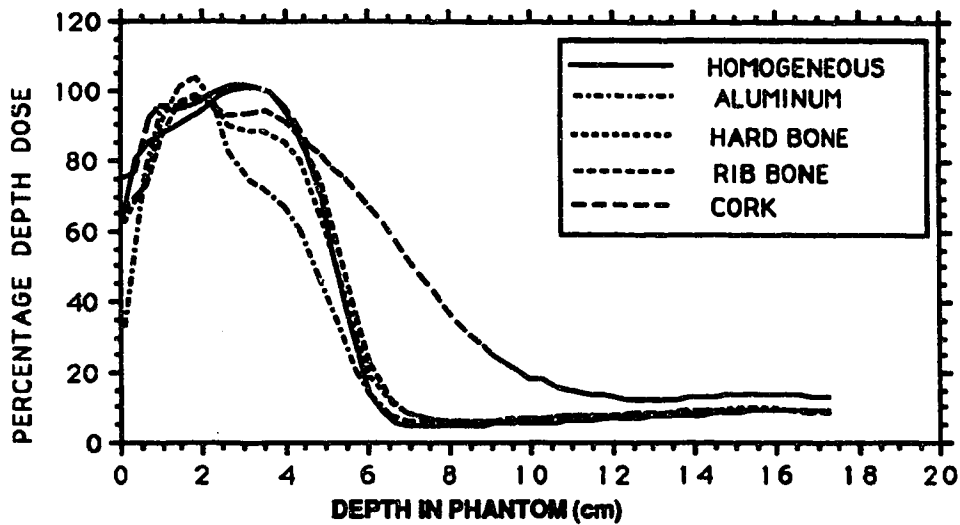


Figure 5-27(a) Percentage depth dose through various inhomogeneities for an arced 12 MeV electron beam. The aluminum, hard bone and rib bone are positioned from 1-2 cm depth, while the cork is from 4.5 -13 cm in depth.

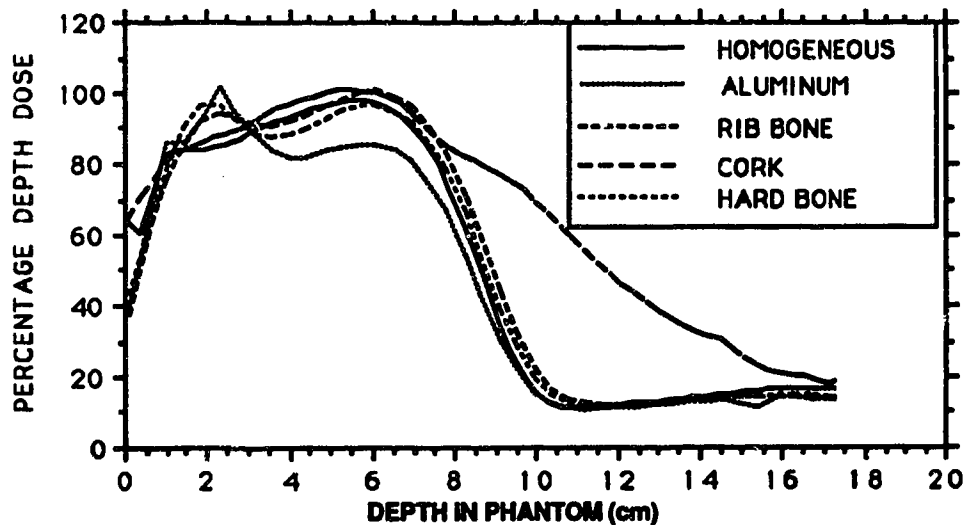


Figure 5-27(b) Percentage depth dose through various inhomogeneities for an arced 20 MeV electron beam. The aluminum, hard bone and rib bone are positioned from 1-2 cm depth, while the cork is from 7.5 -13 cm in depth.

homogeneous arc. This is expected, since the range of the electrons will be much larger in the cork than it is in polystyrene.

CHAPTER 6 PLANNING AN ELECTRON ARC TREATMENT

The methodology behind planning an electron arc treatment is very complex, and takes a long time compared to the time required for other types of radiation treatment. For this reason the treatment planning technique should be as streamlined as possible or the treatment will not be used to its fullest extent. The following will be an overview of the complete process that must be followed in order to plan an electron arc treatment.

The first component of the treatment planning process is to determine the position of the tumor within the patient and the position of all the critical structures such as the spinal cord and the lungs etc.. This can normally be done using either a CT scanner or a simulator. It is the responsibility of the physician to determine the position of these structures. The CT scans should be taken in multiple slices to get a good three dimensional view of the treatment area. The contour of the patient should also be manually measured in the same planes as the CT slices, as this information is required for the calculation algorithm. The contours can generally be taken directly from the CT information, but in some cases the patient cannot be scanned in the same position as that in which he / she would be in for treatment. In these cases the CT contours may be slightly distorted, and manual measurements should be used. The next step is to pass this information on to the calculation algorithm where the treatment process is determined. If the contour of the patient is curved, and the tumor is fairly large and follows the contour of the patient, electron arc therapy would be a good method to treat the patient. If electron arc treatments are proposed the following factors must be determined before treatment can begin:

1) The energy of the beam must be determined to give a sufficiently high dose to the tumor while sparing the surrounding healthy tissue as much as possible.

2) The position of the isocenter must be determined. This is a vital step since the dose at isocenter can be very high due to the photon contamination in the beam. Therefore, the isocenter cannot be positioned close to any vital organs. It is also important that the isocenter be chosen such that the distance from the isocenter to the patient surface is constant so that the SSD does not change over the length of the arc. By doing this the isodose lines will follow the contour of the patient, thus giving a uniform dose at any given depth.

3) The dose distribution must be calculated. This is usually an iterative process, where many different parameters are modified and the distribution is recalculated until an acceptable dose distribution is found. Once an acceptable distribution has been found in the central plane, the distribution must also be checked in the off axis planes. This may require modification of some of the parameters that can affect the off axis dose distribution. The arc may be broken into two or more segments, each varying all the possible parameters, then the dose from each segment must be added in order to get the complete dose distribution. Therefore, this can be an extremely time consuming process. The following parameters can be modified in order to produce the best possible dose distribution.

i) The extent of the arc should be determined in order to treat the entire tumor volume.

ii) The dose per degree setting for each segment of the arc must be determined if the weighting of the segments is to be different.

iii) The secondary collimator, which defines the field size, must be designed for each individual patient. One of the primary methods of changing the dose distributions in the off axis planes is by designing the secondary collimator with a different field size at the extremities than at the central axis.

iv) Bolus, which adds tissue equivalent material to the patient surface in order to increase the effective depth of the tumor, is often used. In these cases it should be designed to optimize the treatment plan.

v) The position of the isocenter can be optimized, which may mean rotating the patient slightly such that the isocentric axis does not follow the patient axis.

vi) The patient collimator must be designed such that as much normal tissue is spared without interfering with the dose deposition in the tumor. This step is tied primarily to the design of the secondary collimator. The patient collimator should be at the position in the penumbra where the dose has fallen to approximately 90% of the central axis dose. It can also be shaped to shield radiation sensitive tissue in the irradiated volume:

vii) The absolute dose must be calculated for the distribution that has been proposed, which determines the monitor unit settings for the accelerator for each treatment.

The planning process can take as much as 4-5 hours and a faster algorithm for performing the calculations can streamline the planning process. The actual calculation time is about 4-5 minutes of processor time for an arc of about 140 degrees, or longer if there are a lot of inhomogeneities in the plane of calculation. With many users sharing the processor, and each plan taking many iterations, this can bottleneck the planning procedure.

Once the plan is finished, the information is passed on to the mold room . This stage involves the fabrication of the secondary and patient collimators, as well as the bolus. The secondary collimator is constructed by pouring Lipowitz metal around a styrofoam template cut to the shape of the open field. The resulting collimator can be fitted into the accessory mount on the head of the accelerator when required. The construction of the patient collimator is an elaborate process which can be accomplished in various ways. The basic idea is that a mold is made of the patient surface. Either lead or Lipowitz metal is then attached to the mold everywhere except in the area that is to be treated. The mold is then cut out in the area to be treated. This leaves an unobstructed path for the radiation in the treatment volume, but a thick layer of attenuator to shield the healthy tissue everywhere else. The amount of lead or Lipowitz metal that is required depends on the energy of the electrons.

CHAPTER 7 CONCLUSION

A pencil beam arc algorithm has been evaluated in homogeneous and heterogeneous phantoms. The phantoms contained high density inclusions of aluminum and bone analogue materials to simulate ribs, and low density inclusions of air, and cork (to simulate the lung). Experiments were carried out using electron beams of nominal energies of 12 and 20 MeV. The largest differences between the measured and calculated distributions are summarized in Table 7-1 for a variety of the phantom arrangements used. This table also shows the regions in which these differences occur. The positive differences in the table indicate the largest difference where the measured dose is greater than the calculated dose, and the negative values are for the regions where the calculated dose is greater than the measured dose. With the original code the differences found in the stationary beam were rather large, but they occurred in an area of very high dose gradient. In order to get a better agreement between dose matrices the calculation algorithm needed to produce a beam about 3 - 4 mm wider at the depth of d_{max} . When writing the algorithm the authors were aware of the problems that the stationary beam algorithm had in modelling the dose distributions to levels less than 10%, and they introduced a field width correction to make the arc algorithm work under these circumstances. This error in the code was causing very substantial errors for an arc irradiation on a homogeneous cylindrical phantom. However, once the correction was made the differences between measured and calculated dose distributions were down to 5% or less throughout most of the irradiated area. The major area of concern is in the build up region, where the measured dose is higher than the calculated

TABLE 7-1				
PHANTOM SET UP	12 MeV		20 MeV	
	MAXIMUM * DIFFERENCE	REGION ‡	MAXIMUM * DIFFERENCE	REGION ‡
0 degree arc (Stationary beam) on a flat phantom	-----	-----	+ 5 %	beyond d_{max}
	- 5 %	penumbra	- 5 %	penumbra
Arc on a homogeneous cylindrical phantom	+ 10 %	build - up	+ 10 %	build - up
	- 5 %	beyond d_{max}	- 5 %	beyond d_{max}
Arc on phantom with an aluminum insert (with stopping power correction)	+ 25 %	beyond d_{max}	+ 25 %	beyond d_{max}
	- 5 %	just beyond the aluminum	- 5 %	just beyond the aluminum
Arc on phantom with a rib bone analogue insert	+ 10 %	beyond d_{max}	+ 15 %	inside the inhomogeneity
	- 5 %	penumbra	-----	-----
Arc on phantom with a cork insert	+ 25 %	penumbra	+ 15 %	build - up
	- 10 %	inside the cork	- 15 %	edge of the cork
<p>* + indicates the maximum difference where the measured dose is greater than the calculated - indicates the maximum difference where the calculated dose is greater than the measured</p> <p>‡ beyond d_{max} refers to the region deeper than the 90 % level beyond d_{max}</p>				

dose. There is still room for improvement in this region, as the usual target for delivering a given dose to a patient is that it be within 5%. At this point the

algorithm is approaching this goal.

For the high density inhomogeneities the largest differences between calculated and measured dose distributions were found to be inside the inhomogeneity. At least part of the difference is due to not converting the relative optical density of the film to the absorbed dose in the aluminum properly, and an appropriate conversion factor has been calculated and implemented. With this correction applied the difference between the calculated and measured dose in the inhomogeneity is about 10 %. In the areas beyond the inhomogeneity differences of up to 25 % were found between the measured and calculated dose distributions for the aluminum inhomogeneity. With high density inclusions of hard bone and rib bone it was found that the differences between measured and calculated distributions followed the same pattern as with aluminum. However, the magnitude of the errors decreased as the density of the inhomogeneity approached unity. These differences appear to be due mainly to the 2-D approximation of the algorithm. With the phantom which has the inhomogeneity following the surface contour, the inhomogeneity is only 12 mm wide, and this assumption is clearly violated, resulting in significant differences. This conclusion is justified because when aluminum rods were inserted into the phantom such that they did provide full lateral scatter making the 2-D assumption valid, the high difference region distant from the inhomogeneity was not found.

The low density inhomogeneity also gave rise to differences between measured and calculated dose distributions. Differences up to 15 % were found inside and adjacent to the cork inhomogeneity. For the small air gap in the phantom differences of 25 % were found between the calculated and measured dose distributions. In an effort to find the root of the problem the difference maps

for the irradiation of the phantom with the cork insert were compared to the difference maps for an arc on the homogeneous phantom. This comparison led to the conclusion that the differences seen in the low density dose distributions were mainly due to the same problem that caused the errors in the homogeneous case. These errors were about 5 % for the homogeneous phantom, however, they appeared to be the direct cause of differences of as much as 15 %. They are occurring in a relatively high dose gradient region and the inhomogeneity is simply amplifying these differences. The differences found with the small air gap appear to also be due to the assumption by the algorithm that the inhomogeneity is infinite in extent.

In general it was found that the pencil beam algorithm predicts the dose distributions quite well for an electron arc treatment on a homogeneous phantom, although slight differences did appear in the build up region. For phantoms with inhomogeneities that are narrow in the direction perpendicular to the plane of rotation improvements are necessary in order to obtain better agreement between measured and calculated dose distributions. For stationary electron beam treatment planning a three dimensional inhomogeneity correction was found to improve the accuracy of the algorithm substantially over the two dimensional correction (Mah E. 1989). Therefore, an attempt should be made to develop and implement a three dimensional inhomogeneity correction in the electron arc algorithm. Calculation times may make this implementation impractical for general clinical use. However, there are many cases where arc electron therapy is used that the two dimensional inhomogeneity assumption will be violated, and a three dimensional approach will be needed. Further work must be carried out in order to improve the small differences in the dose

distribution in the build up region. At present in a clinical situation it is felt that the pencil beam algorithm can be used to develop a treatment plan for an electron arc therapy with reasonable confidence .

CHAPTER 8 BIBLIOGRAPHY

- Attix F, Introduction to Radiological Physics and Radiation Dosimetry, John Wiley and Sons Inc, 1986, Toronto, Canada
- Azam N, Gillin M, Kline R, Grimm D, 1986 Film Dosimetry of Small Electron Beams for Routine Radiotherapy Planning *Med.Phys.* 13 416-421
- Becker J, Weitzel G, 1956 Neue Formen der Bewegungsbestrahlung beim 15 MeV Betatron der Siemens-Reiniger-Werke. *Strahlentherapie.* 101 180-190
- Biggs P 1984 The Change in Percentage Depth Dose of Electrons due to Beam Angulation *AAMD Journal* 9 25-28
- Boyer A., Fullerton G, and Joaquin G 1982 An Electron Beam Pseudoarc Technique for Irradiation of Large Areas of Chest Wall and Other Curved Surfaces *Int.J.Radiat. Oncol. Biol. Phys.* 8 1969-1974
- Bragg W. 1910 Consequences of the Corpuscular Hypothesis of the Gamma and X Rays, and the Ranges of Beta Rays *Phil Mag* 20 385
- Cygler J, Battista J, Scrimger J, Mah E, Antolak J, 1987 Electron Dose Distributions in Experimental Phantoms: A Comparison with 2D Pencil Beam Calculations *Phys. Med. Biol.* 32 1073-1086
- Dutriex J, Dutriex A, 1969 Film Dosimetry of High Energy Electrons *Ann. N.Y. Acad. Sci.* 161 33-43
- El-Khatib E, Scrimger J, Murray B, 1990 Reduction of the Bremsstrahlung component of Clinical Electron Beams: Implications for Electron Arc Therapy and Total Skin Electron Irradiation Submitted to *Phys. Med. Biol.*
- Eyges L, 1948 Multiple Scattering with Energy Loss *Phys. Rev.* 74 1534-1535
- Gray L, 1936 Ionization Method for the Absolute Measurement of Gamma-Ray Energy *Proc. Roy. Soc. (London)* A156 578
Harshaw Filtrrol Performance Specifications, Harshaw Chemical Company, Cleveland, Ohio
- Hogstrom K, and Karup R, 1987 A Pencil Beam Algorithm for Arc Electron Dose Distributions *The Use of Computers in Radiation Therapy* ed I.A. Bruinvis, P.H. Geissen, H.J. van Kleffens, F.W. Wittkamper (North-Holland: Elsevier Science Publishers), pp 265-295

Hogstrom K, Karup R, Shiu A, and Starkschall G, 1989 A Two Dimensional Pencil Beam Algorithm for Calculation of Arc Electron Dose Distributions *Phys. Med. Biol.* **34** 315-341

Hogstrom K, and Leavitt D, 1986 Dosimetry of Electron Arc Therapy *Radiation Oncology Physics*, (Medical Physics Monograph No 15) ed J.G. Kereiakes , H.R. Elson, and C.G. Born (New York: American Institute of Physics) pp265-295

Hogstrom K, Mills M, and Almond P 1981 Electron Beam Dose Calculations *Phys. Med. Biol.* **26** 445-459

Hubbell J, 1969 Photon Cross Sections, Attenuation Coefficients, and Energy Absorption Coefficients from 10 KeV to 100 GeV. Report NSRD - NBS29, *U.S. National Bureau of Standards*

ICRU 37 1984 Stopping Powers for Electrons and Positrons *International Commission on Radiation Units and Measurements* 7910 Woodmont Ave. Bethesda, MD. 20814

Karzmark C, 1983 Advances in Linear Accelerator Design for Radiotherapy *Med. Phys.* **11** 105-128

Kase K , and Bjarngard B 1979 Bremsstrahlung Dose to Patients in Rotational Electron Therapy *Radiology* **133** 531-532

Khan F, Fullerton G, Lee J, Moore V, and Levitt S 1977 Physical Aspects of Electron Beam Arc Therapy: *Radiology* **124** 497-500

Kodak XV-2, Eastman Kodak Company, Rochester, New York

Leavit D, Peacock L, Gibbs F Jr., and Stewart J 1985 Electron Arc Therapy: Physical Measurements and Treatment Planning Techniques *Int.J.Radiat. Oncol. Biol. Phys* **11** 987-999

Leavitt D, Stewart J, Moeller J, and Earley L. 1989 Optimization of Electron Arc Therapy Doses by Multi-vane Collimation Control *Int.J.Radiat. Oncol. Biol. Phys* **16** 489-496

Mah E, Antolak J, Scrimger J, and Battista J 1989 Experimental Evaluation of a 2D and 3D Electron Pencil Beam Algorithm *Phys. Med. Biol.* **34** 1179 - 1194

Pla M, Pla C, and Podgorsak E 1988 The Influence of Beam Parameters on

Percentage Depth Dose in Electron Arc Therapy *Med. Phys* 15 49-55

Pla M, Podgorsak E, and Pla C 1989 Electron Dose Rate and Photon Contamination in Electron Arc Therapy *Med. Phys.*16 692-697

Ruegsegger D, Lerude S, Dick L 1979 Electron Beam Arc Therapy Using a High Energy Betatron *Radiology* 133 483-489

Rickner G 1983 Silicon Diodes as Detectors in Relative Dosimetry of Photon, Electron and Proton Radiation Fields Abstracts of Uppsala Dissertations from the Faculty of Science, Uppsala Universitet

Scanditronix RFA-7, Scanditronix, Uppsala, Sweden

Scanplas, Orpington, Kent, UK

Shiu A, Otte V, Hogstrom K 1989 Measurement of Dose Distributions Using Film in Therapeutic Electron Beams *Med Phys* 16 911-915

Shortt K, Ross C, Bielajew A, and Rogers P 1986 Electron Beam Dose Distributions near Standard Inhomogeneities *Phys. Med. Biol.* 32 1073-1086

Task Group 21, Radiation Therapy Committee, American Association of Physicists in Medicine 1983 A Protocol for the Determination of Absorbed Dose from High Energy Photon and Electron Beams *Med Phys* 10 741-771

Van Dyk J, Keane T, Rider W 1982 Lung Density as Measured by Computed Tomography: Implications for Radiotherapy *Int J Radiat Oncol Biol Phys* 8 1363-1372

Varian Clinac 2100C, Varian Associates Palo Alto, California.

White D 1978 Tissue Substitutes in Experimental Radiation Physics *Med Phys* 5 467-479

APPENDIX 1

CALCULATION OF PERCENT DOSE

In order to calculate the percentage depth dose from the percent ionization, an energy dependent factor must come into the calculation. According to the TG-21 (Task Group 21) protocol the dose to the phantom is given by

$$D_p = N_{\text{gas}} M_e P_{\text{ion}} P_{\text{fl}} \left[\frac{(L)^p}{(\rho)_{\text{gas}} T} \right]$$

Where D_p is the unperturbed dose to the phantom.

N_{gas} is the calibration factor for the ion chamber and electrometer

M_e is the electrometer reading corrected for pressure and temperature

P_{ion} is the correction factor for ionic recombination

P_{fl} is the electron fluence correction

$\left[\frac{(L)^p}{(\rho)_{\text{gas}} T} \right]$ is the ratio of restricted stopping powers for the phantom medium and the gas used in the chamber.

All of these terms except for the restricted stopping power and the electrometer reading are constants for the ion chamber, therefore, the true percentage depth dose can be derived from the percentage ionization in the following manner

$$\frac{D_p(x,y)}{D_p(\text{Norm})} = \frac{M_e(x,y) \left[\frac{(L)^p}{(\rho)_{\text{gas}} T(x,y)} \right]}{M_e(\text{Norm}) \left[\frac{(L)^p}{(\rho)_{\text{gas}} T(\text{Norm})} \right]}$$

Where (x,y) indicates the point in question, and (Norm) indicates the normalization point. The ratio of the M_e values is simply the percent ionization, therefore, the percentage depth dose is simply the ratio of restricted stopping powers times the percent ionization.

The values of the restricted stopping powers are energy dependent, and therefore, depth dependent. If the initial beam energy is known the values of the restricted stopping powers can be found in look up tables as a function of depth. These are presented in the TG-21 protocol (Task Group 21)

As an example the following table shows the calculation of the percentage depth dose from the percent ionization for a beam energy of 18.3 MeV (ie Nominal Energy of 20 MeV).

TABLE A-1				
DEPTH (cm)	% IONIZATION	L/p	L/p * (%ionization)	Normalized percent dose
0	96.1	.960	92.2	93.9
1	99.7	.970	96.7	98.5
2	100	.982	98.2	100
3	97.5	.996	97.1	98.4
4	94.0	1.011	95.0	96.7
5	89.5	1.028	92.0	93.7
6	82.5	1.048	86.5	88.1
7	67.5	1.072	72.4	73.7
8	46.0	1.095	50.4	51.3
9	23.0	1.112	25.6	26.1